AIAA2018-1275 8-12 January 2018
AIAA SciTech 2018, Kissimmee, FL

Computational Component Build-up for the X-57 Distributed Electric Propulsion Aircraft

Karen A. Deere*, Jeffrey K. Viken†, Sally A. Viken‡, Melissa B. Carter§, Dave Cox**
NASA Langley Research Center, Hampton, VA 23681, USA
Michael R. Wiese†† and Norma Farr‡‡
Craig Technologies, Hampton, VA 23681, USA

Abstract

A computational study of the wing for the distributed electric propulsion X-57 Maxwell airplane configuration at cruise and takeoff/landing conditions was completed. Three unstructured-mesh, Navier-Stokes computational fluid dynamics methods, FUN3D, USM3D and Kestrel, were used to predict the performance buildup of components to the full X-57 configuration. The goal of the X-57 wing and distributed electric propulsion system design was to meet or exceed the required lift coefficient of 3.95 for a stall speed of 58 knots. The X-57 Maxwell airplane was designed with a small, high aspect ratio cruise wing that was designed for a high cruise lift coefficient of 0.75 at a cruise speed of 150 knots and altitude of 8,000 ft, with an angle of attack of approximately 0°. The computational data indicates that the X-57 full aircraft drag would meet the cruise drag goal with a 25 count drag margin. The cruise configuration maximum lift coefficient is 2.07 and without including the stabilator is 1.86 at an angle of attack of 14°, predicted with the USM3D flow solver using the Spalart-Allmaras turbulence model. The maximum lift coefficient for the high-lift wing (with the 30° flap deflection) without the stabilator contribution is 2.60 at an angle of attack of 13°. For high-lift blowing conditions with 13.7 hp/prop, the maximum lift coefficient excluding the stabilator is 4.426 at α = 13°. Therefore, the lift augmentation from the high-lift propellers is 1.7 and the total lift augmentation from the high-lift system (30° flap deflection and the high-lift blowing) is 2.38. The drag for the high-lift wing with 30° flap deflection is much higher than the cruise wing configuration, but the high-lift system is used only during a small portion of the flight envelope. The pitching moment is relatively constant for both blown and unblown conditions when the stabilator is excluded. Modeling the full geometry has indicated some adverse effects from the fuselage on the wing and stabilator. At high angles of attack, the solutions with the USM3D flow solver using the Spalart-Allmaras turbulence model indicates large flow separation on the wing upper surface between the two high-lift nacelles near the fuselage, and also a reduction in sectional lift on the stabilator in the first 50 percent of the stabilator semispan. However, the large flow separation near the fuselage is mostly eliminated in the solutions predicted with two codes, USM3D and Kestrel, using Hybrid Reynolds-averaged Navier Stokes/Large Eddy Simulation turbulence models.

Nomenclature

AR	= aspect ratio, (wing span)^2/S
b	= intercept, curve fit coefficient, eqn. 8
c	= local chord, used in plots of sectional lift coefficient
C_D	= drag coefficient
C_f	= skin friction coefficient
C_L	= lift coefficient
c_l	= sectional lift coefficient
$C_{L,eff}$	= effective lift coefficient: $C_L + C_{L,prop}$
$C_{L,max}$	= maximum lift coefficient
$C_{L,prop}$	= lift coefficient from the contribution of the propeller thrust in the lift direction
$C_{L,stab}$	= lift coefficient of the stabilator
C_m or $C_{m,y}$	= pitching moment coefficient
$C_{m,x}$	= rolling moment coefficient
C_p	= pressure coefficient

* Aerospace Engineer, Configuration Aerodynamics Branch, Mail Stop 499, AIAA Senior Member.
† Aerospace Engineer, Aeronautics Systems Analysis Branch, Mail Stop 442, AIAA Senior Member.
‡ Aerospace Engineer, Configuration Aerodynamics Branch, Mail Stop 499, AIAA Associate Fellow.
§ Aerospace Engineer, Configuration Aerodynamics Branch, Mail Stop 499, AIAA Associate Fellow.
** Aerospace Engineer, Dynamic Systems & Control Branch, MS 308, AIAA Member.
†† Senior Researcher, GEOLAB, Mail Stop 128.
‡‡ Technical Group Lead, GEOLAB, Mail Stop 128.

c_{ref} = reference chord, in.
C_T = thrust coefficient
$C_{T,HL}$ = thrust coefficient from 12 high-lift propellers, $C_{T,HL} = Thrust_{HL} \div (q \cdot S)$
C_Q = torque coefficient
d = propeller diameter, ft.
h = altitude, ft.
i = incidence (wing or tail), degrees
stab = stabilator
K_T = normalized thrust coefficient
K_Q = normalized torque coefficient
M = Mach number
m = slope, curve fit coefficient, eqn. 8
offset = curve fit coefficient, eqn. 8
P = pressure, lbf/in^2
q = dynamic pressure, lbf/in^2
Re = Reynolds number based on c_{ref}
S = wing reference area, ft^2
T = temperature, °F
V = freestream velocity, ft/sec
vtail = vertical tail
$V_{t,ratio}$ = ratio of tip speed to freestream velocity
y = axis along the wing span, in.
y^+_{node} = nondimensional 1st node height in the boundary layer
y^+_{CC} = nondimensional 1st cell centroid height in the boundary layer

Symbols

α = angle of attack, degrees
ϵ = downwash angle, degrees
ρ = density, slugs/ft^3

Acronyms

AD = aileron deflection
DEP = distributed electric propulsion
HL = high lift
HLN = high-lift nacelles and pylons
HP = horsepower
KTAS = knots true airspeed
LM = Langtry-Menter transition model
QCR = quadratic constitutive relation
RPM = revolutions per minute
SA = Spalart-Allmaras 1 equation turbulence model
SST = Menter's Shear Stress Transport turbulence model
RC = rotation and curvature correction
WT = wind tunnel

Subscripts

HL = high-lift
stab = stabilator
w = wing

I. Introduction

A NASA and industry team are designing the X-57 Maxwell airplane to research the capabilities of an all-electric airplane, to determine if this emission-free flight approach also allows for a more efficient aircraft design. The single-pilot X-57 aircraft will have two main propulsion systems. Electric motors are installed in wingtip nacelles powering cruise propellers. In addition, 12 electric motors in nacelle-pylons

power high-lift propellers at take-off and landing conditions. These high-lift motors hang below and are distributed in front of the wing leading edge. One goal of the all-electric X-57 Maxwell technology demonstrator is to prove that significantly reducing wing area and increasing aspect ratio (to improve cruise efficiency) can be done without compromising takeoff and landing performance. This goal is accomplished by application of distributed electric propulsion (DEP) to effectively blow a higher dynamic pressure (q) over the wing and flap during takeoff and landing conditions.

The new DEP wing system for the X-57 airplane demonstrator will be installed on a Tecnam P2006T aircraft (fig. 1) by removing the original wing and installing the cruise-optimized DEP wing (fig. 2). At a target gross weight of 3,000 lb, there are two main design performance goals: (1) a cruise speed of 150 knots true airspeed (KTAS) at 8,000 feet, and (2) a stall speed of 58 knots equivalent airspeed. The stall speed is scaled from the original P2006T gross weight and stall performance, and equates to a a $C_L = 3.95$.

It is projected that the all-electric X-57 Maxwell airplane will achieve 5 times lower energy use than the original P2006T. The efficiency gains will be accomplished with aerodynamic improvements and by the increased propulsion system efficiency of the electric motor/battery system. The sizing design study of the wing presented in Reference 1 resulted in a wing design with a wing loading of 45 lb/ft^2, a wing area of 66.67 ft^2, an aspect ratio of 15, and a cruise C_L= 0.75. The higher aspect ratio for the new wing is needed to minimize induced drag at cruise, since the new wing's cruise lift coefficient (C_L) is much higher and the wing area is much lower than the original P2006T. The original P2006T has a wing loading of 16.365 lb/ft^2, a wing area of 158.88 ft^2, an aspect ratio of 8.8, and a cruise C_L = 0.275. The specially designed X-57 airfoil is tailored for a sectional, cruise lift coefficient of 0.90 and incorporates a 25% chord flap. The flap design uses a single-pivot displaced hinge with a 30° maximum deflection.

This paper will discuss the computational study of the component build-up for the X-57 DEP airplane configuration using the computational fluid dynamics (CFD) codes FUN3D [2], USM3D [3-5], and KESTREL [6-7]. Previous comparisons between high-fidelity CFD codes FUN3D, USM3D, OVERFLOW and STAR-CCM+ on DEP configurations were made to characterize wing performance and give confidence in the computational tools for predicting lift augmentation from DEP [8].

For the current study, the wing-alone performance was investigated with FUN3D. The wing-alone investigation included determining the impact of the high-lift system, including the DEP nacelle-pylon geometry and the 30° flap deflection. The configurations with the wing and the stabilator (stab) were studied with USM3D, and wing performance from this wing+stabilator geometry could be compared with FUN3D wing-alone results. The switch to the USM3D CFD code was necessary as the grids became too large when using the FUN3D node-based code, and the USM3D cell-centered code allowed for smaller grid sizes without compromising the grid resolution needed to model the flow physics. It wasn't that FUN3D cannot run on very large grids, but that the USM3D code allowed for smaller resource requirements and quicker solution turn-around time. Similar to the wing-alone study using FUN3D, the stabilator was also studied in isolation but with USM3D. The stabilator study included investigating three trim tab settings (0°, -5°, and -10°) at flight and wind tunnel Reynolds numbers. Wind tunnel data of the stabilator performance was obtained from a test of a 42-percent scale model of the stabilator mounted in the NASA Langley Research Center 12-Foot Low Speed Tunnel and a picture of the model in the test section is shown in figure 3. Finally, the fuselage and vertical tail were added to the cruise wing and stabilator to model the full geometry, cruise configuration at a flight Reynolds number. The high-lift, full configuration with the addition of the 30° flap deflection, will be studied in the near future.

Table 1. Configuration Component Build-up

Config.	Name	Fuselage and Vertical Tail	Wing and Tip Nacelle	30° Flap Deflection	HLN	Aileron (deg)	Stabilator (deg), Trim Tab (deg)
1	CW		x			0	
2	HLNCW		x		x	0	
3	HL30FW		x	x		0	
4	HLN30FW		x	x	x	0	
5	STAB0T0						0, 0
6	STAB0TM5						0, -5
7	STAB0TM10						0, -10
8	HLNCWSTABA00		x		x	0	-1, 0
9	HLNCWSTABA10		x		x	10	-1, 0
10	HLNCWSTABAM10		x		x	-10	-1, 0
11	HLN30FSTABA00		x	x	x	0	-1, 0
12	X57CWA00	x	x		x	0	-1, 0

II. Configurations

The configurations (configs.) used in the component build-up approach are shown in Table 1. The high-lift nacelles (HLN) used in all configurations are version 4.1. The assumption throughout the paper is that a reference to the HLN includes the high-lift nacelles and pylons. The stabilator had three trim tab settings of 0°, -5° and -10° in configurations 5 through 7, and was studied with a -1° incidence and 0° trim tab in configurations 8 through 12. Two aileron deflections (AD) of +10° and -10° were investigated using configurations 9 and 10. Since the stabilator is designed with a symmetrical airfoil by running CFD with only negative trim tab angles through both the positive and negative angle-of-attack range, the data could then be mirrored to give positive trim tab aerodynamic data.

III. High-Fidelity Distributed Propulsion Analysis Tools

Three unstructured-mesh, Navier-Stokes CFD methods were used to define the performance of the components in Table 1: FUN3D, USM3D, and KESTREL.

This work was initiated with the FUN3D CFD code because of its ease of modeling unlimited propellers with an actuator disk model, within a mesh with no special patching required in the grid. FUN3D is a node-based, finite-volume discretization, Reynolds-averaged Navier-Stokes flow solver. Fully turbulent predictions were computed with FUN3D using the Spalart-Allmaras (SA) one-equation turbulence model [9] with rotation and curvature correction (RC) [10] and the quadratic constitutive relation (QCR2000) [11] and called SA-RC-QCR2000 in this paper.

For this work, FUN3D was the primary method used to define $C_{L,max}$ for the cruise wing component and the high-lift wing with a 30° flap deflection component, without the other components included. Node-based CFD codes require approximately six times the grid resolution of cell-centered codes, therefore, smaller grids can be used with cell-centered CFD codes. Due to the reduced resources required for the cell-centered codes, and the increase in grid sizes when adding components, the team switched from FUN3D to USM3D. The USM3D code did need modification to allow for more than four propeller planes to be simulated with an actuator disk model.

USM3D is a cell-centered, finite-volume discretization, Reynolds-averaged Navier-Stokes flow solver. Fully turbulent solutions were computed with the standard SA turbulence model [9]. The SA model was chosen for most of the simulations with USM3D because the data from the SA model on a generic high-lift configuration was in better agreement with wind tunnel data than SST [12], although both models under-predicted upper surface pressures with less suction near the wing tip than WT data [13]. The USM3D flow solver with the Langtry-Menter (LM) transition model [14-15] was used for predicting transitional flow along the wing to see if computational data would match low Reynolds number wind tunnel data near stall. The SA Detached-Eddy simulation (DES) [16] was used at high angles of attack to compare with the SA model.

KESTREL is a cell-centered, finite-volume discretization, Reynolds-averaged Navier-Stokes flow solver. Two turbulence models were used with KESTREL; SA [9] and SA with Delayed Detached-Eddy simulation (DDES) [17]. The SA model in KESTREL uses the constant c_{t3} = 0, not 1.2, as documented in reference 9, and models production based on the square root of the product of vorticity and strain, to prevent overproduction in areas undergoing strong acceleration or deceleration. The DDES, as compared to DES, is a newer model with improvements in detecting the edge of the boundary layer and delays the switch from RANS (within the boundary layer), to LES outside of the boundary layer.

A. Grid Generation

The gridding guidelines established in the 2nd AIAA CFD High Lift Workshop [18] were used to create grids for this study. An initial grid study of the cruise wing (configuration 1) and wing with 30° flap (configuration 4) was completed by using the guidelines for generating a medium, fine and extra fine mesh. The fine mesh was chosen for wing-only studies as a compromise between resources required and changes in coefficient values between mesh levels. The gridding guidelines were followed when adding components such as the stabilator and fuselage with vertical tail (vtail).

The GridTool/VGRID [19] software was used to generate the meshes for FUN3D and USM3D simulations. GridTool is used to take a supplied geometry file and create the necessary points, curves, patches and grid topology (sources) to define the surface for grid generation. VGRID is a tetrahedral unstructured grid program that can either be run interactively or in a batch mode with grid spacing corresponding to the strength of user-defined sources placed in the domain. The advancing layers method [20] is used to generate the boundary layer and the advancing front is used to generate the farfield tetrahedral mesh. The advancing layers method forms prismatic layers that are divided into three tetrahedral cells. POSTGRID is used for additional post-processing, to close any open pockets that do not have cells and to improve the grid quality. For FUN3D, a utility code was used to take the VGRID mesh and combine the tetrahedral cells in the boundary into prisms and write out a mixed element mesh. For USM3D, the VGRID mesh is used as is, with the prismatic layers of tetrahedral cells created from the advancing layer method. The distance from the surface of a geometry, to the cell centroids of the tetrahedral boundary cells, is one-fourth of that to the first layer of nodes, resulting in the $y^+_{CC} = 0.25 \cdot y^+_{node}$. For all grids, a flat-plate, turbulent boundary layer calculator was used with the reference chord length, a Reynolds number based on reference chord length, the intended y^+, and an intended number of layers of cells within the boundary layer, to determine the first node height and expansion rate of the grid for input to VGRID. FUN3D results from reference 21 for a similar blown-wing configuration showed that using an intended y^+= 0.67 for a medium mesh had solution y^+ values up to 2 for the blown, high-lift wing solutions, even though the solution y^+ were less than 1 for the unblown wing solutions. Values of solution y^+ that are less than 1 are recommended to adequately model the boundary layer flow.

Unstructured, mixed element meshes were used for the FUN3D simulations. The mixed element mesh had prisms in the boundary layer and tetrahedral cells in the farfield, with pyramids to transition between the boundary layer and farfield cells. FUN3D is a node-based code so the number of nodes characterizes the number of unknowns. Semispan wings were used in the computational model since all calculations were computed at 0° angle of sideslip and little lateral variation was expected. A full span solution was computed for the blown, high-lift wing (30° flap) with high-lift nacelles at α = 0°. The differences between the full span and semispan configurations for lift, drag, and pitching moment coefficient were 0.2%, 0.8% and 0.1%, respectively. These small differences between the solutions confirmed the approach of using a semispan mesh.

Unstructured, tetrahedral meshes were used for the USM3D simulations. The number of cells characterizes the number of unknowns for USM3D since it is a cell-centered code. The same grid used for FUN3D and USM3D would have 6 times more resolution for the USM3D solution, than for the FUN3D solution because of it being cell-centered and not node-based. Consequently, smaller grids and less resources can be used for USM3D, than FUN3D.

The mesh sizes for each configuration are shown in Table 2. Configurations 1 through 4 were used with FUN3D and configurations 5 through 12 were used with USM3D. The power meshes for configurations 8 through 10 were made for wingtip, cruise power at 150 KTAS. The power mesh for configuration 11 was made for high-lift blowing at 58 KTAS. The grids for configurations 1 through 11 had farfield boundaries that extended to approximately 100 chord lengths away from the wing. The reference chord length was C_{ref}= 25.56 in. For the full geometry (configuration 12), the farfield boundaries extended over 15 body

lengths (209 chord lengths) away from the configuration.

For the FUN3D code, the semispan mesh of the cruise wing with wingtip nacelles (config. 1) had 44 million nodes and the semispan mesh for the cruise wing with high-lift and wingtip nacelles (config. 2) had 48 million nodes. As recommended in reference 16, both meshes were generated with an intended $y^+ = 0.3$ for an extra fine mesh, and 32 grid layers were specified within the boundary layer. The corresponding VGRID spacing for the first node height was 6.3e-5 in. as determined by the boundary layer calculator for the cruise mesh at *Re* = 2.83 million, and 150 KTAS.

The FUN3D semispan mesh for the high-lift wing (30° flap setting) and tip nacelle had 149 million nodes. Adding the high-lift nacelles brought the grid to 153 million nodes. Both meshes were generated with an intended $y^+ = 0.3$ and 32 grid layers within the boundary layer. The corresponding VGRID spacing for the first node height was 1.3e-4 in. for the high-lift wing mesh at *Re* = 1.33 million, and 58 KTAS.

For the USM3D semispan mesh of the stabilator alone, the intended y^+ was relaxed to $y^+ = 0.67$ and 30 grid layers within the boundary layer and the stabilator reference length was 30.67 in. The three meshes (0°, -5°, -10° trim tab settings) for 58 KTAS had the first node height of 2.9e-4 in. for a *Re* = 1.6 million. The three meshes for 150 KTAS had the first node height of 1.4e-4 in. for a *Re* = 1.6 million.

Here are two examples of the grid size savings for using USM3D instead of FUN3D. The FUN3D grid created for the cruise wing with high-lift and wingtip nacelles (config. 2) has 48 million nodes, but if it was used for USM3D, then it would have 140M cells. However, the USM3D grid was 121 million cells when the stabilator geometry was added to the cruise wing with high-lift and wingtip nacelles geometry. Therefore, by switching CFD codes to USM3D and taking advantage of the increase in resolution from cell-centered grids versus node-based, we were able to reduce the cell count by 19M cells and also model another geometry feature. Another example is the FUN3D grid created for the high-lift wing, with 30° flap deflection, high-lift and wingtip nacelles (config. 4), which has 153 million nodes. If that grid was used with USM3D, it would have 461M cells. However, when switching to USM3D, the new grid (for high-lift wing, with 30° flap deflection, high-lift and wingtip nacelles) that included the stabilator and clustering for high-lift blowing (config. 11) was 359M cells, a savings of 62M cells while adding geometry features.

No special patching was required within the grid for FUN3D to simulate the propellers, except the clustering of cells to resolve the flow. The clustering of cells was achieved using VGRID volume sources during grid generation. Grids for powered or blown runs with the USM3D code required zero-thickness patches created at the locations of the propellers for implementing the actuator disk model, which simulates the effect of propellers.

The mesh used with the Kestrel CFD code was created from the full configuration mesh used with the USM3D CFD code. The Carpenter Grid Utility tool was used to merge the boundary layer tetrahedral cells into prism layers and write the file in an AVMesh format (*.avm) necessary for Kestrel.

Table 2. Configuration Mesh Sizes

Config.	Name	Description	Nodes FUN3D No-Power Mesh	Nodes FUN3D Power Mesh	Cells USM3D No-Power Mesh 58 KTAS and 150KTAS	Cells USM3D Power Mesh Or Blown Mesh
1	CW	Cruise Wing	43,819,990	43,980,340	138,917,478	
2	HLNCW	Cruise Wing, HLN	47,811,306	47,964,659	140,119,871	
3	HL30FW	Flapped Wing	149,168,238	149,280,572	460,865,415	
4	HLN30FW	Flapped Wing, HLN	153,168,117	153,242,173	461,751,910	
5	STAB0T0	stabilator 0° tab 0°			44,633,557 and 45,541,815	NA
6	STAB0TM5	stabilator 0° tab -5°			45,776,989 and 46,565,192	NA
7	STAB0TM10	stabilator 0° tab -10°			45,726,929 and 46,459,816	NA
8	HLNCWSTABA00	Cruise Wing, HLN, Aileron 0° stabilator -1° tab 0°			121,082,678	121,127,722
9	HLNCWSTABA10	Cruise Wing, HLN, Aileron 10°, stabilator -1° tab 0°			112,288,976	112,266,456
10	HLNCWSTABAM10	Cruise Wing, HLN, Aileron -10°, stabilator -1° tab 0°			112,304,323	112,172, 899
11	HLN30FSTABA00	Flapped Wing, HLN, Aileron 0°, stabilator -1° tab 0°			347,096,423	359,444,677
12	X57CWA00	Full Geometry: Fuselage, vtail, Cruise Wing, Aileron 0°, stabilator -1° tab 0°			124,903,224	

B. Computational Scheme

Initially, the codes were run steady-state with a local time stepping method and when needed, time-accurate, global time stepping was used to obtain acceptable convergence. Typically, the higher angles of attack or more complex geometry required time-accurate solutions.

The FUN3D code was used for configurations 1 through 4. Steady-state solutions were used for configuration 1 and 3, the wing geometry without the HLN. For configuration 2, steady-state solutions were computed for $\alpha < 8°$ and time-accurate solutions for $\alpha > 6°$. All configuration 4 (HL blowing and no HL blowing) solutions were run with time-accurate, global time stepping, except $\alpha = 0°$ with no HL blowing.

The USM3D code was run with configurations 5 through 12. The stabilator configurations 5 and 7 were run steady-state, with a local time stepping method. All solutions converged very well with the local time stepping method, except a few solutions at high angles of attack near stall. These unsteady cases were switched to time-accurate, global time stepping, to obtain acceptable convergence. All of the solutions for configurations 6, and 8 through 12 were run with USM3D time-accurate, global time stepping. The USM3D solutions were second order in both spatial and temporal accuracy.

Configuration 12 was also run with the Kestrel code, using a second-order time-accurate, global time stepping method. The Kestrel solutions were second order in both spatial and temporal accuracy.

C. Boundary Conditions and Actuator Disk Modeling

A symmetry plane boundary condition is used for the semispan grids while the farfield boundaries utilized the Riemann invariants boundary condition. All of the solid surfaces were set with the no-slip boundary condition.

All of the powered simulations for this study used an actuator disk representation for the high-lift propellers, with thrust and torque coefficient data being inputs to the solution. The thrust and torque coefficient data were derived from the XROTOR [22] blade element momentum analyses.

There are 6 options to loading the rotor in FUN3D but the one implemented for this work was a body force based on the optimal distribution of Goldstein [23] implemented as described by Stern, Kim, and Patel [24]. Inputs for the actuator boundary condition included tip radius, hub radius, and the (x, y, z) location of the hub centers for each propeller. Additionally, the $V_{t,ratio}$, the normalized thrust coefficient and the normalized torque coefficient, were required for each propulsor. Positive values of $V_{t,ratio}$ resulted in a clockwise propeller rotation (from the pilot's view) on the right wing, a rotation that opposed the wingtip vortex. The torque and thrust coefficients are shown in equations 2 and 3, respectively. The normalized torque coefficient and normalized thrust coefficient were computed with equations 4 and 5 and used in the FUN3D actuator boundary condition input file.

$$V_{t,ratio} = \left[\pi * \left(\frac{RPM}{60}\right) * d\right] / V \quad (1)$$

$$C_Q = Torque/[\rho(\frac{RPM}{60})^2 d^5] \quad (2)$$

$$C_T = Thrust/[\rho(\frac{RPM}{60})^2 d^4] \quad (3)$$

$$K_Q = \frac{8}{\pi^3} C_Q \quad (4)$$

$$K_T = \frac{4}{\pi^3} C_T \quad (5)$$

For USM3D, an actuator disk model was also used to represent the high-lift propellers. The nine values needed for the actuator disk model include the rotor outer radius, the location (x, y, z) of the rotor center, the advance ratio, the thrust and torque coefficients, the propeller rotational direction and the type of rotor jump conditions. The type of rotor jump condition is a constant pressure jump, with no radial variation.

For the blown-wing power conditions, both codes used 4548 RPM, a torque of 15.9 ft-lbf, a thrust of 49.7 lbf, freestream velocity of 58 KTAS, and the propeller diameter (d) of 1.89 ft for the high-lift propellers to compute the information needed as inputs to the actuator disk model. This resulted in high-lift blowing conditions of 13.7 hp/HL prop. For the cruise power conditions, both codes used 2250 RPM, a torque of 137 ft-lbf, a thrust of 115 lbf, freestream velocity of 150 KTAS, and the propeller diameter of 5 ft. This resulted in cruise power conditions of 58.7 hp/cruise prop.

D. Flow Conditions

Two primary conditions were used for this computational study, the design cruise speed and the design stall speed. A third condition was used to compare with wind tunnel data. The conditions for the design cruise speed were a freestream velocity of 150 KTAS, Reynolds number based on chord (*Re*) of 2.83 million, an altitude (h) of 8000 feet, and an air temperature (T) of 30.5°F. The conditions for the design stall speed were a freestream velocity of 58 KTAS, *Re* = 1.33 million, h = 0 feet, and T = 59°F. For comparison to wind tunnel data, the conditions used for CFD were a freestream velocity of 34.4 KTAS, *Re* = 0.38 million, h = 0 feet, and T = 72.9°F.

E. Convergence

The criteria used to monitor and determine solution convergence was a drop of at least two orders of magnitude for the flow solution residual. In addition, for an interval of 1,000 iterations, it was required that for steady-state solutions the standard deviation of C_L be less than 0.0012 and C_D be less than 0.0020.

IV. Results

The results are discussed in a build up approach, with some additional content included (i.e., code comparisons and the effect of aileron deflection). First, the wing-alone solutions that were computed with FUN3D SA-RC-QCR2000 turbulence model are discussed, followed by the stabilator-alone that were computed with USM3D SA turbulence model. Although the FUN3D code was originally chosen for this

work due to the ease of modeling numerous propellers, the authors switched codes to USM3D to take advantage of the smaller grids that can be used with the cell-centered USM3D code, that are larger for the node-based FUN3D code. The details of switching codes and grid comparisons are discussed in section III, subsection A (Grid Generation). Therefore, following the wing-alone and stabilator-alone results, there is a brief discussion of results from code comparisons between FUN3D and USM3D. Then the contribution of the stabilator is discussed in subsection D, along with downwash and aileron deflection. Finally, full geometry (with the addition of the fuselage and vtail) is discussed in subsection E.

A. Wing Alone

Figures 4(a), 4(b) and 4(c) show the impact of the high-lift nacelles (HLN) and pylons, for the unpowered cruise wing (CW) using configurations 1 and 2 at 150 KTAS, and the unblown and blown high-lift wing with 30° flap deflection (HL30FW) using configurations 3 and 4 at 58 KTAS, respectively. These solutions were computed with FUN3D using the SA-RC-QCR2000 turbulence model. In general, the nacelles reduce the lift across the range of angle of attack (α) and the lift curve slopes are about the same for both the CW and the HL30FW. The unpowered cruise wing with high-lift nacelles has a ΔC_L decrement of 0.10 to 0.15 over the computed angle-of-attack range, with the angle of attack at stall being the same for both configurations 1 and 2 (fig. 4(a)). Similarly, the unblown HL30FW with HLN configuration has a ΔC_L decrement of 0.05 to 0.11 (fig. 4(b)) compared to the unblown HL30FW without HLN. The C_L decrement due to HLN diminishes as $C_{L,max}$ is approached. In the blown wing case with HL power (Fig. 4(c)), the ΔC_L decrement occurs in the angle-of-attack range from 6° to 10°, with a maximum ΔC_L= -0.30 at α = 10°.

Figures 5(a), 5(b), and 5(c) show the impact on the span loading of the high-lift nacelles (HLN) for the unpowered cruise wing (CW) using configurations 1 and 2 at 150 KTAS, and the unblown and blown high-lift wing with 30° flap deflection (HL30FW) using configurations 3 and 4 at 58 KTAS, respectively. The unpowered cruise wing (fig. 5(a)) has a Δc_l decrement in the region of the nacelles. The unpowered HL30FW with HLN configuration (fig. 5(b)) has a Δc_l decrement in the region in between the nacelles. In the blown wing case with HL power (13.7 hp/prop) (Fig. 5(c)), the Δc_l decrement occurs overall, and the local Δc_l peaks on the high-lift propeller blade upflow are lower in the presence of the nacelles. Also, there is a decrement in the inboard lift of the wing inboard of the blown region.

Comparisons below (subsection E.) show the influence of the fuselage and vertical tail on the lift in the inboard wing region for the cruise wing configuration.

B. Stabilator Alone

The X-57 has an all moving horizontal tail, called a stabilator, with a trim tab to generate the correct stick forces for the pilot. For stability and control analysis, the aerodynamic performance of the stabilator alone was needed for a range of angles of attack and trim tab deflections. The data is used to generate stability derivatives that are needed to compute the stick free longitudinal static stability and control of the aircraft. These four derivatives are: (1) change of lift with angle of attack, (2) change of pitching moment with angle of attack, (3) change of lift with trim tab deflection, and (4) change in pitching moment with trim tab deflection. Figures 6 and 7 show the lift, drag, and pitching moment coefficients from USM3D SA analyses for the stabilator with three trim tab settings (configurations 5-7) at 58 KTAS (design stall speed) and 150 KTAS (design cruise speed), respectively. The decreasing tab deflection acts to decrease C_L and increase pitching moment coefficient (C_m) of the stabilator across the range of α at both velocities. The drag coefficient (C_D) decreases for α > 3° and increases for α < 3° as the tab deflection decreases from 0° to -10°. The stabilator stalls after α =-19° and α =19° for the design stall speed conditions (fig. 6) as the flow separates from the stabilator, resulting in a loss of lift, a large increase in drag, and a large change in pitching moment. For the design cruise speed condition (fig. 7), the stabilator stalls after α = -18° and α = 18°. There is a linear shift in the lift curve versus angle of attack from tab deflection and the lift curve slope is constant. However, pitching moment is linear only in a small region near 0° angle of attack.

Figure 8 shows the comparison between USM3D computations and wind tunnel (WT) data for the stabilator with 0° trim tab setting (configuration 5) at wind tunnel conditions (34.4 KTAS, a wind tunnel *Re* = 0.38 million, h = 0 ft, and T = 72.9°F). The fully turbulent flow solutions with the USM3D SA model compare well with wind tunnel data for -10° ≤ α ≤ 10°. Although the wind tunnel lift coefficient increases slightly from α = 10° to α = 12°, the drop in pitching moment data indicates an increase in flow separation at α = 12°. The fully turbulent flow solutions with SA indicates wing stall after α = 15°. However, the

transitional flow solution of LM matches wind tunnel data well at α = 12° and fairly well at α = 15°.

The comparisons between solutions using the USM3D LM transition model and USM3D SA fully turbulent model at wind tunnel conditions are shown in figures 9 and 10. Figure 9 has Mach contours at y = 10 inches and figure 10 shows pressure coefficient contours on the surface of the stabilator, as well as a C_p surface distribution at y = 10 in. The LM predicts a laminar separation bubble on the wing upper surface as shown in figure 9(a) with blue Mach contours and recirculating streamlines, while the SA model predicts attached flow along the full wing upper surface (fig. 9(b)). The flow at the wing leading edge reaches higher Mach numbers (higher flow acceleration) with the SA model, compared to LM, as the turbulent flow expands and remains attached around the leading-edge curvature. The peak minimum pressure is much lower for the fully turbulent SA solution, reaching C_p = -4.5, while the laminar-turbulent transitional flow of the LM solution only has a peak minimum pressure of C_p = -1.5 (fig. 10(c)). These data comparisons at wind tunnel Reynolds numbers (figs. 8-10) indicate that perhaps the wind tunnel data does have some laminar flow present on the stabilator and therefore, the laminar boundary layer separates at an earlier angle of attack than the fully turbulent boundary layer.

C. Code Comparisons Wing Lift Coefficient

Figure 11 shows the FUN3D and USM3D code comparisons of the unpowered wing lift coefficient for the cruise wing at the design cruise speed conditions and the blown, high-lift wing with 30° flap at the design stall speed. For these comparisons, the wing geometry includes the high-lift nacelles and tip nacelle. Only the wing geometry is modeled for the FUN3D data. However, the geometry for the USM3D solutions modeled the wing+stabilator, so the force and moment data for the wing alone was computed for comparisons to FUN3D results.

For the cruise wing at the design cruise speed (fig. 11(a)), there is fairly good agreement in the lift curve slope between the codes with the SA turbulence model, with the USM3D predicting slightly higher lift across the range of angle of attack except at α = 12°. Figures 12 and 13 show the flow contours for USM3D SA at α = 12° and α = 13°, respectively. The unusual dip in the C_L versus alpha curve at α = 12° for the USM3D SA solution, results from a large amount of flow separation across the wingspan as shown as reversed streamlines that move upstream toward the wing leading edge in figure 12(a) and as dark blue skin friction contours, in large triangular-shaped patterns, behind HLN7, HLN8, and HLN10. Also, smaller flow separation regions exist behind HLN9, HLN11, and HLN12. At α = 13°, there is a large increase in lift coefficient (fig. 11(a)) as the large triangular-shaped flow separation patterns dissipate, except at HLN12 (fig. 13). There is still flow separation across the wing semispan, but the reversed streamlines do not move forward of approximately the 75 percent chord location, except at HLN12. It is believed that the vortices shedding off the HLN at α = 12° strike the wing leading edge and affect the boundary layer flow that results in flow separation very near the wing leading edge. At α = 13°, the vortices travel above the wing surface and do not affect the boundary layer flow except at HLN12. For FUN3D, the SA-RC-QCR2000 predicted slightly lower lift across the angle-of-attack range than the SA model. Maximum lift coefficient was within 1° for the angles of attack computed, with a maximum lift coefficient of 1.85 for USM3D SA, 1.78 for FUN3D SA, and 1.7 for FUN3D SA-RC-QCR2000.

For the blown, high-lift wing with 30° flap deflection (fig. 11(b)), the FUN3D SA and SA-RC-QCR2000 turbulence models predict more lift for α < 10°, but predict less lift for α > 10°, than USM3D SA. The USM3D SA code predicts a higher maximum lift coefficient than FUN3D but both codes predict similar flow separation with wing stall (fig. 14). Figure 14 shows the comparison between the codes and turbulence models at the angle of attack for maximum lift and wing stall. Both codes with both turbulence models predicted large flow separation within 0 in. < y < 23 in. when the wing stalls, which would be within the fuselage. The flow along the rest of the wing is similar, but with less flow separation in the blown region near the wing trailing edge (just upstream of the flap) predicted with USM3D, than with FUN3D.

These comparisons of solutions between FUN3D to USM3D provided some evidence that switching codes from FUN3D to USM3D was acceptable, in an effort to allow for reasonable grid sizes and reduced solution convergence times.

D. Wing+Stabilator

Figure 15 shows the comparison of lift coefficient values for configurations 8 through 11. The cruise wing configurations 8 through 10 were computed at conditions for the design cruise speed of 150 KTAS, *Re* = 2.83 million, h = 8000 ft, and T = 30.5°F. The high-lift wing with the 30° flap deflection (configuration

11), was computed at the design stall speed conditions of 58 KTAS, *Re* = 1.33 million, h = 0 ft, and T = 59°F, without and with HL power. The stabilator is at a -1° incidence for configurations 8 through 11. For the high-lift blowing cases, the effective lift coefficient includes the contribution of the propellers, $C_{L,eff} = C_{L,total} + C_{L,prop}$.

i. High-Lift System: Lift Augmentation, Drag and Pitching Moment

The lift augmentation is the increased lift of one configuration over another, and is computed by dividing the $C_{L,max}$ of one configuration by the $C_{L,max}$ of the second configuration. For these calculations, the stabilator contribution to lift is excluded and data is shown in figure 15. For the high-lift wing+stabilator geometry (HLN30FSTABA00), the unblown maximum lift coefficient is $C_{L,total} - C_{L,hstab}$ = 2.60 and the maximum lift coefficient including the propeller contribution to lift is $C_{L,eff} - C_{L,hstab}$ = 4.426, both at α = 13°. For the cruise wing+stabilator geometry (HLNCWSTABA00), the unpowered maximum lift coefficient is $C_{L,total} - C_{L,hstab}$ = 1.85 at α = 15°. Therefore, the high-lift wing lift augmentation from the 30° flap deflection is approximately a factor of 1.41 above the cruise wing ($1.41 = 2.60 \div 1.85$). The lift augmentation from the DEP system is an additional factor of 1.70 above the unblown high-lift wing with the 30° flap deflection ($1.70 = 4.426 \div 2.60$), indicating a major advantage of the blown-wing for lift augmentation. The total lift augmentation of the high-lift wing with 30° flap deflection and DEP system is approximately 2.39 ($2.39 = 4.426 \div 1.85$). Additionally, although the fuselage and vertical tail are not included in the prediction yet, the data thus far ($C_{L,eff} - C_{L,hstab}$ = 4.426) indicates that the lift coefficient of 3.95 for the design stall speed goal can be achieved with some margin.

The component buildup of lift, drag and pitching moment for the high-lift wing with 30° flap deflection is shown in figure 16. Unfortunately, the full geometry with fuselage and vertical tail for the high-lift wing with 30° flap deflection and DEP system has not been completed yet. However, figure 16 shows the effect of adding the stabilator, and also the effect of high-lift blowing on total lift, lift without the stabilator contribution, drag and pitching moment coefficients. The lift augmentation from the DEP blown-wing system is further illustrated in the large increase in lift curves from the unblown wing solutions to blown-wing solutions in figures 16(a) and 16(b). The drag for the high-lift wing (fig. 16(c)) is much higher than for the cruise wing configuration (shown in fig. 24(a) and will be discussed in Section E). The drag at maximum lift is C_D = 0.6732 with high-lift blowing and is C_D = 0.2474 without high-lift blowing, but the minimum drag with high-lift blowing is C_D = 0.2550 for $C_{L,total}$ = 2.5389 at α = 0°. Note that with a thrust/prop of 49.7 lbf, the thrust coefficient ($C_{D,thrust}$) is -0.7663 for the 12 high-lift props, which more than offsets the increase in drag with high-lift power. The pitching moment coefficient with and without the contribution of the stabilator is shown in figures 16(d) and 16(e), respectively. The pitching moment data with the stabilator is linear with a constant slope for α < 10° for both the blown and unblown configurations (config. 11). There is a slight slope change and rounding of C_m for $\alpha >$ 10°. The pitching moment is relatively constant, for both blown and unblown conditions, when the stabilator is excluded (fig. 16(e)).

ii. Downwash

To conduct the stability analysis for the X-57, as well as provide input for the flight simulator, the downwash on the stabilator is needed to define the tail lift for trim calculations and pitching moment characteristics for stick force calculations. The lift on the stabilator would be characterized by

$$C_{L,stab} = \frac{\partial C_{L,stab}}{\partial \alpha}(\alpha_{stab}) = \frac{\partial C_{L,stab}}{\partial \alpha}(\alpha_w + i_w + i_{stab} - \epsilon) \quad (6)$$

where ϵ is the downwash angle. From computations of the stabilator-alone results (Section B), the value of $\frac{\partial C_{L,stab}}{\partial \alpha}$= 0.065558 per degree.

With the CFD solution calculations of the stabilator lift ($C_{L,stab}$) for the wing+stabilator (Section D) and the X-57 configuration with stabilator (Section E), the downwash can be computed from equation 6. The computed CFD downwash for all wing+stabilator and X-57 configurations is given in figure 17(a). To be able to use the downwash in a stability and control and trim assessment, an analytic variation of the downwash is needed for various flight conditions. Reference 25 explains that the downwash angle is a function of the lift, and also the downwash angle at infinity behind the wing is defined by the following relationship

$$\epsilon^\circ = \left(\frac{180}{\pi}\right) * \epsilon_{rad} = \left(\frac{180}{\pi}\right) * \frac{2*C_L}{\pi*AR} \quad (7)$$

The computed downwash in figure 17(a) appears to be very close to a linear function of C_L in regions preceding stall (or preceding large areas of wing separation). The computed downwash data was curve fit with the following relationship

$$\epsilon^\circ = \left(\frac{180}{\pi}\right) * \left[\frac{2*(m*C_L+b)}{\pi*AR}\right] + offset \quad (8)$$

The values used to curve fit the computed downwash to the variation with C_L are:

Table 3. Curve Fit Coefficients to Compare with Computed Downwash Angle (equation 8)

Configuration	*m*	*b*	*offset*
HLNCWSTABA00	0.65	0.33	0.0
HLN30FSTABA00 (No HL Blowing)	1.0	0.00	-1.6
HLN30FSTABA00 (HL Blowing – ON)	1.0	0.00	-2.7
X57CWA00	1.5	-0.76	0.0

The data presented in figure 17(a) compares the curve fit downwash to the computed angles. For the flapped wing with high-lift power (HLN30FSTABA00), the downwash does not increase linearly with $C_L > 3.5$. Curve fit 2 for this configuration is limited to $\epsilon = 5°$ for $C_L > 3.5$. Figure 17(b) shows the variation in stabilator lift with configuration angle of attack compared with values from the curve fit downwash for a stabilator incidence of -1.0°.

Figures 18 through 21 show the Mach contours and streamlines for the wing+stabilator solutions for the cruise wing, the unblown high-lift wing, and the blown high-lift wing configurations. Figure 18 shows how the wing wake goes over the upper side of the stabilator at y = 40 in. at $\alpha = 0°$. Therefore, the cruise wing wake will always be above the stabilator at higher angles of attack. Figures 19(a) and 20(a) show the wing with a 30° flap deflection at y = 40 in., computed at $\alpha = 0°$ for unblown conditions and with high-lift blowing using 13.7 hp/prop, respectively. Unlike the cruise wing, the wing wake over the flap has more downwash and travels under the stabilitor $\alpha = 0°$ for both the unblown and blown high-lift wings. For the high-lift unblown-wing case at y = 40 in. (fig. 19), the stabilator goes through the wing wake at $3° < \alpha < 6°$, and below the wake for $\alpha \geq 6°$. For the high-lift blown-wing case at y = 40 in. (fig. 20), the stabilator is above the wing wake for $\alpha < 9°$, travels through the wake for $9° < \alpha \leq 12°$, and below the wake for $\alpha > 12°$. For the high-lift blown-wing case at y = 50 in. (fig. 21), the stabilator is in the wing wake for $6° \leq \alpha \leq 9°$ and below the wake for $\alpha > 9°$.

iii. Aileron Deflection

The cruise wing with HLN and stabilator (-1° incidence, 0° trim tab) configuration was used to determine the effect of aileron deflection on rolling moment. Figure 22 shows the effect of +10° and -10° AD on rolling moment coefficient for the wing+stabilator configuration at the design cruise speed using USM3D SA. The contribution of the stabilator to rolling moment was excluded. As this is a semispan model, there is a significant rolling moment at zero aileron deflection, however, the aileron control power can be seen in the differential in $C_{m,x}$ between the positive and negative deflections. There is a fairly constant rolling moment differential between aileron deflections of +10° and -10° up through $\alpha = 12°$, followed by a smaller differential up through $\alpha = 16°$ (fig 22). The differential in $C_{m,x}$ between the positive and negative deflections is eliminated at $\alpha = 17°$ and looking at comparisons of sectional lift coefficient (c_l) at $\alpha = 16°$ and $\alpha = 17°$ in figure 23 helps to explain why.

Figure 23 shows four comparisons of sectional lift coefficient (c_l) of the cruise wing with +10° and -10° AD, at $\alpha = 16°$ and $\alpha = 17°$. First, there is not much difference in c_l across the semispan between the $\alpha = 16°$ and $\alpha = 17°$ solutions for -10° of AD (fig. 23(a)). However, the c_l comparisons between $\alpha = 16°$ and $\alpha = 17°$ for the +10° of AD show that the wing is stalled outboard at $\alpha = 17°$ due to the increased camber of the +10° of AD (fig. 23(b)). Separation effects can also be seen in figure 23(b) between y = 45 in. and y = 80 in., as this is near the wing's overall stall condition. It is clear that the roll control (differential in $C_{m,x}$ between the positive and negative deflections) at $\alpha = 16°$ is from the large difference in c_l for 130 in. < y < 180 in. (fig. 23(c)). As α is increased from 16° to 17° (fig. 23(d)), there is only one spanwise region where

the lift with AD = +10° is greater than the AD = -10° deflection, 125 in. < y < 160 in. However, there are 3 spanwise regions where the AD = -10° deflection has higher lift, one of them being the outer section of the aileron. In this case, the rolling moment differential goes to zero.

E. Cruise Wing, Stabilator, and Fuselage/Vertical Tail

The conditions for all of the cruise wing cases were a freestream flow of 150 KTAS, Re = 2.83 million, h = 8000 ft, and T = 30.5°F. Figure 24 shows the component buildup of drag, pitching moment and lift for the configurations with the cruise wing. Compared to a clean wing (config. 1), adding the HLN (config. 2) resulted in a decrease in lift and increase in drag with minimal effect on pitching moment. The addition of the stabilator (config. 8) with a -1° incidence and a 0° trim tab setting increased lift for $\alpha > 5°$ and decreased lift for $\alpha < 5°$ (fig. 24(d)). Adding the fuselage to the geometry (config. 12) had a very small decrease in total lift for $\alpha < 12°$.

For the USM3D SA solutions for the full geometry, the total minimum drag was $C_{D,total}$ = 0.0482 for a $C_{L,total}$ = 0.63 at $\alpha = 0°$, and at the cruise lift coefficient of $C_{L,total}$ = 0.75, the total drag was $C_{D,total}$ = 0.0517 for an α = 0.91° (fig. 24(a)). Reference 1 established the airplane drag to meet the cruise speed goal of $C_{D,total}$ = 0.0542. This computational data indicates that the X-57 full aircraft drag would meet the goal with a 25 count drag margin. Of course, the real aircraft, with rivets and skin surface intersections, will have some drag that is not modeled in the smooth computational geometry. There is however, in addition to the 25 counts already available here, some drag savings from induced drag reduction with cruise power on and from laminar flow on the wing at conditions for the design cruise speed. Reference 26 showed a savings of 24 counts of induced drag reduction with cruise power and 33 counts of drag savings from laminar flow drag over approximately 65 percent chord along the wingspan on the upper surface and between the high-lift nacelles on the lower surface. The previous estimate of total wing drag in reference 26 was computed by making adjustments to the fully turbulent CFD $C_{D,wing}$ for the drag savings due to cruise power and laminar flow, and was 7.6 drag counts above the target wing drag, but within the drag margin of the total aircraft drag by only using 10 percent of the allotted margin. Therefore, this is an excellent position to now have the full geometry modeled and be under the total aircraft drag estimate by 25 counts and still have some possible savings with power and laminar flow.

The pitching moment coefficient with and without the contribution of the stabilator is shown in figures 24(b) and 24(c), respectively. The effects of building up the configuration from the wing alone (configs. 1 and 2), to adding the stabilator (config. 8), and finally adding the fuselage (config. 12) is obvious in the plot of pitching moment as the near constant C_m for the wing alone, changes to a decreasing C_m with increasing lift when adding the stabilator and an additional slope change when adding the fuselage (fig. 24(b)). When the stabilator is excluded from the pitching moment coefficient, C_m is relatively constant for configurations 1, 2, and 8, while the C_m increases with increasing lift due to the fuselage (config. 12).

The total lift coefficient, and the total lift coefficient excluding the stabilator, are plotted as a function of angle of attack in figures 24(d) and 24(e). Figure 24(e) was included because the X-57 aircraft horizontal stabilator is all moving. Therefore, adjusting the incidence can modify the total aircraft lift and pitching moment at a constant aircraft angle of attack. For the USM3D SA solutions for the full geometry, the total maximum lift is $C_{L,total}$ = 2.07 at α = 14° and at α = 19° (fig. 24(d)). The maximum lift for the wing occurs at α = 14°, but the fuselage and stabilator continue to generate lift up through α = 19°. The maximum lift for the full geometry (config. 12) without the stabilator is $C_{L,total}$ = 1.86, and occurs at α = 14°.

Figure 25 shows the comparisons of spanloading (c_l) between the cruise wing configurations (configuration 12 with the fuselage/vtail and configuration 8 without the fuselage/vtail), as computed with USM3D SA. The c_l data in the plot of c_l as a function of y was normalized by the local chord (c), such that it skews the fuselage c_l compared to the other components due to the length of the fuselage. Therefore, the plot of $c * c_l$ was included to understand magnitude of lift on the fuselage as relative to the wing and stabilator. At $\alpha = 0°$, the comparisons between c_l on the wing for y > 50 in. are identical (fig. 25(a)). For y < 50 in., the effect of the fuselage on the stabilator increases the c_l (less negative) and decreases the c_l on the wing. In the region of 0 in. < y < 24 in., the lift on the fuselage is less than that of the wing section of configuration 8 that resides within the fuselage, but was modeled for the configuration without the fuselage. The wing+stabilator geometry (config. 8) has more lift for y < 24 in., but more negative lift on the stabilator for y < 40 in., compared to the full geometry (config. 12). The total lift coefficient at $\alpha = 0°$ is 0.6279 with the fuselage/vtail and 0.6669 without the fuselage/vtail (fig. 24(d)).

The total lift coefficients for configurations 8 and 12 at α = 11° are very similar (fig. 24(d)), but the spanloading distributions are somewhat different (fig. 25(b)). Both configurations have a loss of lift near y = 100 in. At this y location, just downstream of HLN10, a triangular-shaped, flow separation pattern, marked with dark blue skin friction contour values near 0 can be visualized in figure 26. Other large triangular-shaped separation patterns are seen downstream HLN7 for configuration 12, and downstream of HLN8 for configuration 8. These separation patterns correspond to the differences in the wing spanloading at approximately y = 30 in. and y = 60 in. At α =11°, the stabilator has positive c_l values, and the effect of the fuselage acts to decrease c_l for y < 25 in. Also, the lift from the fuselage for y < 25 in. is still less than the wing alone at α =11° (right side of fig. 25(b)).

However, at α = 12°, the sectional lift from the fuselage for y < 25 in. is more than the wing section, but the fuselage still has a negative effect on the stabilator and decreases c_l for y < 25 in. (fig. 25(c)). Figure 24(d) shows that the lift coefficient for the full geometry (config. 12) increases at α = 12°, while the lift coefficient for the wing+stabilator (config. 8) decreases slightly. Figure 27 shows the Mach contours at a plane of y = 60 inches and surface pressure coefficient for configurations 8 and 12. There is a larger region of blue Mach contours in the y = 60 in. plane (fig. 27(a)) as the flow separation between 30 in. < y < 120 in. moves upstream toward the leading edge and the sectional lift decreases (fig. 25(c)) for configuration 8, compared to configuration 12 with a much smaller region of separated flow visualized as blue Mach contours in figure 27(b).

As the angle of attack is increased to α =13°, the large region of flow separation for configuration 8 at α =12° is reduced and the sectional lift coefficient distribution moves to higher values and matches configuration 12 well (fig. 25(d)). A possible explanation for the change in flow separation for configuration 8 without the fuselage, is that vortices shedding off the high-lift nacelles may be hitting the leading edge to cause the large flow separation at α = 12°, but at α = 13°, the vortices pass above the leading edge and do not disturb the boundary layer flow. At α = 13°, the sectional lift from the fuselage for y < 10 in. is higher than the wing alone.

Figure 28 shows the Mach contours for a y-z plane at x = 155 inches and the surface pressure coefficient (left), and surface skin friction coefficient (right) for the full geometry (config. 12) at α = 14°, α = 15°, and α = 16°. The maximum lift coefficient, $C_{L,total}$ = 2.07, for the full geometry occurs at α =14° and the flow contours are shown in figure 28(a). At α =15°, the flow separates at the wingroot-fuselage intersection as seen as dark blue Mach contours at x = 155 inches (left side fig. 28(b)), dark blue skin friction coefficient values near 0 (right side fig. 28(b)), and in the drop of sectional lift coefficient between 18 in. < y < 40 in (fig. 25(e)). With further increase in angle of attack to 16°, another large region of flow separation occurs on the wing between HLN9 and HLN10 (fig. 28(c)) and the total lift coefficient drops to $C_{L,total}$ = 1.98.

To understand if the SA turbulence model might have exaggerated flow separation at high angles of attack, the SA DES model was also used to compute the flow solutions at 11° < α < 16° and compare with the SA results. The effect of turbulence model on lift coefficient without the contribution of the stabilator ($C_{L,total} - C_{L,hstab}$) and on total lift for USM3D solutions of the full geometry are shown in figure 29. The lift coefficient compares well between the two codes at α = 11°, however, the solution C_p contours (fig. 30) are different with the SA model predicting more flow separation (less negative C_p contours) downstream of several HLN (3, 6, 7, 10), than with the SA DES model. The comparison of the semispan sectional lift coefficient is shown in figure 31 and indicates the SA solution has a lower c_l around y = 32 in. (HLN7) and y = 102 in. (HLN10). However, the lift is higher with the SA model for 40 in. < y < 80 in. and y > 130 in. Additionally, the c_l is the same between the two models on the stabilator and fuselage. Both turbulence models predict maximum wing+fuselage lift ($C_{L,total} - C_{L,hstab}$) at α = 14°, with a value of 1.86 for SA and 1.60 for SA DES (fig. 29(a)). The higher lift coefficient for SA is visualized through differences in surface pressure coefficient and Mach contour (x = 165 in.) comparisons in figure 32. The SA DES, with lower lift, has more flow separation upstream, at locations outboard near the tip nacelle and downstream of several HLNs, as indicated with blue Mach contours and green C_p contours, where the flow does not expand to the same negative C_p values as with the SA model. The difference in lift is further illustrated in the spanloading comparisons in figure 33, with much higher c_l across the wing span for the SA solution, compared to the SA DES solution. The SA DES model predicts a slightly higher c_l across the stabilator and slightly lower c_l across the fuselage.

In an effort to corroborate the SA DES results, predicting lower lift coefficients than the SA model at high angles of attack, a second CFD code was used, Kestrel. The same tetrahedral mesh used for USM3D was used for Kestrel, but with the tetrahedral cells in the boundary layer converted to prisms, as recommended by the Kestrel support team. The comparisons of lift, drag, and pitching moment coefficients between USM3D and Kestrel for the full configuration are shown in Table 4. First, the comparisons between the codes are very good with both codes using the SA turbulence model. There are small differences in the implementation of the SA model in each code, so some small differences are expected. The lift coefficient was within 1 percent for both $\alpha = 0°$ and $\alpha = 15°$ using the SA turbulence model. The difference in lift coefficient without the contribution of the stabilator, between the two codes with SA, was 0.0001 for $\alpha = 0°$, indicating that most of the differences between the codes is occurring on the stabilator. However, at $\alpha = 15°$ the difference in total lift coefficient and lift coefficient without the contribution of the stabilator is about the same for both SA and DES models. The total drag from Kestrel SA was 28.2 counts higher at $\alpha = 0°$ and 82.7 counts higher at $\alpha = 15°$. At $\alpha = 0°$, the difference in counts of drag by components is 11.7 counts on the fuselage, 8.9 on the vtail, 2.5 on the stabilator, 1.6 on the HLN, 1.3 on the landing gear cover, 1 on the tip nacelles, and 1.2 on the wing. The grid resolution on the wing has evolved and improved from grid 1 to 12 and there is only 1.2 count difference between the two codes. When the fuselage and vtail were added to the wing+stabilator geometry, the same criteria and gridding techniques were used and a few cycles of grid improvements were made. However, a full grid study was not completed until after this work with an updated version of the HLN. Based on the grid study, finer grid resolution has been requested on the fuselage and vtail for the next set of grids, which include the version 4.1.5.2 HLN for the final X-57 configuration. As expected with the close comparisons of lift, drag, and pitching moment coefficients, the flow contours look similar as well for the SA turbulence model solutions. Figure 34 shows the nearly identical pressure coefficient contours on the upper surface of the configuration at $\alpha = 0°$. Figure 35 shows the surface pressure coefficient contours on the left side and skin friction coefficient contours on the right side for $\alpha = 15°$. Both codes predict large flow separation on the inboard wing (between HLN6 and HLN7) near the fuselage, and flow separation slightly further upstream between HLN3 to HLN4, and HLN9 to HLN10, than along the rest of the wing $\alpha = 15°$ with the SA turbulence model. At $\alpha = 15°$, the difference in counts of drag between the two codes is larger than at $\alpha = 0°$ due to more unsteady flow separation on the wing; 33.6 count difference on wing and 24.0 count difference on the fuselage.

Table 4. Lift, Drag, and Pitching Moment Coefficients Predicted with USM3D and KESTREL, Full Configuration with the Cruise Wing

CFD CODE	Turbulence Model	α, °	$C_{L,total}$	$C_{L,total} - C_{L,stab}$	$C_{D,total}$	$C_{m,total}$
USM3D	SA	0	0.6278	0.6745	0.0482	0.1516
Kestrel	SA	0	0.6313	0.6746	0.0511	0.1218
USM3D	SA	15	2.0570	1.8078	0.2493	-1.1563
Kestrel	SA	15	2.0377	1.7858	0.2576	-1.1918
USM3D	SA DES	15	1.8217	1.5775	0.2497	-1.1505
Kestrel	SA DDES	15	1.9998	1.7778	0.2398	-0.9392

With good comparisons achieved between the codes using the SA turbulence model, the Kestrel code was also run with SA DDES. Unfortunately, USM3D only has DES and Kestrel only has DDES. Therefore, some differences are expected between the USM3D SA DES and Kestrel SA DDES solutions, but the DDES is a newer model that can detect the edge of the boundary layer and delays the transition to LES outside of the boundary layer. The expectation then, is that the SA DDES is a better prediction. Table 4 shows a larger difference between the DES and the DDES solutions than with SA turbulence model. The DDES has 9.5 percent higher lift, 99 counts lower drag, and a 19 percent lower pitching moment than DES. The differences are visualized in figure 36, which shows the contours of pressure coefficient (left) and skin friction coefficient (right). The midspan flow separation between HLN 3 to 4, and 9 to 10 is further upstream for DES (fig. 36(a)), than with DDES (fig. 36(b)). The flow separation near the wingtip nacelle is similar between the two turbulence models. Additionally, both CFD codes (with DES and DDES) predict similar flow between HLN6 and HLN7, with what looks to be streaks in skin friction coefficient, along the wing-fuselage intersection, where two vortices (on each side of the fuselage) are shedding off the wingroot leading

edge and traveling downstream, one along the fuselage and one along the wing. The flow between HLN6 and HLN7 from the DES and DDES models (fig. 36), is much different than that predicted with the SA model (fig. 35).

V. Conclusions

The X-57 Maxwell was designed with a small, high aspect ratio cruise wing yielding a high cruise lift coefficient (C_L = 0.75) at α = 0°.

The conditions for all of the cruise wing cases were computed at 150 KTAS, *Re* = 2.83 million, h = 8000 ft, and T = 30.5°F. At the cruise lift coefficient of $C_{L,total}$ = 0.75, the total drag was $C_{D,total}$ = 0.0517 for an α = 0.91°. This computational data indicates that the X-57 full aircraft drag would meet the goal with a 25 count drag margin. Of course, the real aircraft, with rivets and skin surface intersections, will have some drag that is not modeled in the smooth computational geometry. However, this is an excellent position to now have the full geometry modeled and be under the total aircraft drag estimate by 25 counts and still have some possible savings with power and laminar flow to offset any drag additions for the real, as-built aircraft.

For the USM3D SA solutions for the full cruise geometry (config. 12), the maximum lift is $C_{L,total}$ = 2.07 and $C_{L,total} - C_{L,hstab}$ = 1.86 at α = 14°. Using the more advanced turbulence model of DDES for high angles of attack, the lift for the full cruise geometry (config. 12) without the stabilator lift contribution is $C_{L,total}$ = 1.78 at α = 15°, but a full angle-of-attack sweep was not computed. Thus, it is unknown if $C_{L,total}$ = 1.78 is the maximum lift possible from the DDES turbulence model.

Unfortunately, the full geometry with the high-lift wing has not been completed yet. The conditions for all of the high-lift wing (with 30° flap deflection) cases were at the design stall speed of 58 KTAS, *Re* = 1.33 million, h = 0 ft, and T = 59°F. For the unblown high-lift wing, the maximum lift coefficient excluding the stabilator is 2.600 at α = 13°. For the high-lift blowing cases, the total lift includes the contribution of the propellers. For high-lift blowing conditions, the maximum lift coefficient excluding the stabilator is 4.426, at α = 13°. Although this is not the full geometry (fuselage and vertical tail excluded), the computational analysis is predicting that the required lift coefficient of 3.95, for a stall speed of 58 knots, is met with some margin for possible loss of lift when including the fuselage and vertical tail. The lift augmentation from the high-lift propellers is 1.7, computed by dividing 4.426 by 2.600. The lift augmentation from the high-lift system (30° flap deflection and the high-lift blowing) is 2.39 computed by dividing the maximum lift coefficient with high-lift blowing, 4.426, by the maximum lift of the cruise wing 1.86. The drag for the high-lift wing with 30° flap deflection geometry is much higher than the cruise wing configuration, but the high-lift system is used only during a small portion of the flight envelope. The drag at maximum lift is C_D = 0.6732 with high-lift blowing, but the minimum drag with high-lift blowing is C_D = 0.2550 for $C_{L,total}$ = 2.5389 at α = 0°. The pitching moment is relatively constant when the stabilator is excluded, for both the blown-wing and the unblown-wing conditions.

Modeling the full cruise wing geometry (where the fuselage and vertical tail were included) has indicated some adverse effects on the wing and stabilator at the design cruise speed of 150 KTAS. At high angles of attack, the solutions with USM3D SA model indicates large flow separation on the wing upper surface between the two high-lift nacelles near the fuselage (high-lift nacelles 6 and 7), and also a reduction in sectional lift on the stabilator to about 50 percent of the stabilator span. However, the large flow separation between high-lift nacelles 6 and 7 is mostly eliminated in the solutions predicted with two codes, USM3D and Kestrel, using detatched eddy simulation and delayed detatched eddy simulation turbulence model, respectively.

References:

1. Borer, Patterson, Viken, Moore, Clarke, Redifer, Christie, Stoll, Dubois, Bevirt, Gibson, Foster, Osterkamp: "Design and Performance of the NASA SCEPTOR Distributed Electric Propulsion Flight Demonstrator," Aviation Forum in Washington D. C., AIAA 2016-3920, 13-17 June 2016.
2. Biedron, R. T., Carlson, J. R., Derlaga, J. M., Gnoffo, P. A., Hammond, D. P., Jones, W. T., Kleb, B., Lee-Rausch, E. M., Nielsen, E. J., Park, M. A., Rumsey, C. L., Thomas, J. L., and Wood, W. A.: "FUN3D Manual: 13.0," NASA TM-2016-219330.
3. Frink, N. T.: "Tetrahedral Unstructured Navier-Stokes Method for Turbulent Flow," AIAA Journal, Vol. 36, No. 11, Nov. 1998, pp. 1975-1982.
4. Frink, N. T., Pirzadeh, S. Z., Parikh, P. C., Pandya, M. J., and Bhat, M. K.: "The NASA Tetrahedral Unstructured Software System," The Aeronautical Journal, Vol. 104, No. 1040, October 2000, pp. 491-499.
5. Pandya, M. J., Abdol-Hamid, K. S., and Parlette, E. B.: "CFD Computations for a Generic High-Lift Configuration Using TetrUSS," 29th AIAA Applied Aerodynamics Conference, AIAA 2011-3008, 27-30 June 2011.
6. Morton, S. A., McDaniel, D. R., Sears, D. R., Tillman, B., and Tuckey, T. R.: "Kestrel – A Fixed Wing Virtual Aircraft Product of the CREATE Program," 47th AIAA Aerospace Sciences Meeting, A1AA 2009-338, 5-8 January 2009.
7. Morton, S. A.: "HPCMP CREATE™-AV Kestrel Current Capabilities and Future Direction for Fixed-Wing Aircraft Simulations," 53rd AIAA Aerospace Sciences Meeting, SciTech Forum, AIAA 2015-0039, 5-9 January 2015.
8. Deere, K. A., Viken, S. A., Carter, M. B., Viken, J. K., Derlaga, J. M., Stoll, A. M.: "Comparison of High-Fidelity Computational Tools for Wing Design of a Distributed Electric Propulsion Aircraft," AIAA2017-3925, AIAA Aviation Forum, Denver, Colorado, 5-9 June 2017.
9. Spalart, P. R.; and Allmaras, S. R.: *A One-Equation Turbulence Model for Aerodynamic Flows*. Recherché, No. 1, 1994, pp. 5-21.
10. Shur, M. L., Strelets, M. K., Travin, A. K., Spalart, P. R.: "Turbulence Modeling in Rotating and Curved Channels: Assessing the Spalart-Shur Correction," AIAA Journal Vol. 38, No. 5, 2000, pp. 784-792.
11. Spalart, P. R.: "Strategies for Turbulence Modeling and Simulation," International Journal of Heat and Fluid Flow, Vol. 21, 2000, pp. 252-263.
12. Menter, F. R.: "Two-Equation Eddy-Viscosity Turbulence Models for Engineering Applications," AIAA Journal, vol. 32, no. 8, Aug. 1994, pp. 1598– 1605.
13. Pandya, M. J.; Abdol-Hamid, K. S.; and Parlette, E. B.: "CFD Computations for a Generic High-Lift Configuration Using TetrUSS," 29th AIAA Applied Aerodynamics Conference, AIAA 2011-3008, 27-30 June 2011.
14. Langtry, R.B., Menter, F.R., Likki, S.R., Suzen, Y.B., Huang, P.G., and Völker, S.: "A Correlation based Transition Model using Local Variables Part 2 - Test Cases and Industrial Applications," ASME-GT2004-53454, ASME TURBO EXPO 2004, Vienna, Austria.
15. Langtry, R.B., and Menter, F.R.: "Transition Modeling for General CFD Applications in Aeronautics," AIAA paper 2005-522, 2005.
16. Pandya, M. J.; Frink, N. T.; Abdol-Hamid, K. S.; and Chung, J. J.: "Recent Enhancements to USM3D Unstructured Flow Solver for Unsteady Flows," 22nd AIAA Applied Aerodynamics Conference and Exhibit, AIAA 2004-5201, 16-19 June 2004.
17. Spalart, P. R., Deck, S., Shur, M. L., Squires, K. D., Strelets, M. K., and Travin, A., "A New Version of Detached-Eddy Simulation, Resistant to Ambiguous Grid Densities," Theory Computational Fluid Dynamics, Vol. 20, 2006, pp. 181-195.
18. "2nd AIAA CFD High Lift Prediction Workshop Gridding Guidelines," http://hiliftpw.larc.nasa.gov, https://hiliftpw.larc.nasa.gov/Workshop2/GriddingGuidelines-HiLiftPW2-v2.pdf, March 2013.
19. Pirzadeh, S.: "Advanced Unstructured Grid Generation for Complex Aerodynamics Applications," AIAA 2008-7178, 26th AIAA Applied Aerodynamics Conference, August 2008.
20. Pirzadeh, S.: "Three-dimensional unstructured Viscous Grids by the Advancing-Layers Method," AIAA Journal, Vol. 34, No. 1, January 1996, pp. 43-49.

21. Deere, K. A., Viken, S. A., Carter, M. B., Viken, J. K., Wiese, M. R., and Farr, N.: "Computational Analysis of Powered Lift Augmentation for the LEAPTech Distributed Electric Propulsion Wing," AIAA2017-3921, AIAA Aviation Forum, Denver, Colorado, 5-9 June 2017.
22. Drela, M., and Youngren, H.: XROTOR Download Page, http://web.mit.edu/drela/Public/web/xrotor/, accessed 6 May 2014.
23. Goldstein, S.: "On the Vortex Theory of Screw Propellers," Proceeding of the Royal Society of London A: Mathematical, Physical and Engineering Sciences, vol. 792, no. 123, Apr. 1929, pp. 440–465.
24. Stern, F., Kim, H. T., and Patel, V. C.: "A Viscous-Flow Approach to the Computation of Propeller-Hull Interaction," Journal of Ship Research, vol. 32, no. 4, Dec. 1988, pp. 246–262.
25. Perkins, Courtland D., Hage, Robert E.: m "Airplane Performance Stability and Control," Wiley, 1967.
26. Deere, K. A., Viken, J. K., Viken, S. A., Carter, M. B., Wiese, M. R.; and Farr, N.: "Computational Analysis of a Wing Designed for the X-57 Distributed Electric Propulsion Aircraft," AIAA2017-3923, AIAA Aviation Forum, Denver, Colorado, 5-9 June 2017.

Figure 1. The original Tecnam P2006T aircraft without engines.

Figure 2. The X-57 Maxwell DEP aircraft. The Tecnam P2006T fuselage, vertical tail and stabilator with the DEP wing system that includes the wingtip propulsors and the DEP high-lift motors.

(a) Front, looking aft

(b) Aft, looking forward, with negative tab deflection

Figure 3. A 42-percent scale model of the stabilator for the X-57 Maxwell DEP aircraft in the NASA Langley Research Center 12-Foot Low Speed Tunnel.

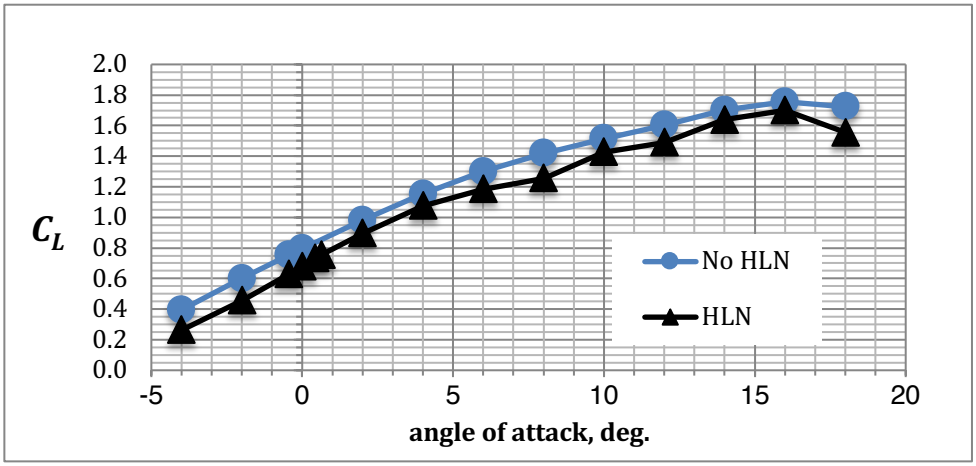

(a) Unpowered cruise wing at 150 KTAS, *Re* = 2.83 million, h = 8000 ft, T = 30.5°F

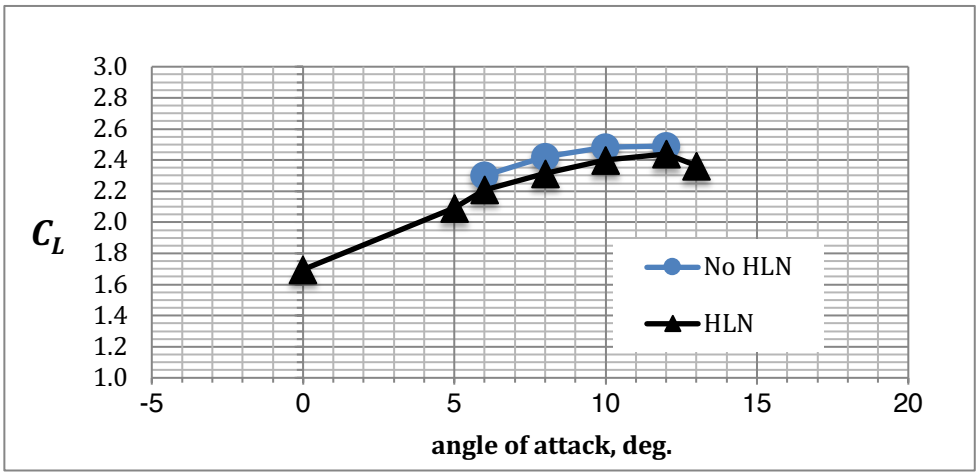

(b) Unblown high-lift wing (30° flap deflection) at 58 KTAS, *Re* = 1.33 million, h = 0 ft, T = 59°F

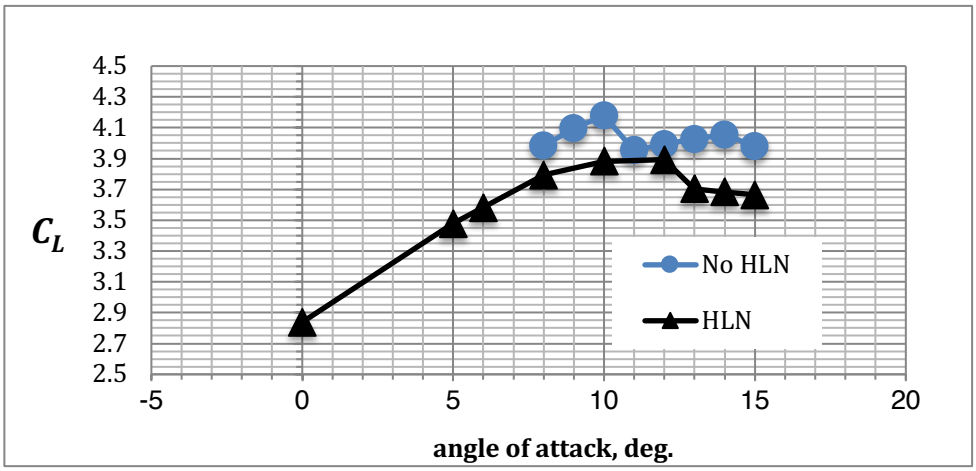

(c) Blown high-lift wing (30° flap deflection) at 58 KTAS, *Re* = 1.33 million, h = 0 ft, T = 59°F, and 13.7hp/prop

Figure 4. The impact of the high-lift nacelles on the lift coefficient using FUN3D SA-RC-QCR2000.

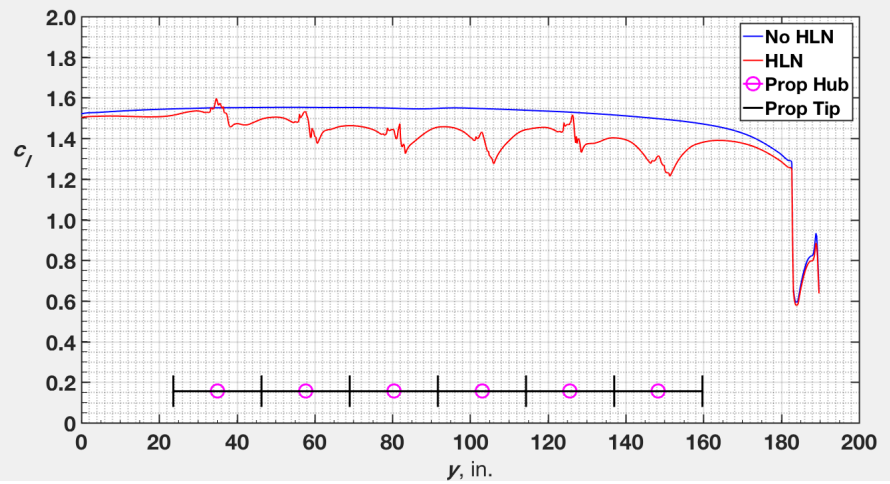

(a) Unpowered cruise wing at 150 KTAS, *Re*= 2.83 million, h = 8000 ft, T = 30.5°F

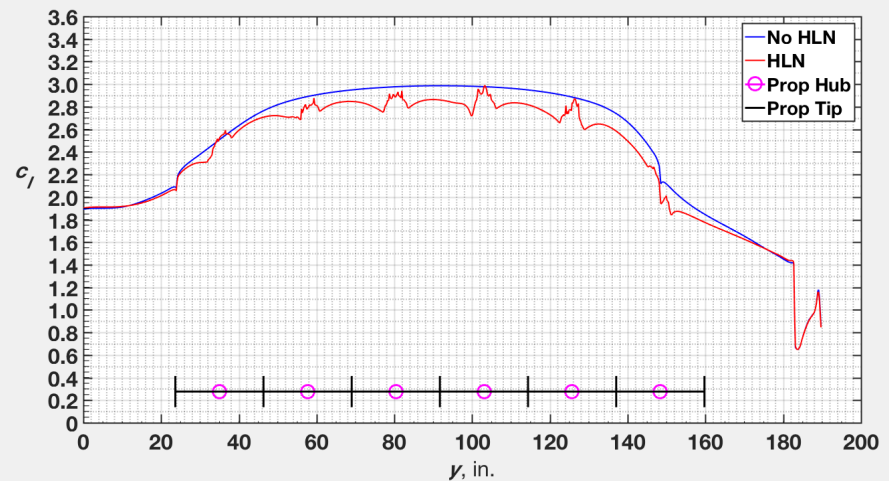

(b) Unblown high-lift wing (30° flap deflection) at 58 KTAS, *Re* = 1.33 million, h = 0 ft, T = 59°F

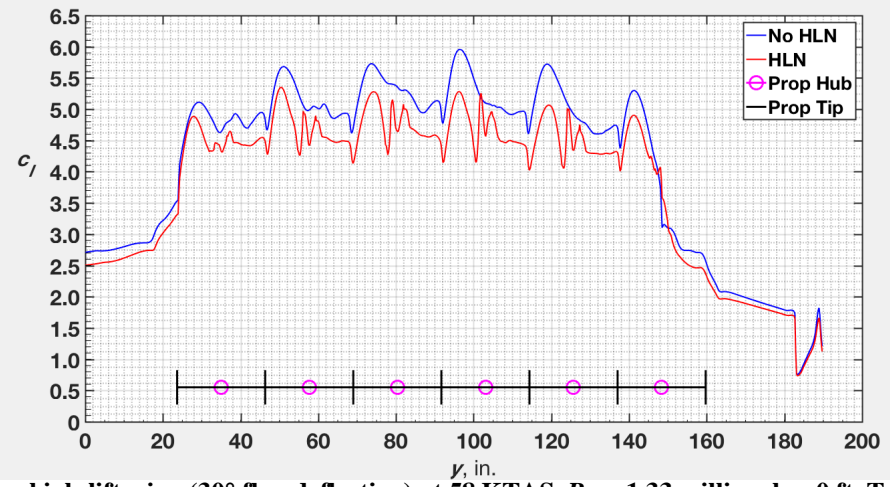

(c) Blown high-lift wing (30° flap deflection) at 58 KTAS, *Re* = 1.33 million, h = 0 ft, T = 59°F, 13.7hp/prop

Figure 5. The impact of the high-lift nacelles on sectional lift coefficient at α = 10° using FUN3D SA-RC-QCR2000. (Blue, without HLN; Red, with HLN).

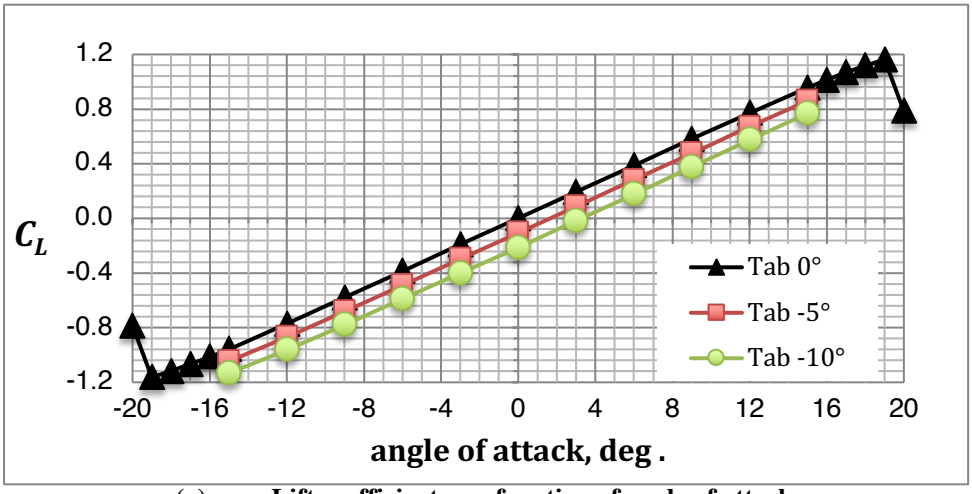

(a) Lift coefficient as a function of angle of attack

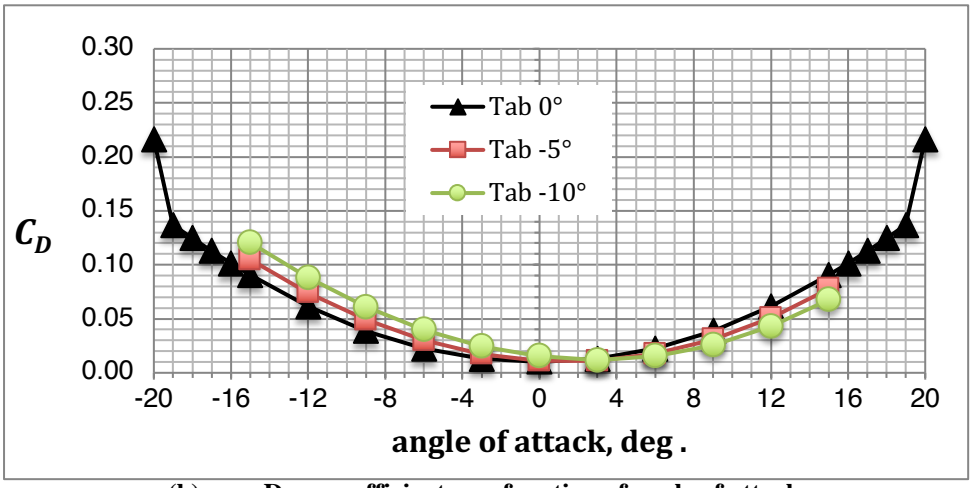

(b) Drag coefficient as a function of angle of attack

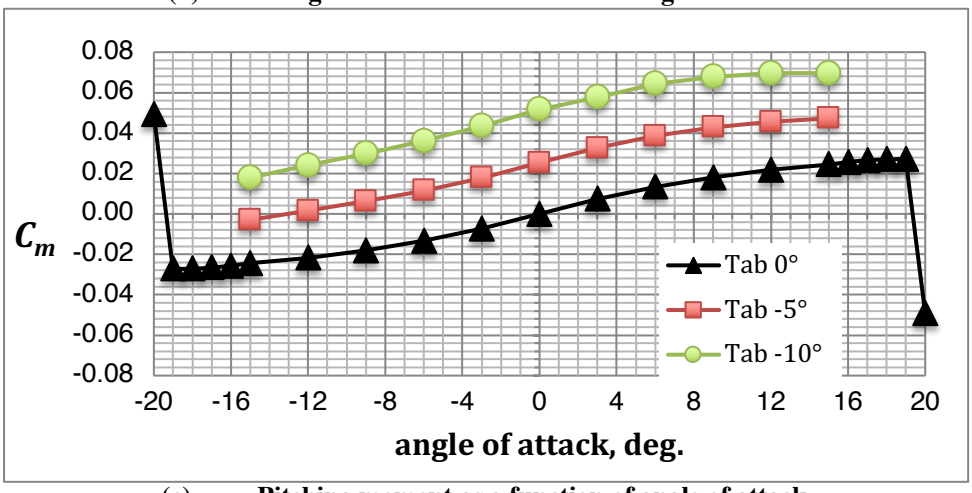

(c) Pitching moment as a function of angle of attack

Figure 6. The lift, drag and pitching moment coefficients from USM3D SA solutions of the stabilator at 58 KTAS, *Re* = 1.3 million, h = 0 ft, and T = 59°F.

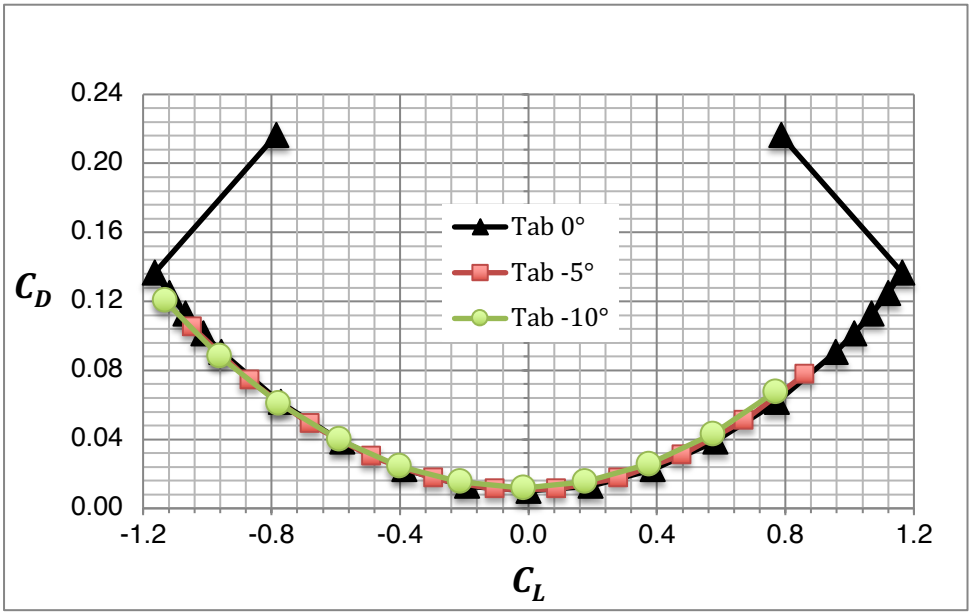

(d) Drag coefficient as a function of lift coefficient

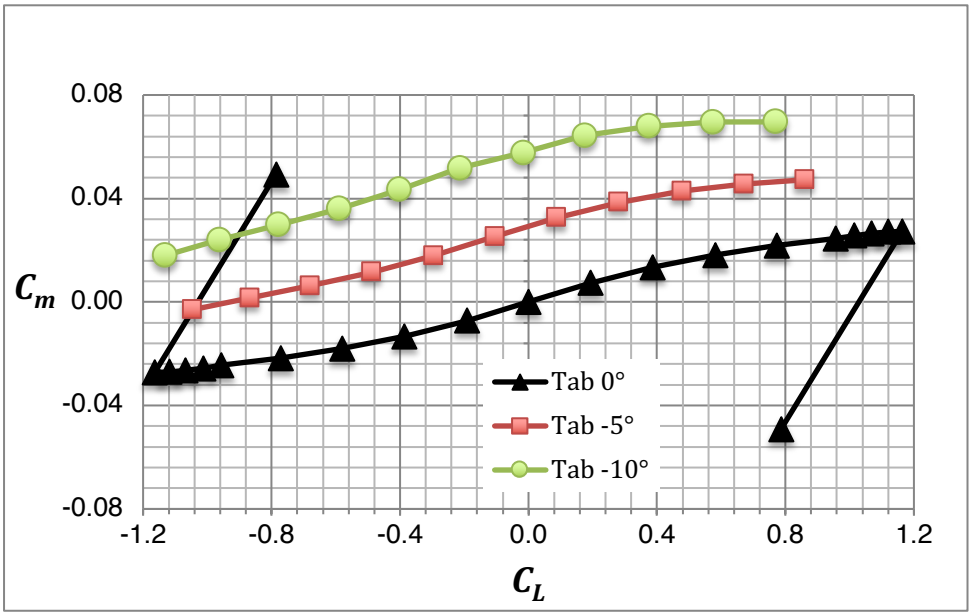

(e) Pitching moment coefficient as a function of lift coefficient

Figure 6 Continued. The lift, drag and pitching moment coefficients from USM3D SA solutions of the stabilator at 58 KTAS, *Re* = 1.3 million, h = 0 ft, and T = 59°F.

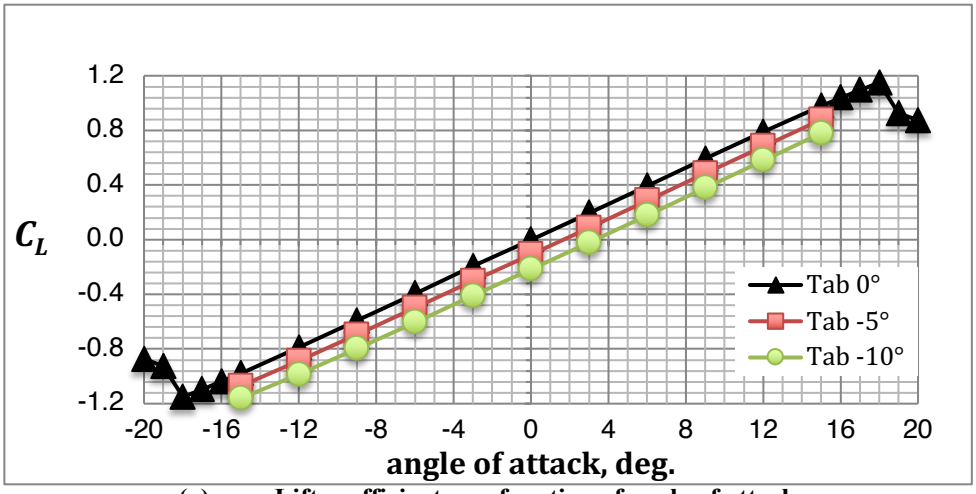

(a) Lift coefficient as a function of angle of attack

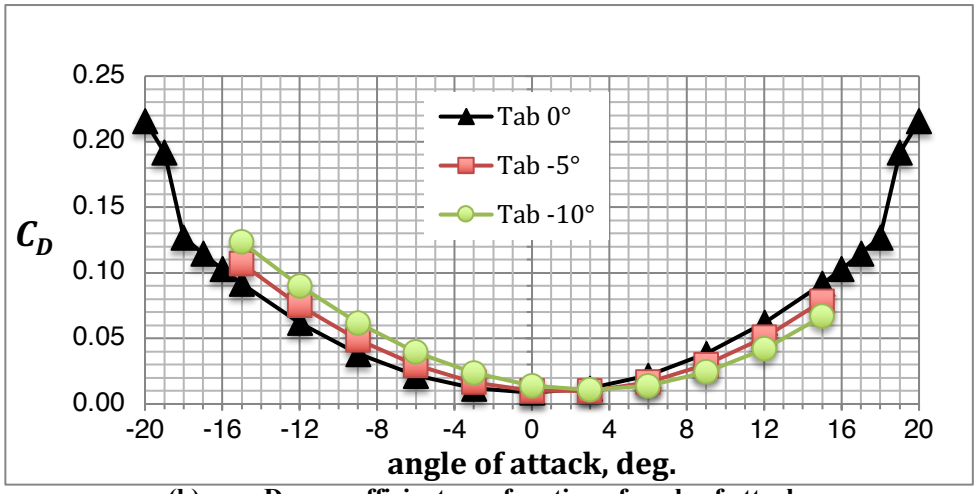

(b) Drag coefficient as a function of angle of attack

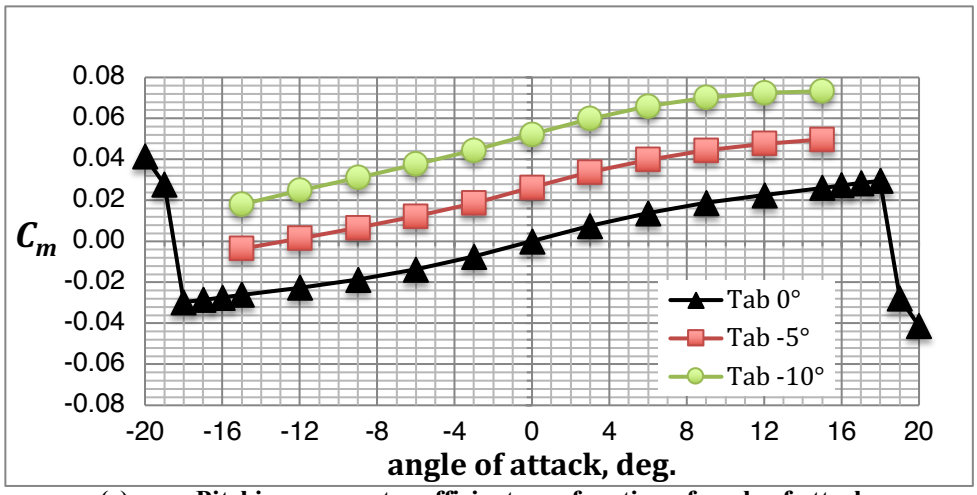

(c) Pitching moment coefficient as a function of angle of attack

Figure 7. The lift, drag, and pitching moment coefficients from USM3D SA of the stabilator at 150 KTAS, *Re* = 2.83 million, h = 8000 ft, and T = 30.5°F.

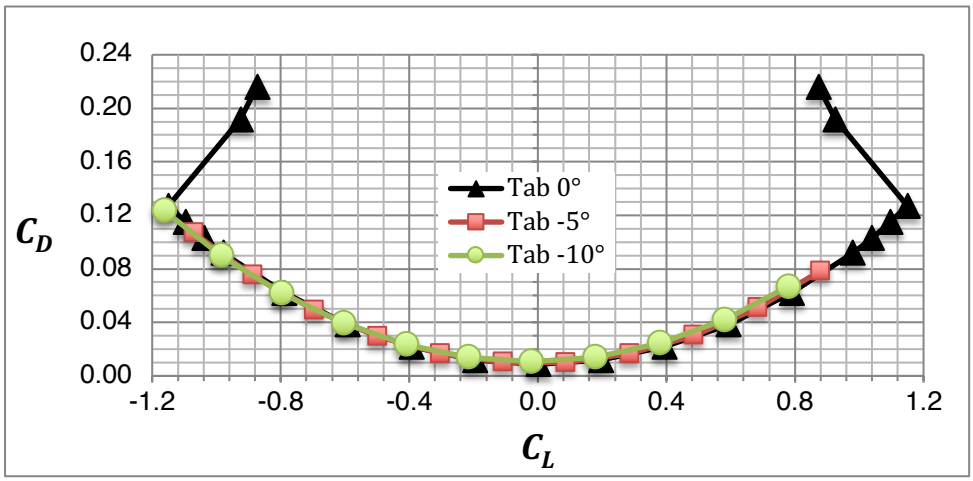

(d) Drag coefficient as a function of lift coefficient

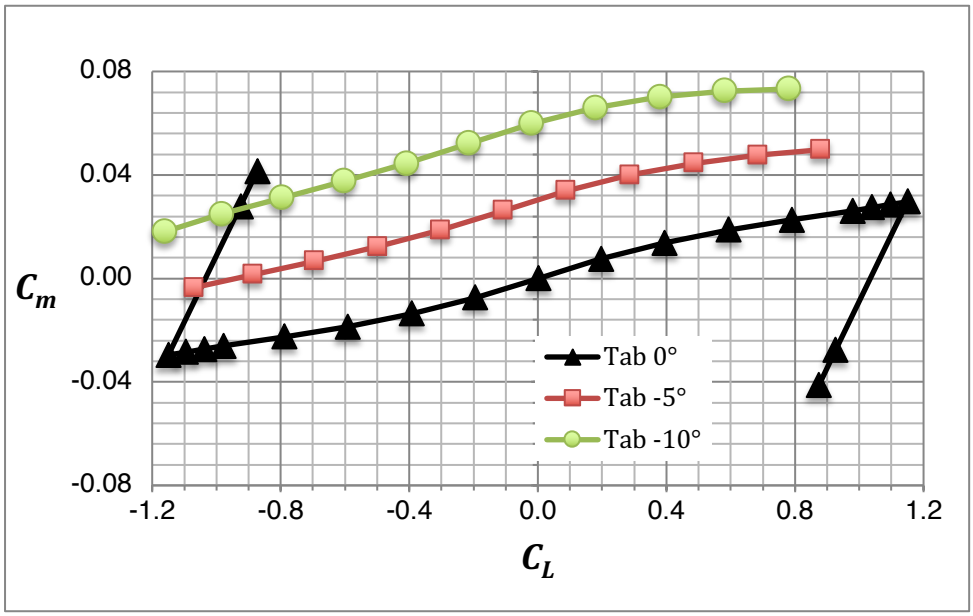

(e) Pitching moment coefficient as a function of lift coefficient

Figure 7 Continued. The lift, drag, and pitching moment coefficients from USM3D SA of the stabilator at 150 KTAS, *Re* = 2.83 million, h = 8000 ft, and T = 30.5°F.

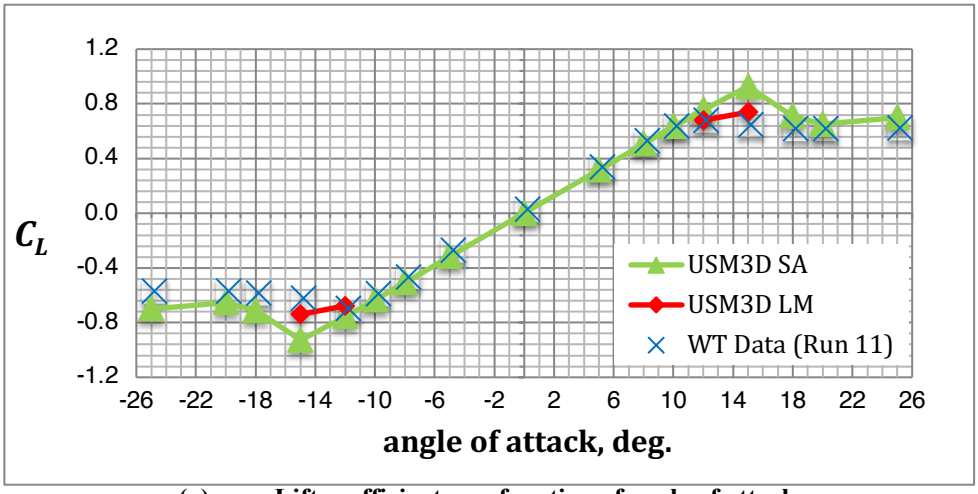

(a) Lift coefficient as a function of angle of attack

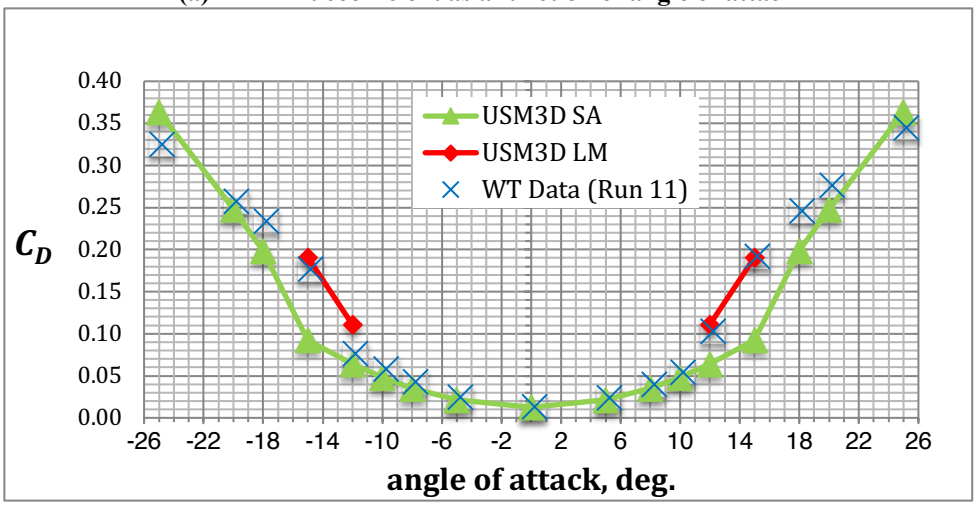

(b) Drag coefficient as a function of angle of attack

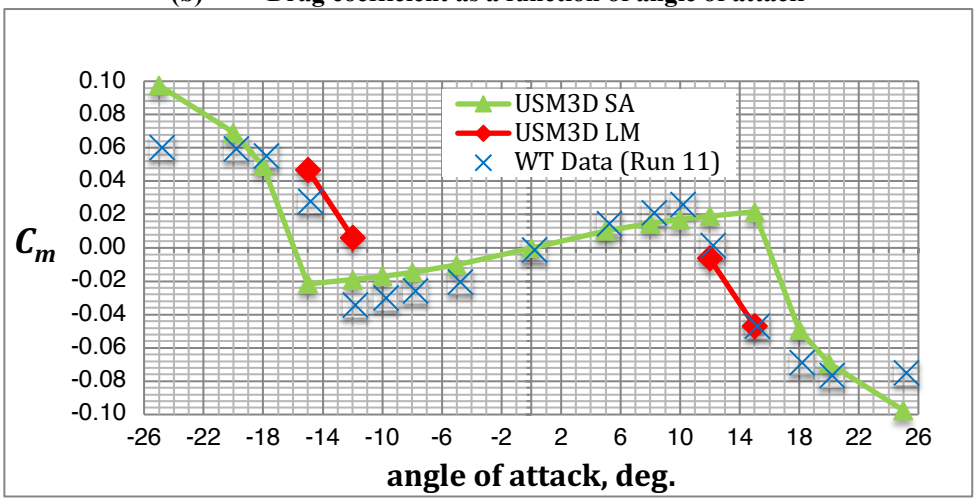

(c) Pitching moment coefficient as a function of angle of attack

Figure 8. The lift, drag, and pitching moment coefficients for the stabilator at 34 KTAS, wind tunnel *Re* = 0.38 million, h = 0 ft, and T = 72.9°F. USM3D fully turbulent solutions with SA and USM3D transitional flow solutions with LM for CFD.

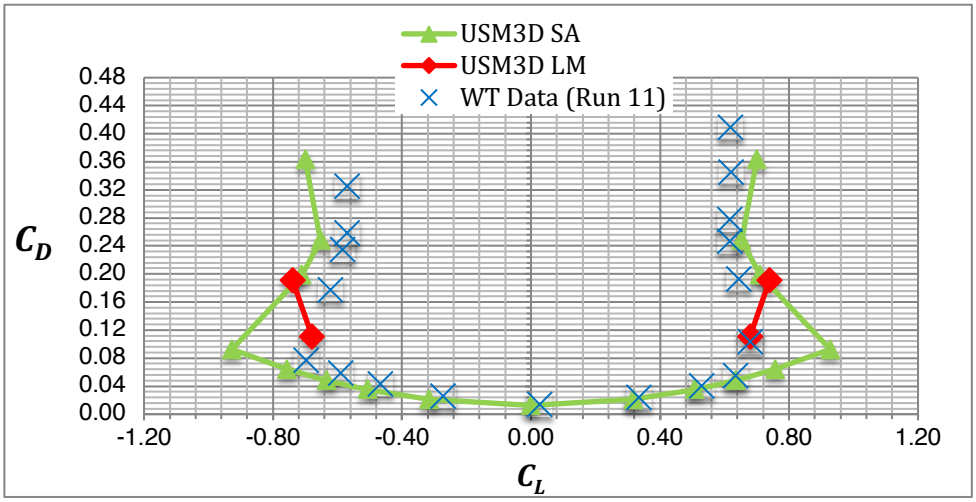

(d) Drag coefficient as a function of lift coefficient

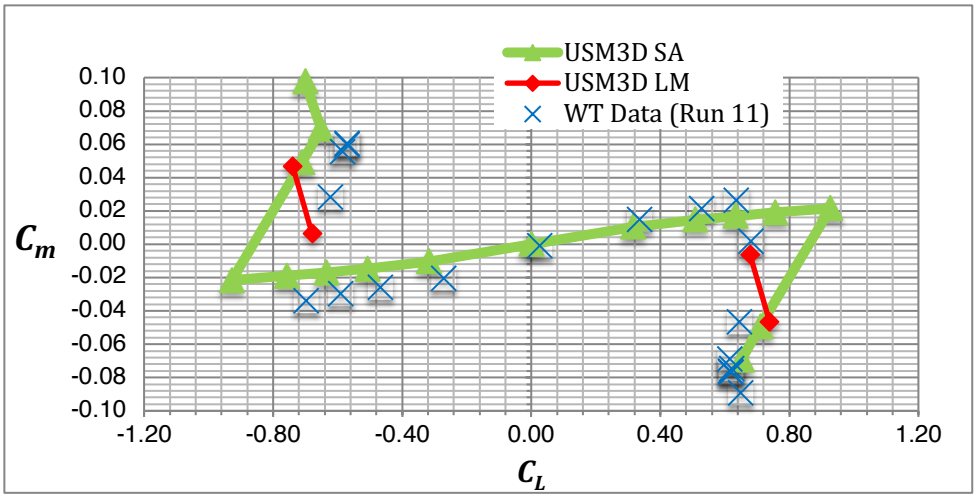

(e) Pitching moment coefficient as a function of lift coefficient

Figure 8 Continued. The lift, drag, and pitching moment coefficients for the stabilator at 34 KTAS, wind tunnel *Re* = 0.38 million, h = 0 ft, and T = 72.9°F. USM3D fully turbulent solutions with SA and USM3D transitional flow solutions with LM for CFD.

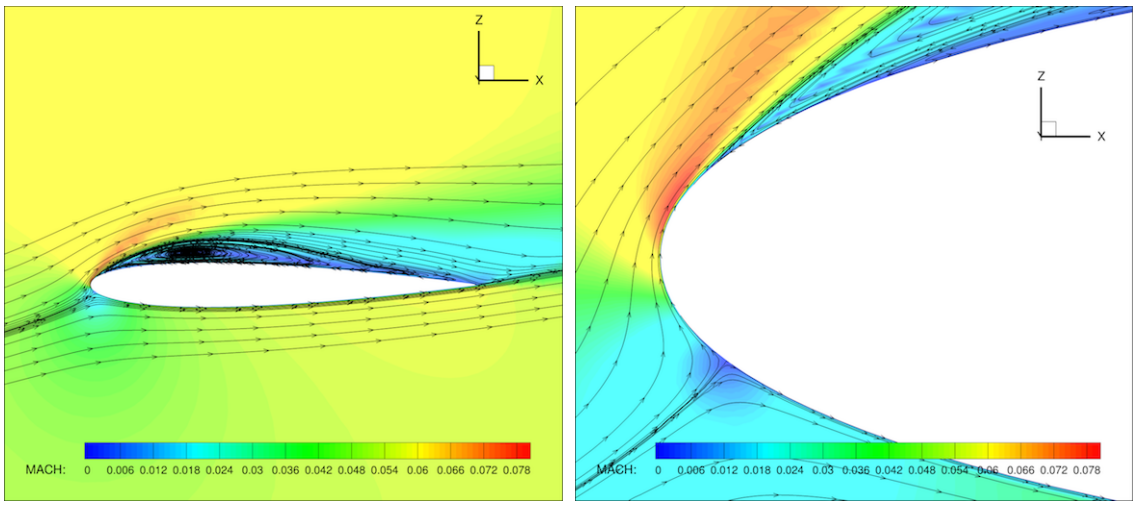

(a) LM transition model

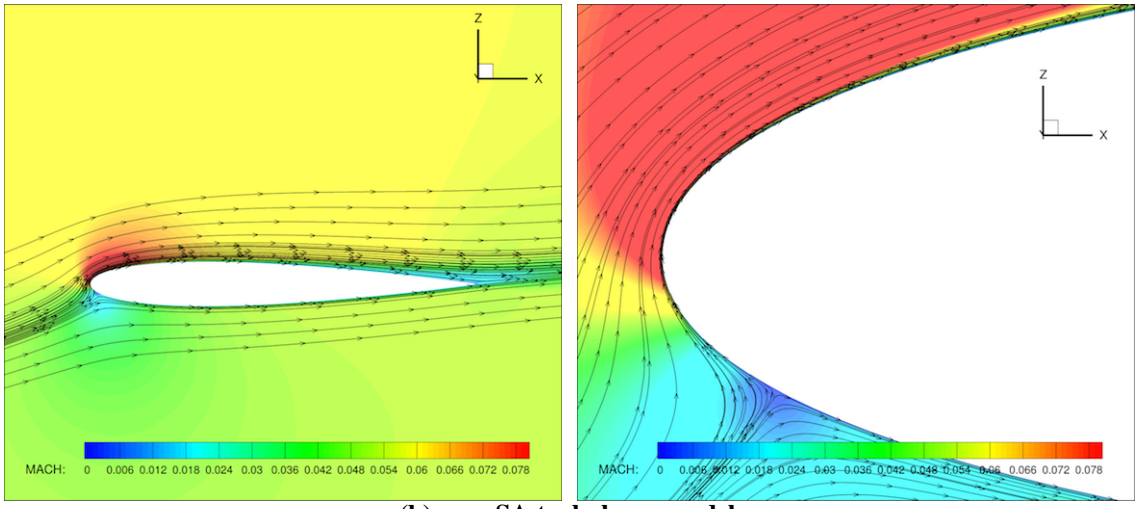

(b) SA turbulence model

Figure 9. The Mach contours at y = 10 inches along the stabilator at 34.4 KTAS, α = 12°, wind tunnel *Re* = 0.38 million, h = 0 ft, and T = 72.9°F. USM3D solutions.

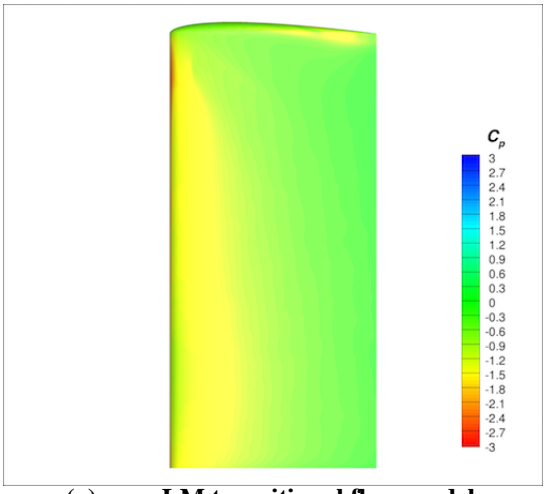

(a) LM transitional flow model

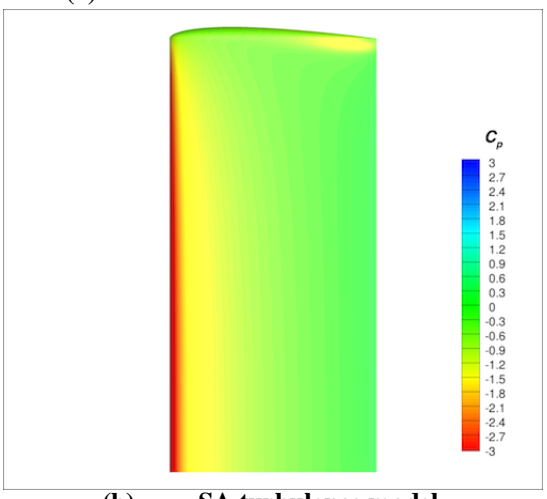

(b) SA turbulence model

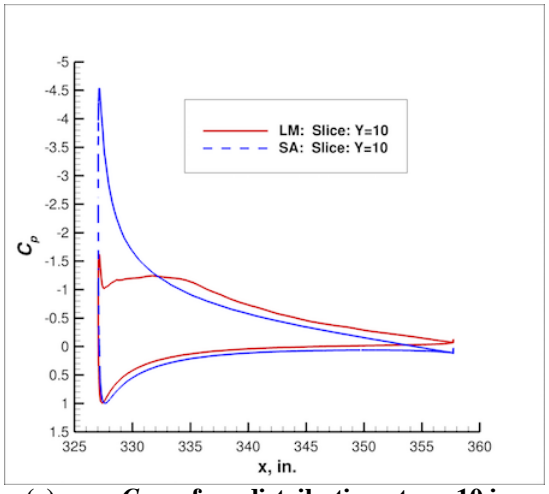

(c) C_p surface distribution at y = 10 in.

Figure 10. The surface pressure coefficient contours and distribution at y = 10 in. on the stabilator at 34.4 KTAS, α = 12°, wind tunnel *Re* = 0.38 million, h = 0 ft, and T = 72.9°F. USM3D solutions.

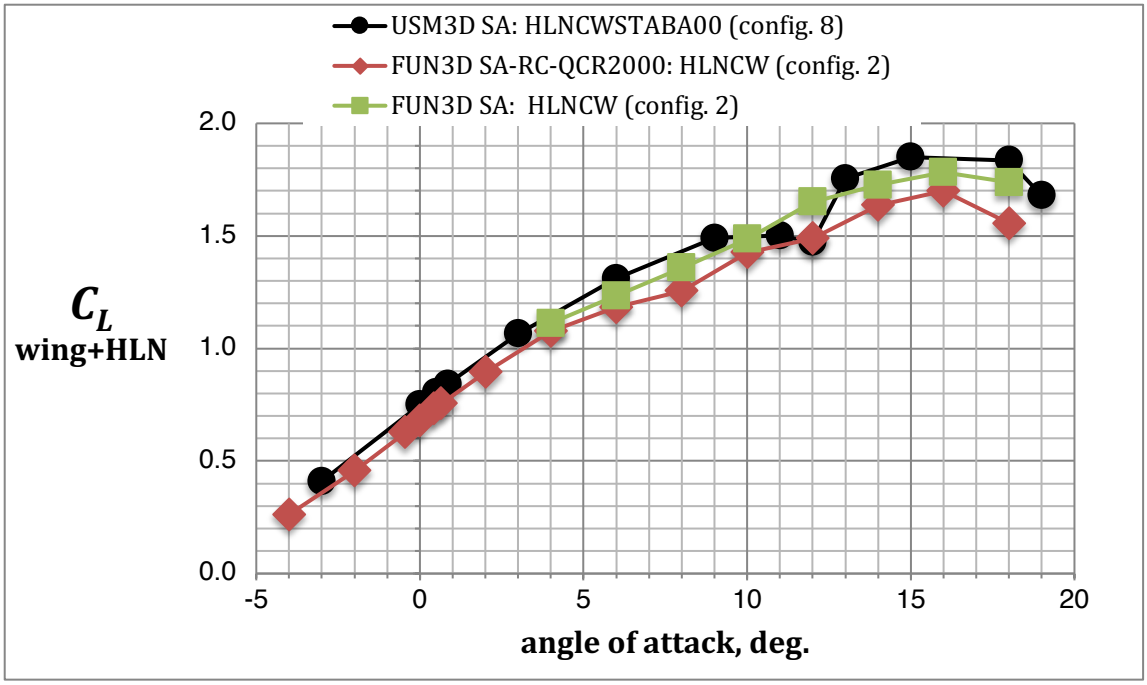

(a) Cruise wing at 150 KTAS, *Re* = 2.83 million, h = 8000 ft, T = 30.5°F.

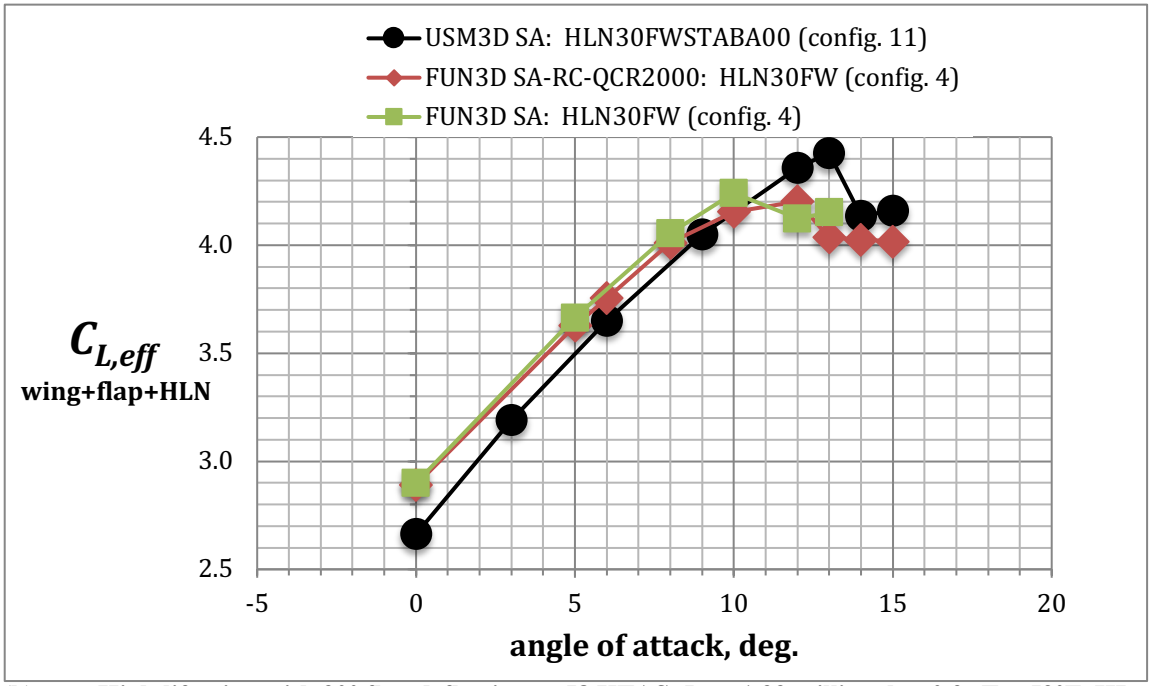

(b) High-lift wing with 30° flap deflection at 58 KTAS, *Re* = 1.33 million, h = 0 ft, T = 59°F, HL blowing (13.7 hp/prop).

Figure 11. FUN3D and USM3D code comparisons of wing lift coefficient (stabilator contribution to lift excluded) for the cruise wing and the high-lift wing with 30° flap deflection and with high-lift blowing.

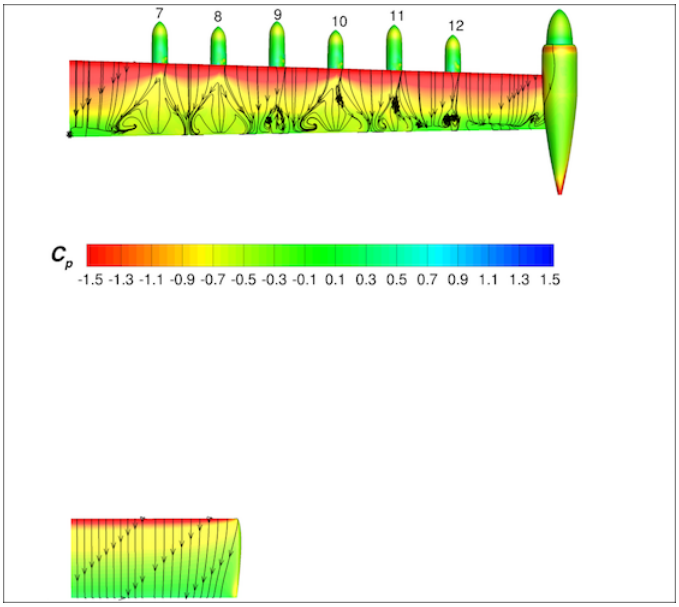

(a) **Surface pressure coefficient and streamlines**

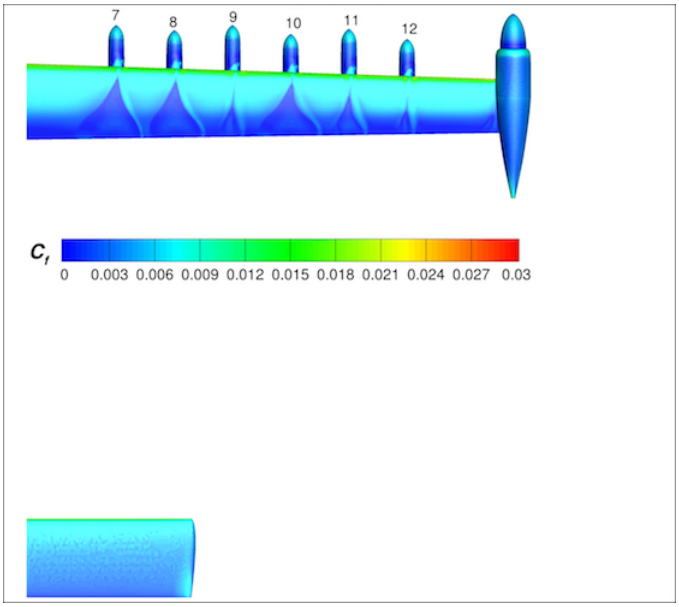

(b) **Skin friction coefficient**

Figure 12. USM3D SA solution for the unpowered cruise wing+stabilator configuration at α = 12°, 150 KTAS, *M* = 0.233, and *Re* = 2.83 million.

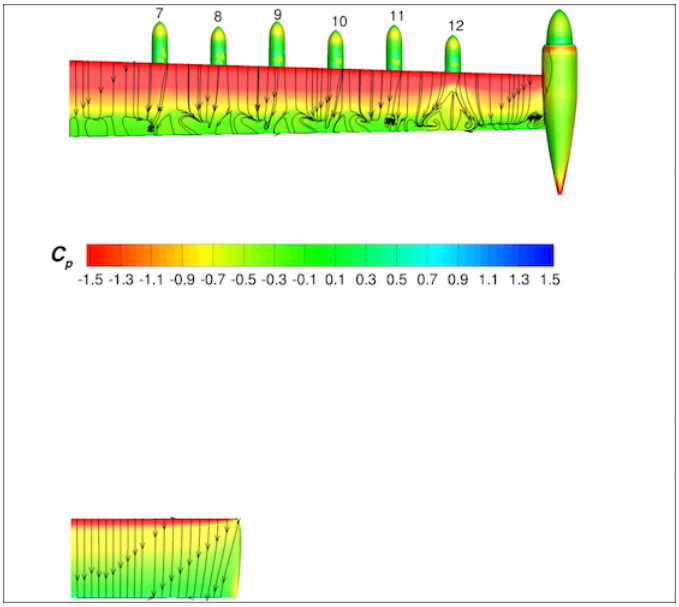

(a) **Pressure coefficient and streamlines**

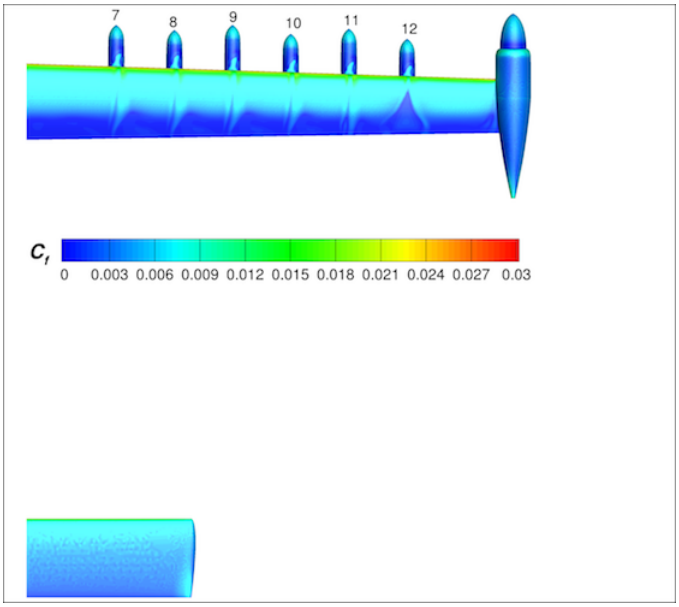

(b) **Skin friction coefficient**

Figure 13. USM3D SA solution for the unpowered cruise wing+stabilator configuration at α = 13°, 150 KTAS, *M* = 0.233, and *Re* = 2.83 million.

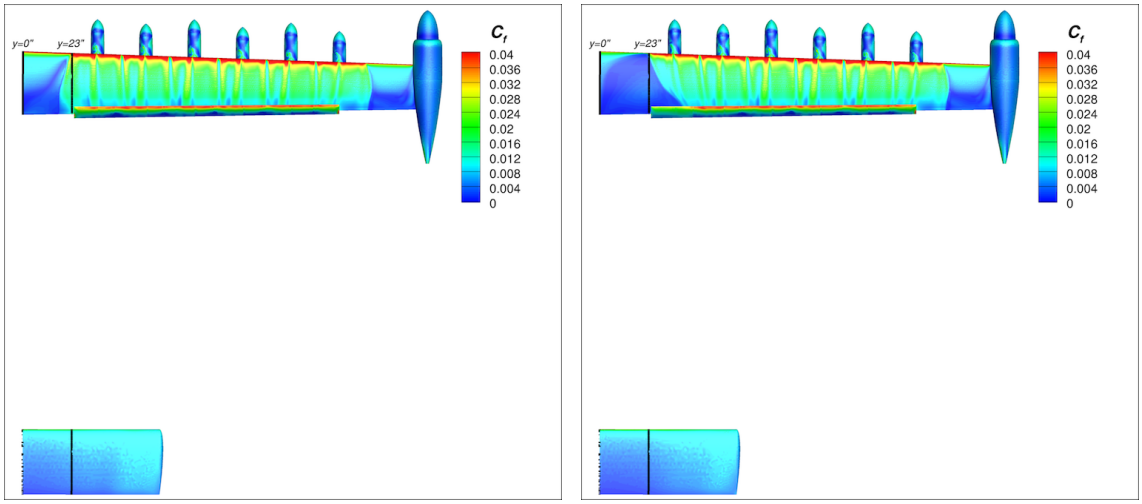

(a) USM3D SA, α = 13° (left) and α = 14° (right)

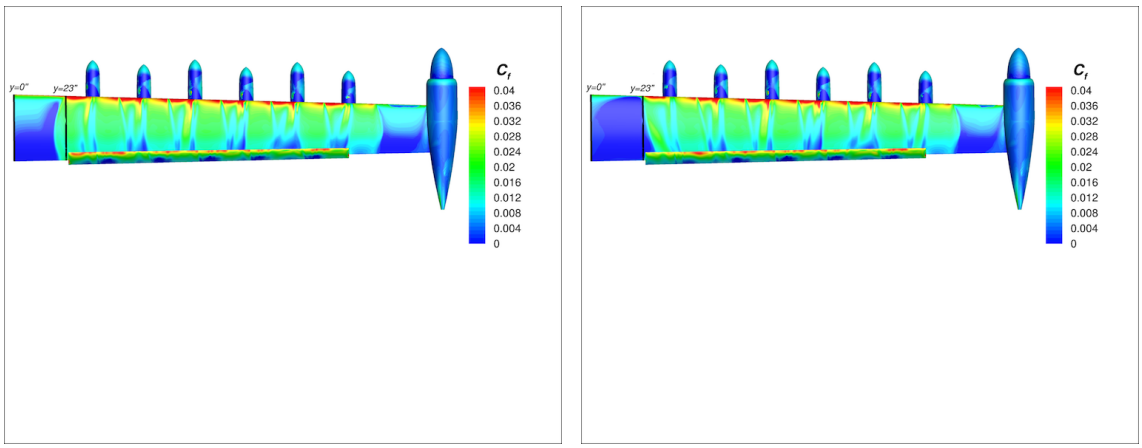

(b) FUN3D SA-RC-QCR, α = 12° (left) and α = 13° (right)

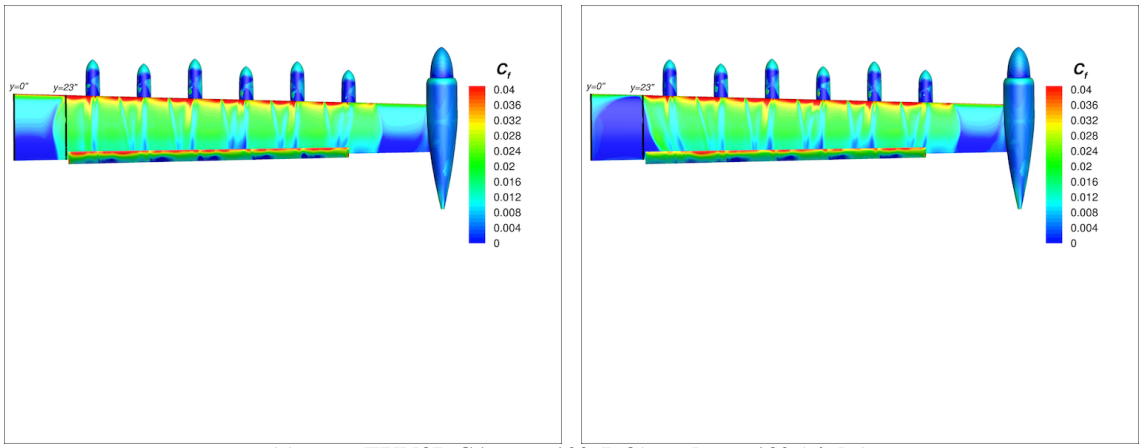

(c) FUN3D SA, α = 10° (left) and α = 12° (right)

Figure 14. FUN3D and USM3D code comparisons of skin friction coefficient for the high-lift wing with 30° flap deflection and high-lift blowing (13.7 hp/prop).

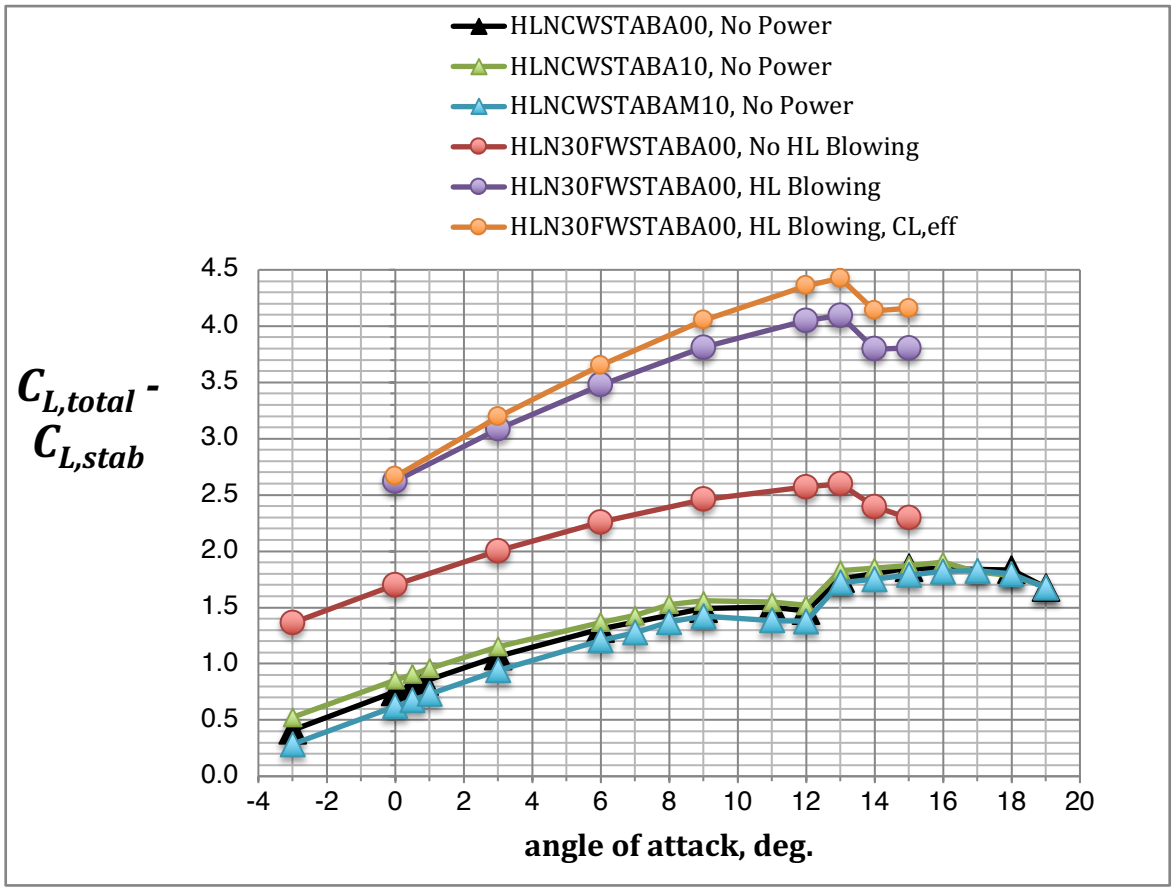

Figure 15. The comparison of lift coefficient, excluding the stabilator contribution to lift, for the wing+stabilator (stabilator incidence -1°, 0° trim tab) configurations. Unpowered cruise wing+stabilator at 150 KTAS, *Re* = 2.83 million, h = 8000 ft, and T = 30.5°F. High-lift wing with 30° flap deflection at 58 KTAS, *Re* = 1.33 million, h = 0 ft, T = 59°F, without and with HL blowing (13.7 hp/prop). USM3D SA.

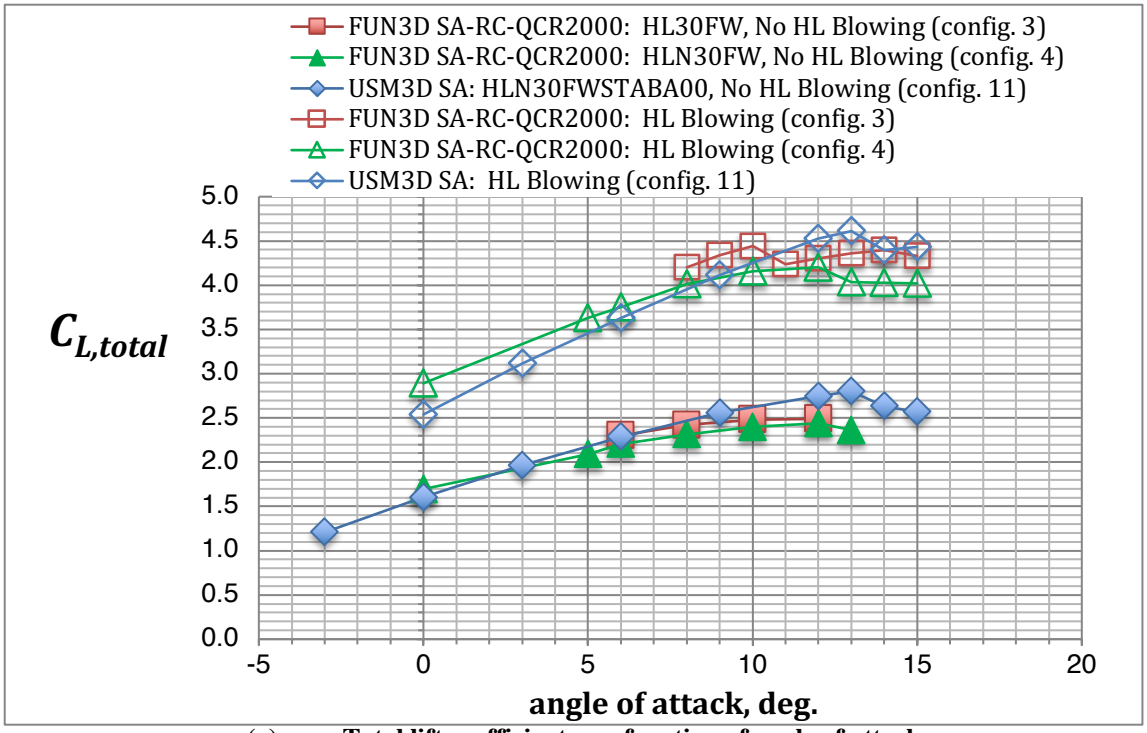

(a) Total lift coefficient as a function of angle of attack

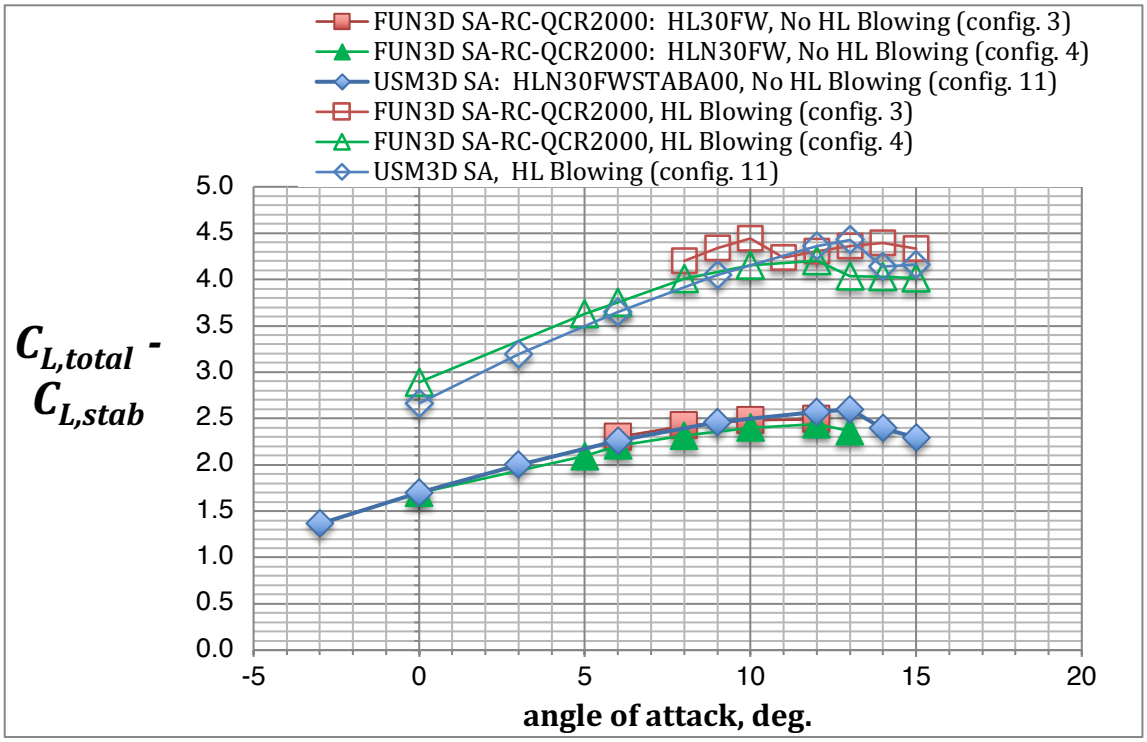

(b) Lift coefficient (without the stabilator contribution) as a function of angle of attack

Figure 16. The component buildup of lift, drag and pitching moment for the configurations with the high-lift with 30° flap deflection at 58 KTAS, *Re* = 1.33 million, h = 0 ft, and T = 59°F.

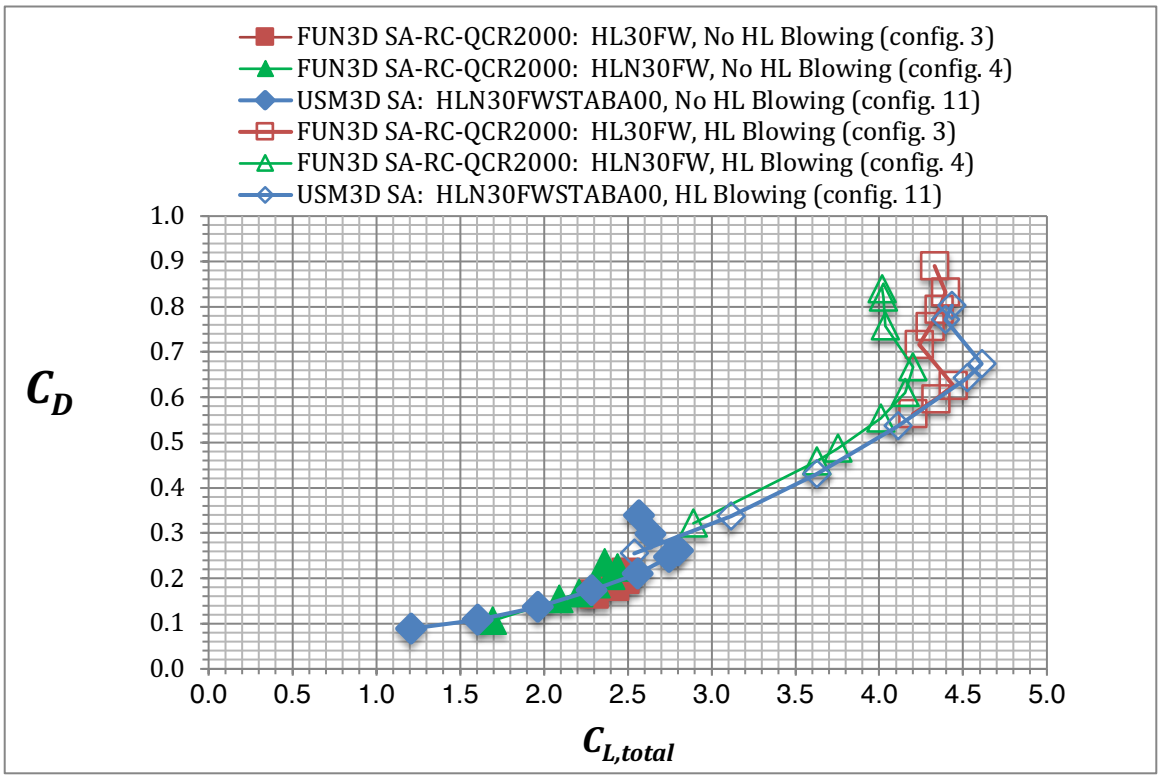

(c) Drag polar

Figure 16 Continued. The component buildup of lift, drag and pitching moment for the configurations with the high-lift with 30° flap deflection at 58 KTAS, *Re* = 1.33 million, h = 0 ft, and T = 59°F.

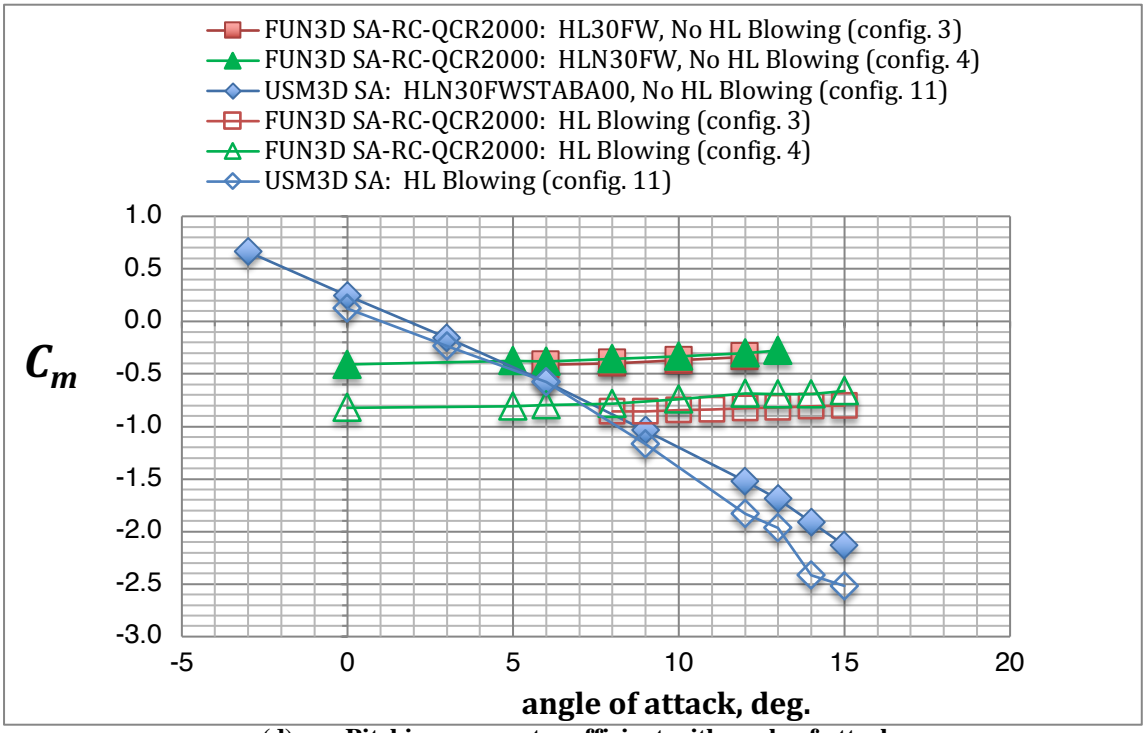

(d) Pitching moment coefficient with angle of attack

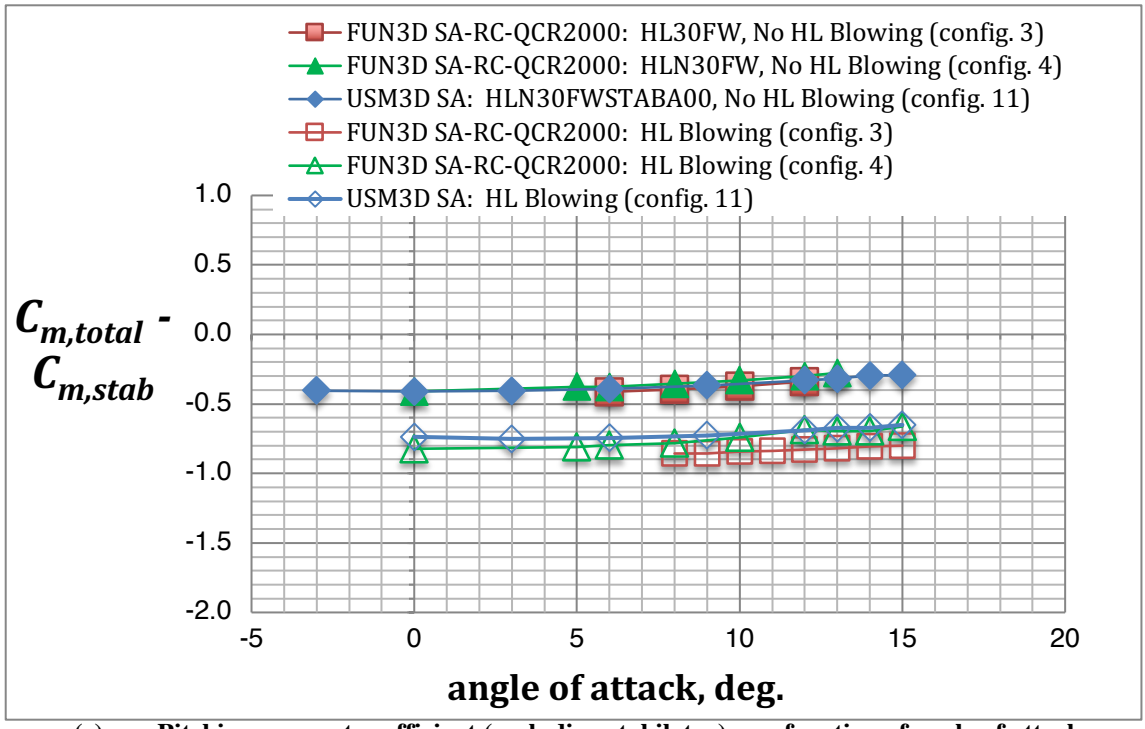

(e) Pitching moment coefficient (excluding stabilator) as a function of angle of attack

Figure 16 Continued. The component buildup of lift, drag and pitching moment for the configurations with the high-lift wing with 30° flap deflection at 58 KTAS, *Re* = 1.33 million, h = 0 ft, and T = 59°F.

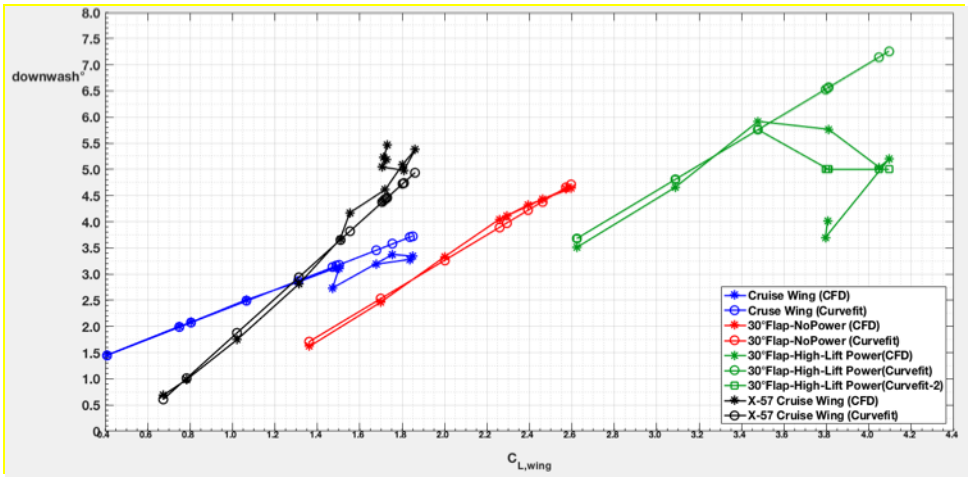

Figure 17(a). Computed and curve fit downwash angle as a function of aircraft C_L (excluding stabilator lift) for all configurations with the stab. Stabilator incidence is -1.0° and the trim tab angle is 0°.

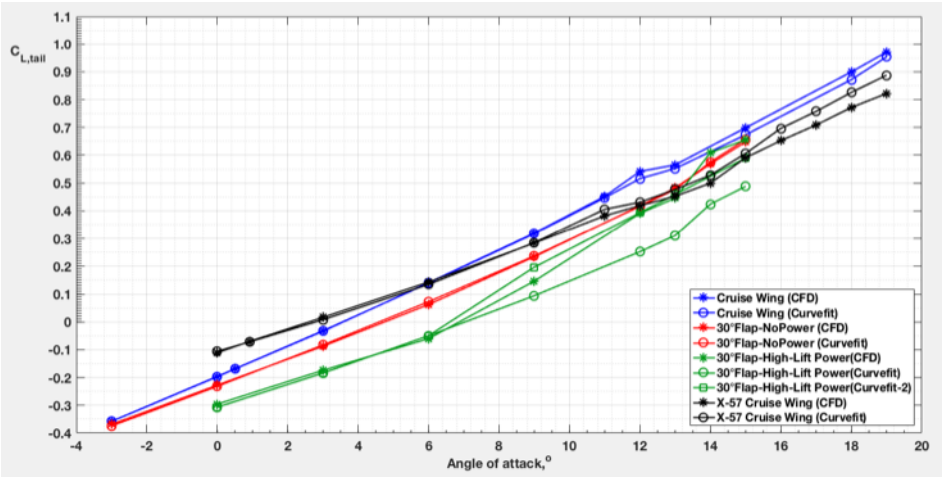

Figure 17(b). Computed and curve fit stabilator lift as a function of aircraft α for all configurations with the stab. Stabilator incidence is -1.0° and the trim tab angle is 0°.

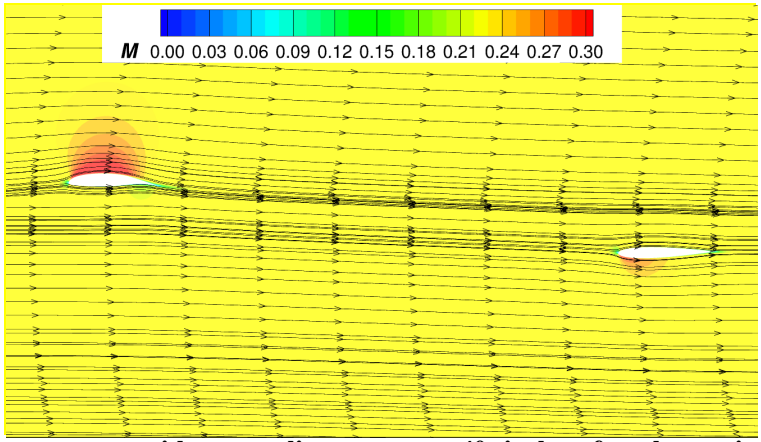

Figure 18. Mach contours with streamlines at y = 40 inches for the cruise wing+stabilator configuration (stabilator incidence -1.0°, 0° trim tab) at α = 0°, 150 KTAS, Re = 2.83 million, h = 8000 ft, and T = 30.5°F. USM3D SA.

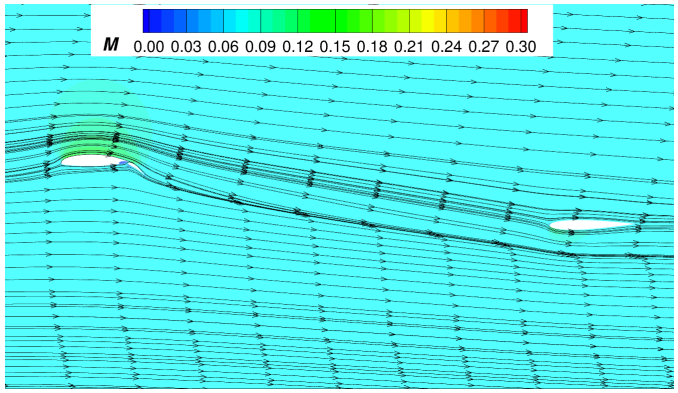

(a) $\alpha = 0°$

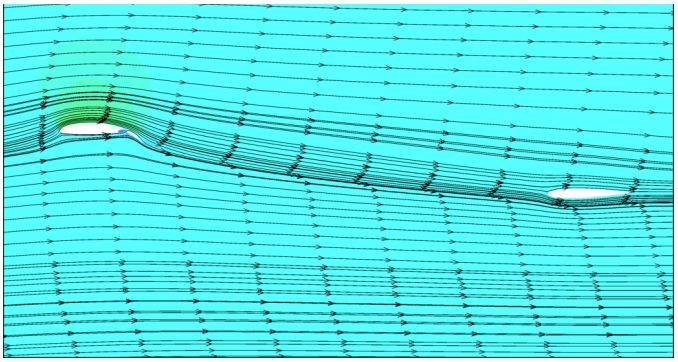

(b) $\alpha = 3°$

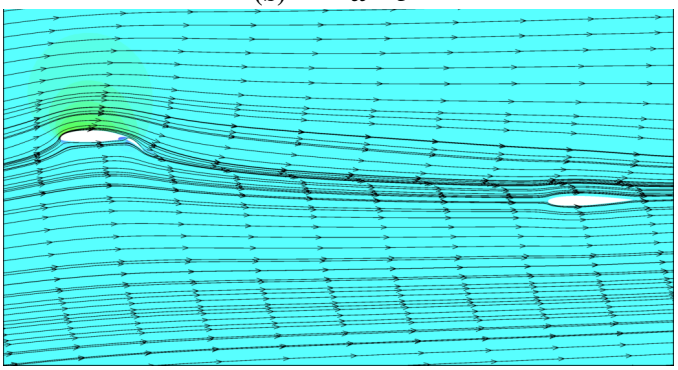

(c) $\alpha = 6°$

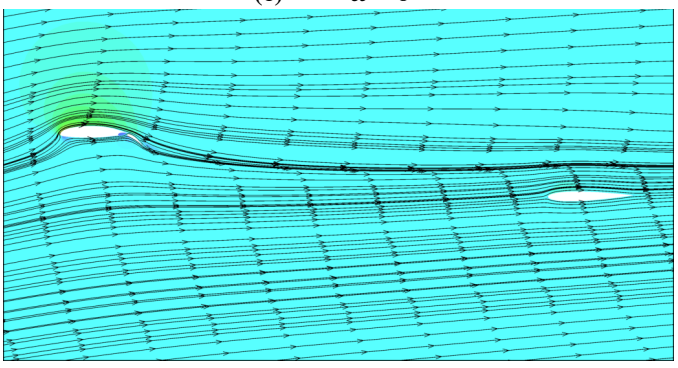

(d) $\alpha = 9°$

Figure 19. Mach contours with streamlines at y = 40 inches for the unblown wing with 30° flap deflection+stabilator configuration (stabilator incidence -1.0°, 0° trim tab) 58 KTAS, *Re* = 1.33 million, h = 0 ft, and T = 59°F. USM3D SA.

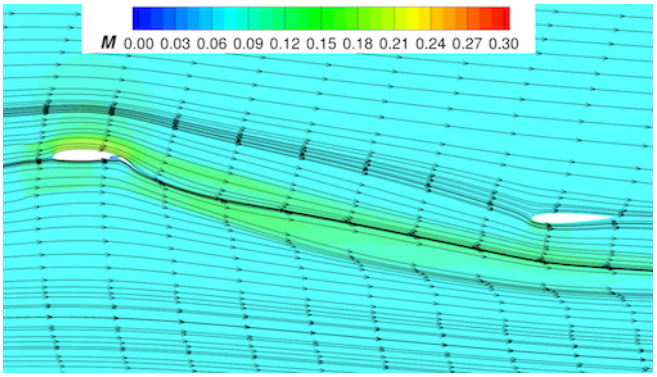

(a) α = 0°

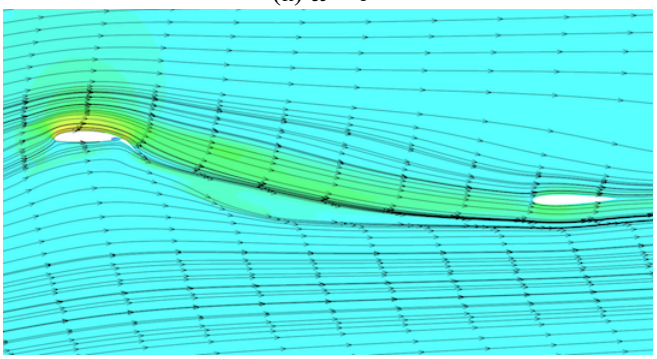

(b) α = 9°

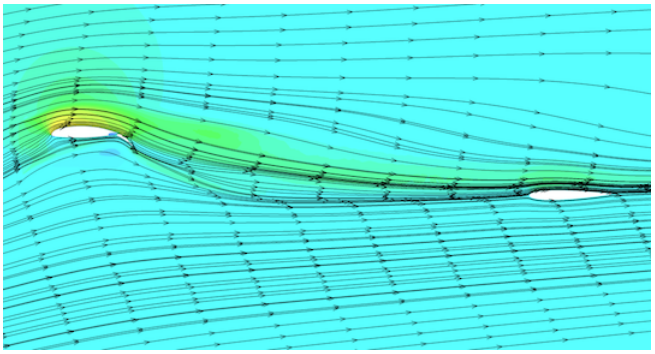

(c) α = 12°

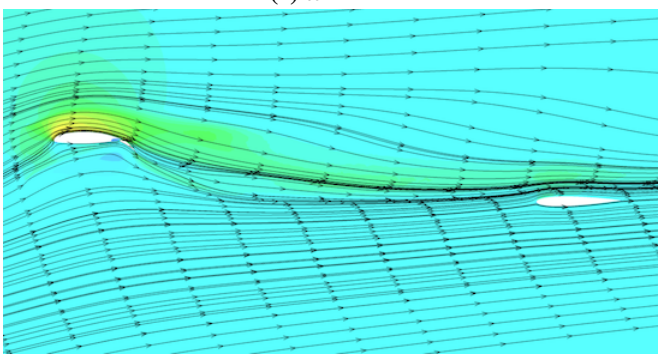

(d) α = 13°

Figure 20. Mach contours with streamlines at y = 40 inches for the blown wing with 30° flap deflection+stabilator configuration (stabilator incidence -1.0°, 0° trim tab) 58 KTAS, *Re* = 1.33 million, h = 0 ft, T = 59°F, and HL power 13.7 hp/prop. USM3D SA.

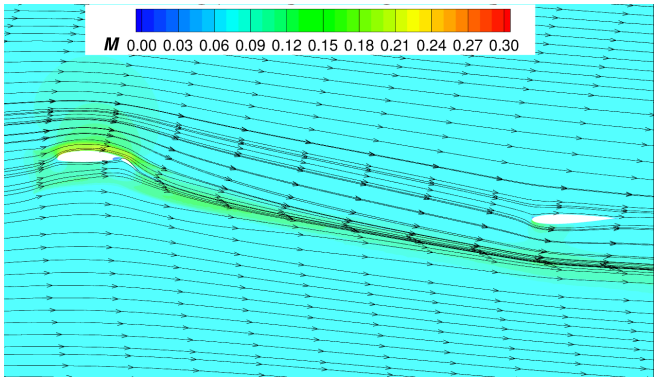

(a) α = 0°

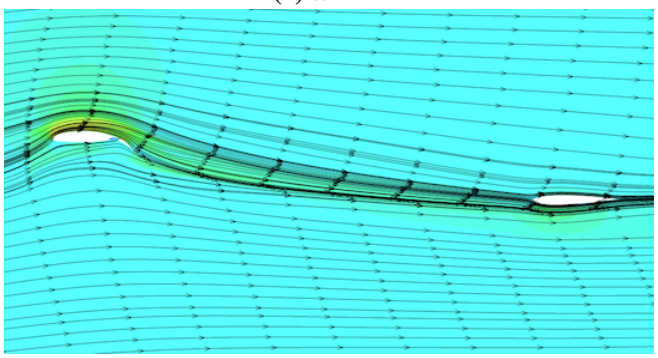

(b) α = 6°

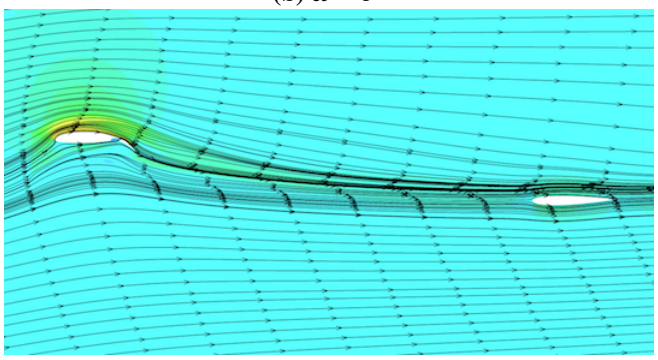

(c) α = 9°

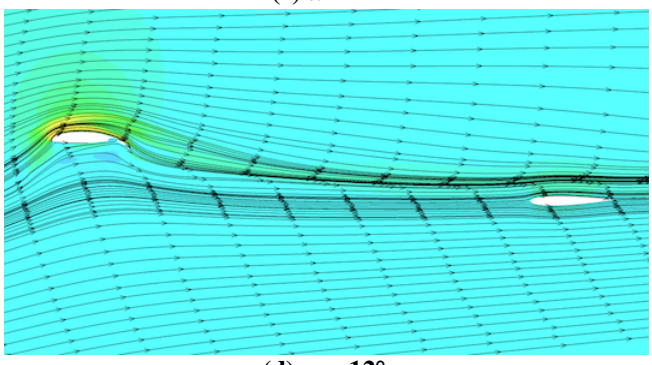

(d) α = 12°

Figure 21. Mach contours with streamlines at y = 50 inches for the blown wing with 30° flap deflection+stabilator configuration (stabilator incidence -1.0°, 0° trim tab) 58 KTAS, *Re* = 1.33 million, h = 0 ft, T = 59°F, and HL power 13.7 hp/prop. USM3D SA.

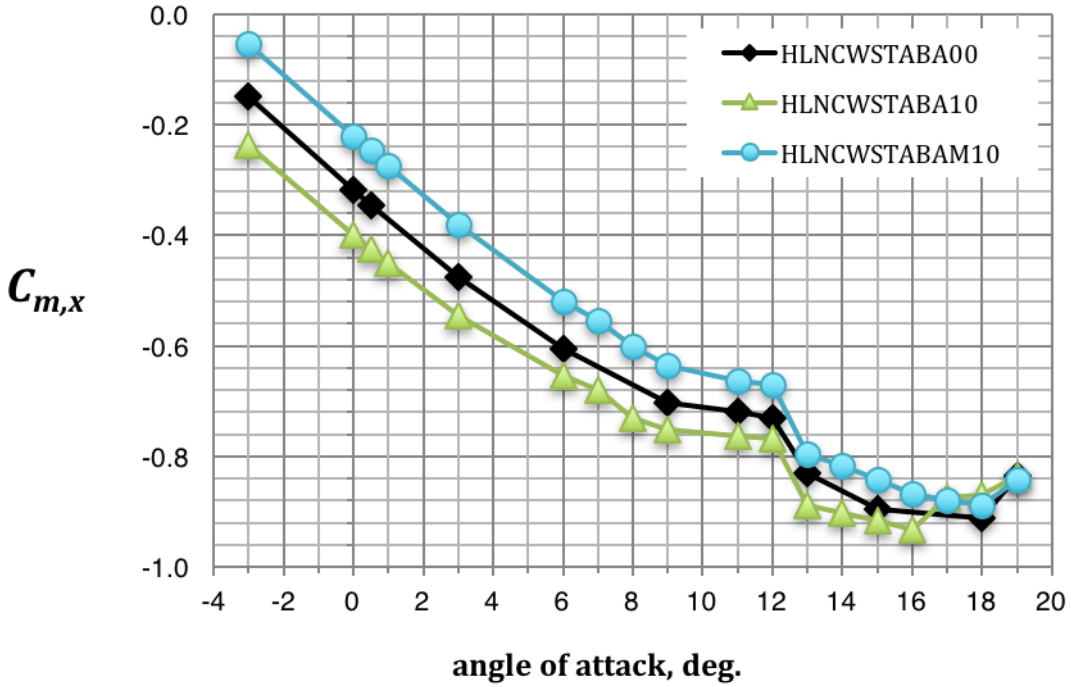

Figure 22. Effect of aileron deflection on rolling moment coefficient for the unpowered cruise wing+stabilator (stabilator incidence -1°, 0° trim tab) configuration, but excluding the stabilator contribution, at 150 KTAS, *Re* = 2.83 million, h = 8000 ft, and T = 30.5°F. USM3D SA.

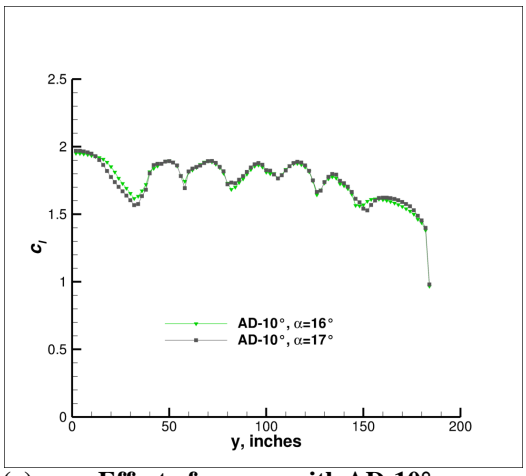

(a) Effect of α on c_l with AD-10°

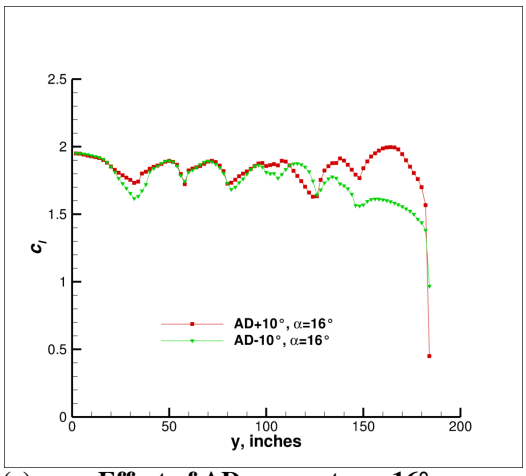

(c) Effect of AD on c_l at α = 16°

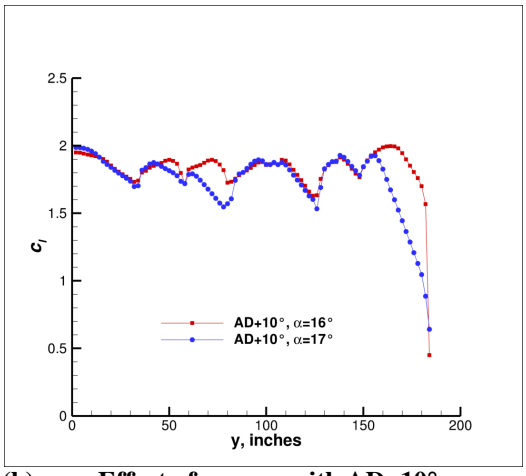

(b) Effect of α on c_l with AD+10°

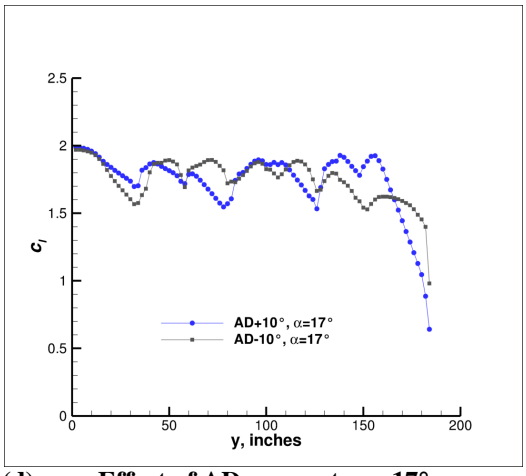

(d) Effect of AD on c_l at α = 17°

Figure 23. The sectional lift coefficient of the cruise wing (stabilator -1°, 0° trim tab) with AD+10° and AD-10°, at α = 16° and α = 17°, 150 KTAS, *Re* = 2.83 million, h = 8000 ft, and T = 30.5°F. USM3D SA.

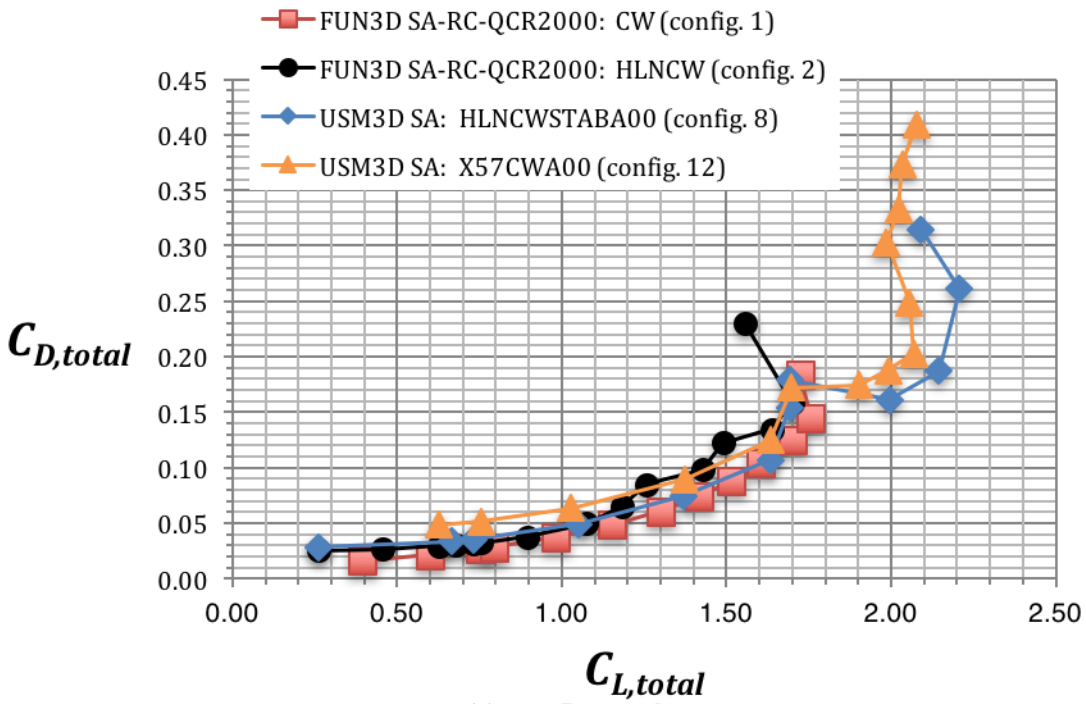

(a) Drag polar

Figure 24. The component buildup of lift, drag and pitching moment for the unpowered cruise wing configurations at 150 KTAS, *Re* = 2.83 million, h = 8000 ft, and T = 30.5°F.

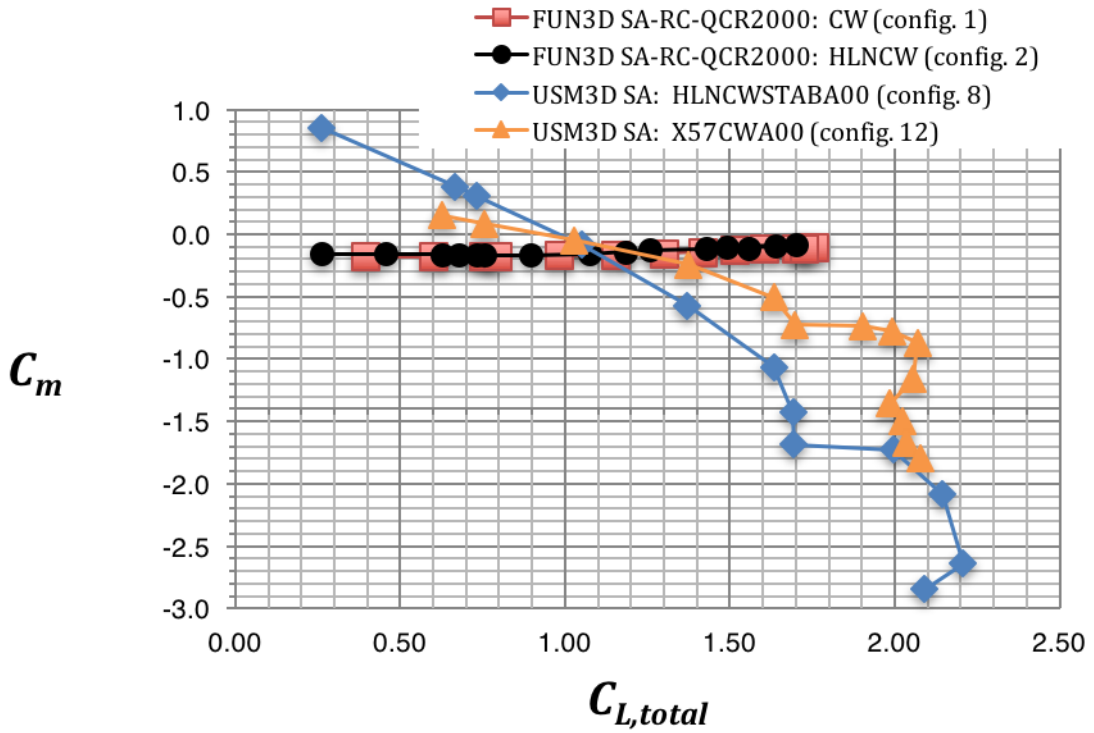

(b) Pitching moment coefficient as a function of lift coefficient

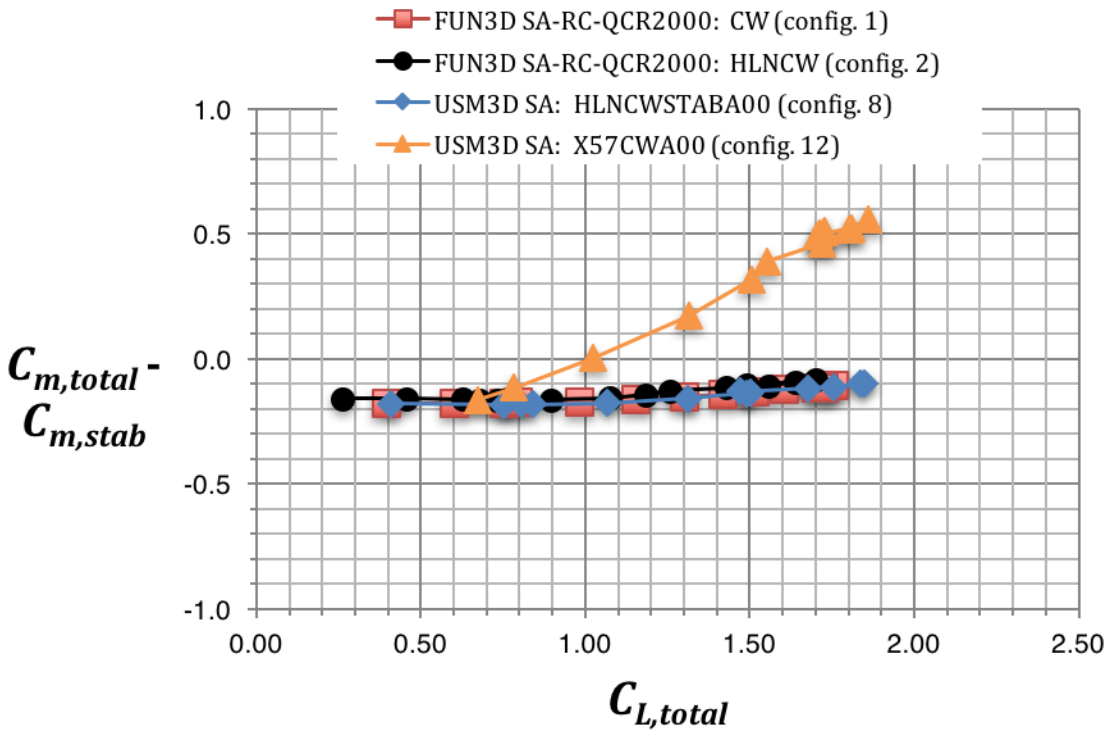

(c) Pitching moment coefficient (excluding stabilator) as a function of lift coefficient

Figure 24 Continued. The component buildup of lift, drag and pitching moment for the unpowered cruise wing configurations at 150 KTAS, *Re* = 2.83 million, h = 8000 ft, and T = 30.5°F.

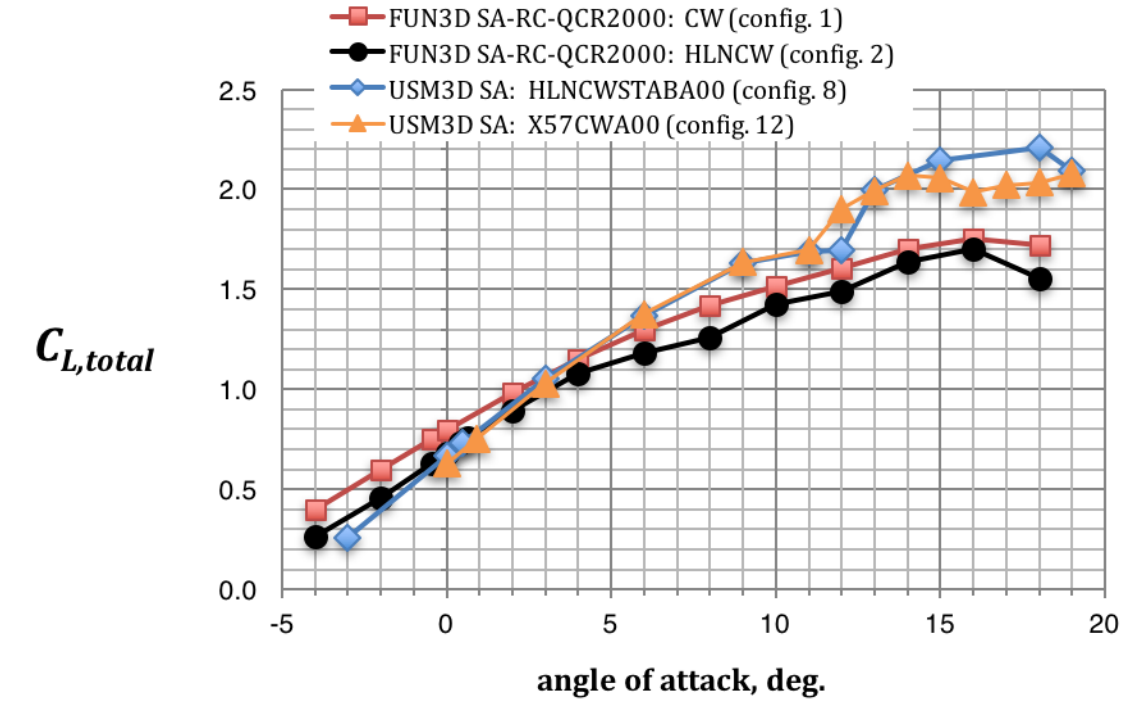

(d) Total lift coefficient as a function of angle of attack

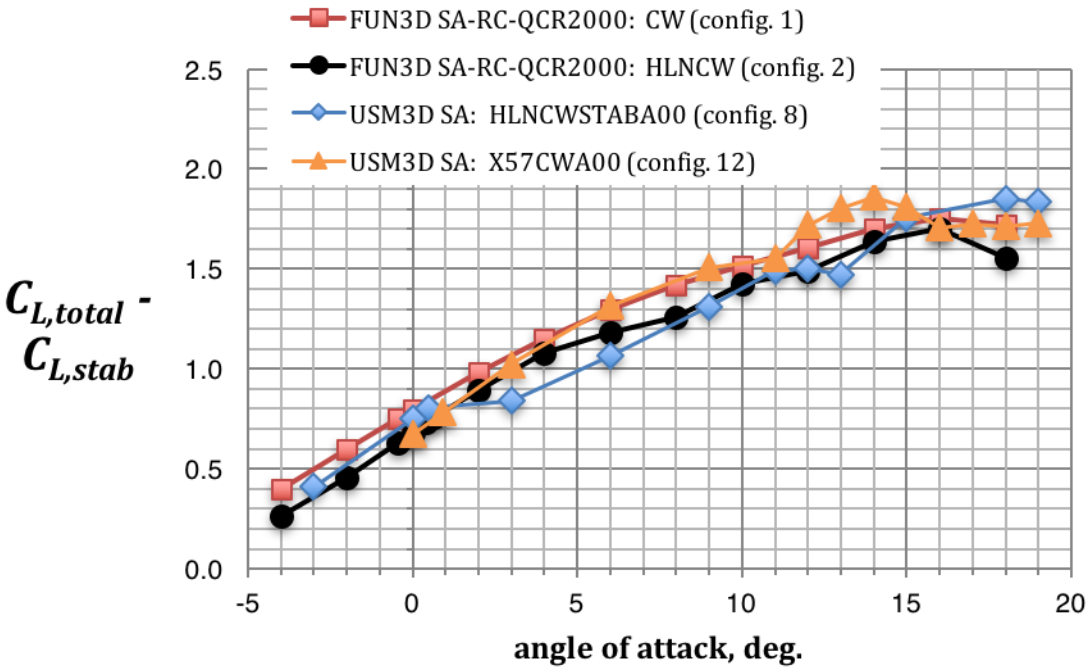

(e) Lift coefficient excluding the stabilator (if present), as a function of angle of attack

Figure 24 Continued. The component buildup of lift, drag and pitching moment for the unpowered cruise wing configurations at 150 KTAS, *Re* = 2.83 million, h = 8000 ft, and T = 30.5°F.

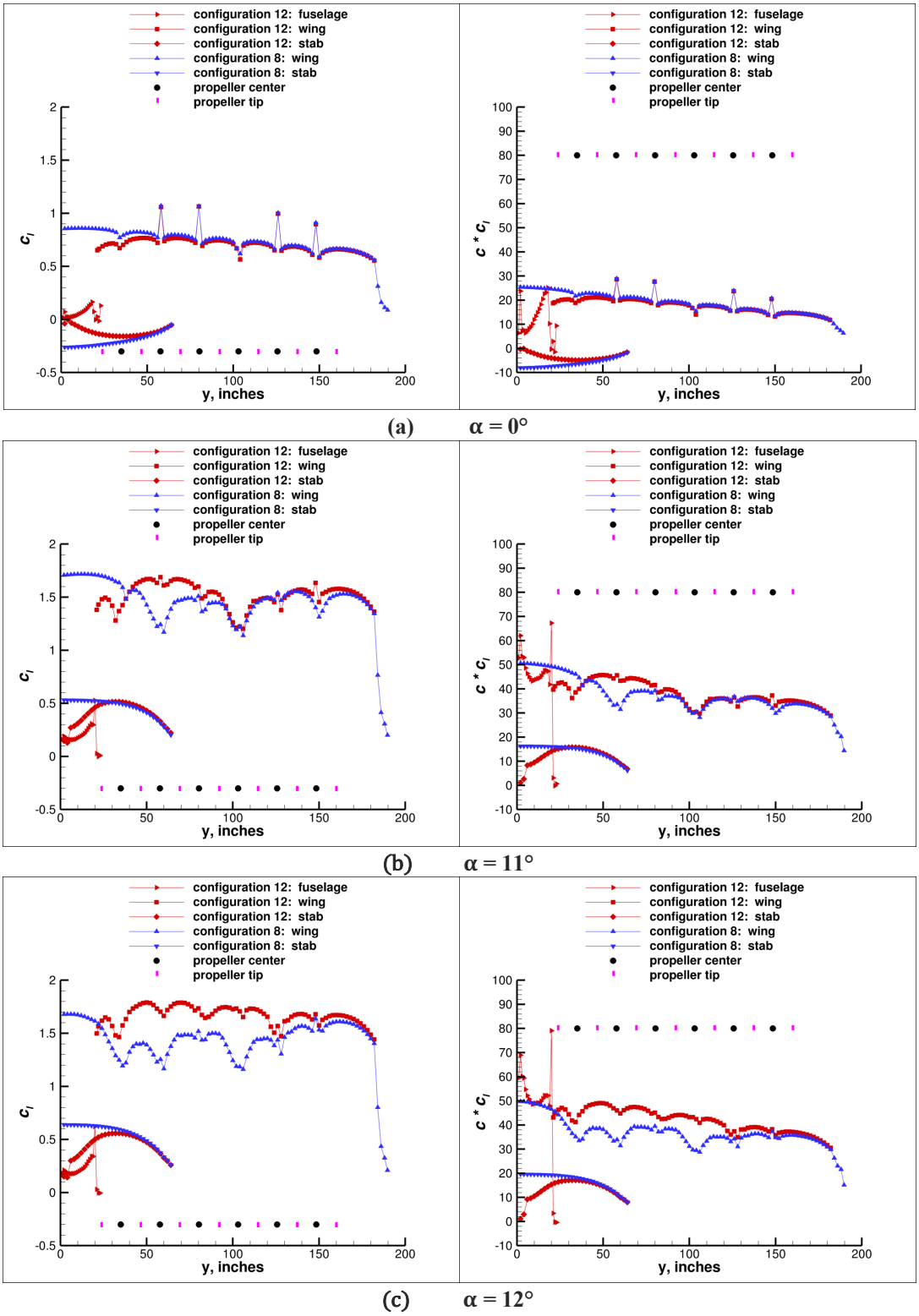

Figure 25. The comparisons of spanloading between the cruise wing configurations, with the fuselage/vtail (config. 12) and without the fuselage/vtail (config. 8), at 150 KTAS, *Re* = 2.83 million, h = 8000 ft, and T = 30.5°F. USM3D SA.

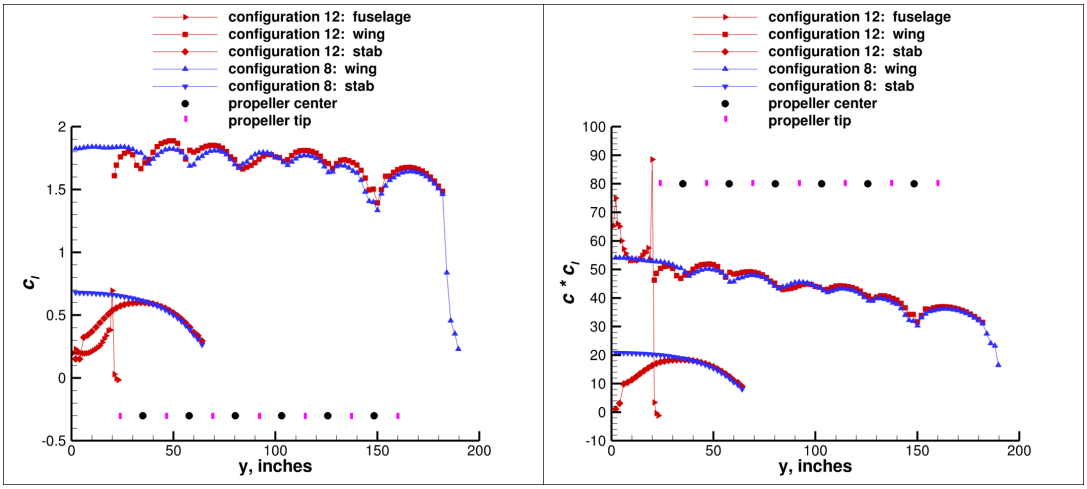

(d) $\alpha = 13°$

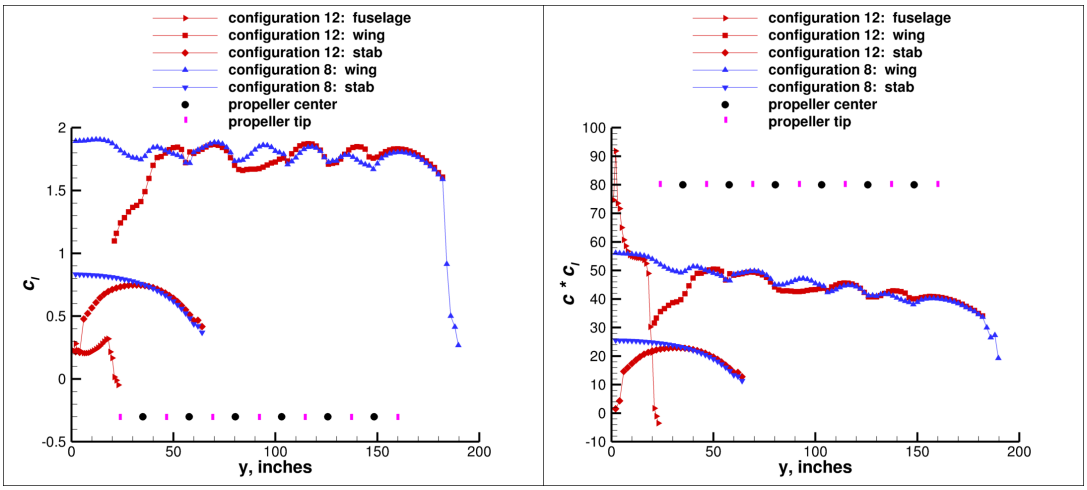

(e) $\alpha = 15°$

Figure 25 Continued. The comparisons of spanloading between the cruise wing configurations, with the fuselage/vtail (config. 12) and without the fuselage/vtail (config. 8), at 150 KTAS, *Re* = 2.83 million, h = 8000 ft, and T = 30.5°F. USM3D SA.

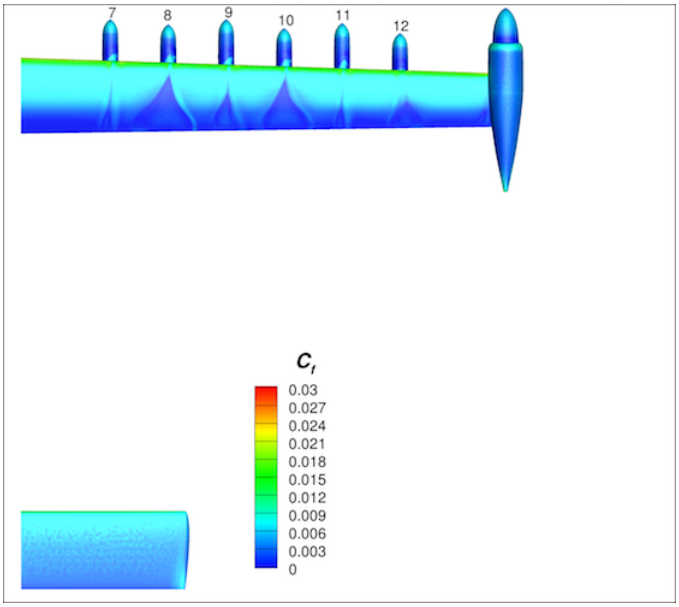

(a) Cruise wing+stabilator configuration 8

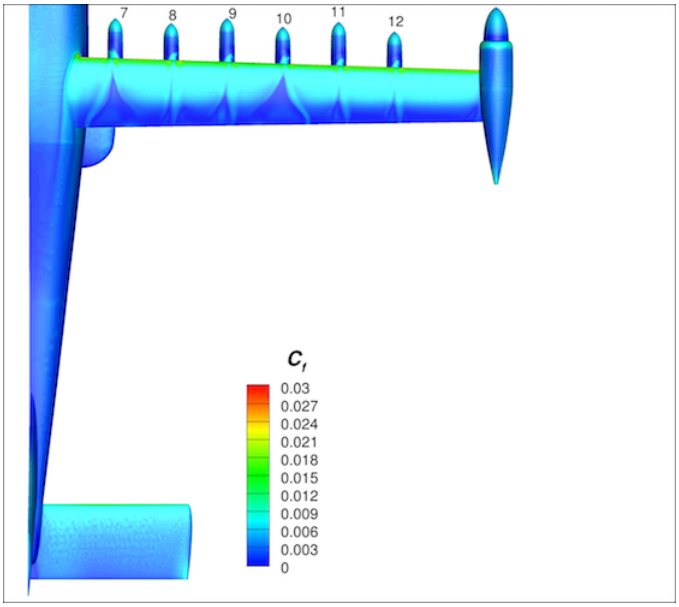

(b) Full geometry, cruise wing configuration 12

Figure 26. Skin friction contours on the surface for configurations 8 and 12 at α = 11°, 150 KTAS, *Re* = 2.83 million, h = 8000 ft, and T = 30.5°F.

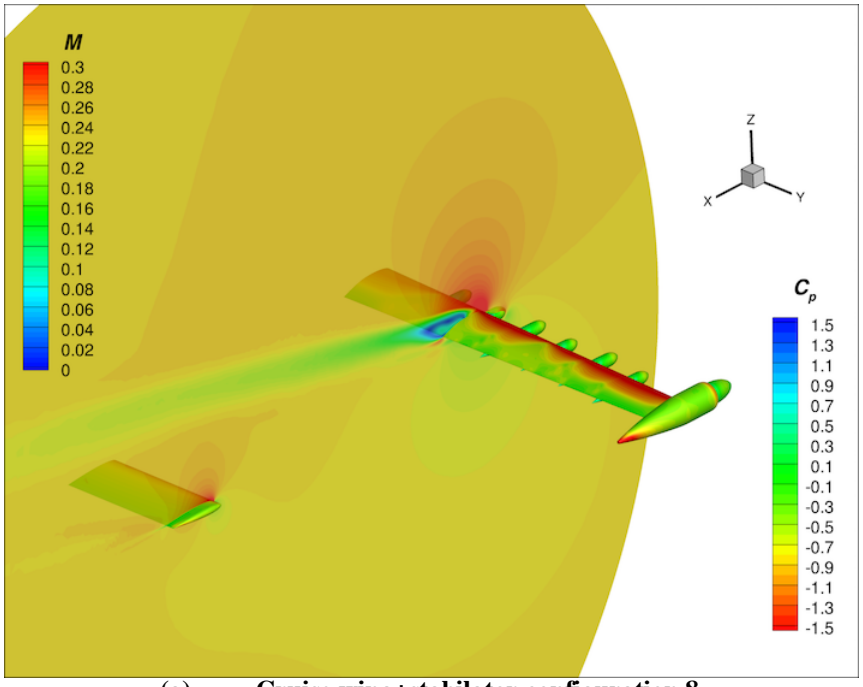

(a) Cruise wing+stabilator configuration 8

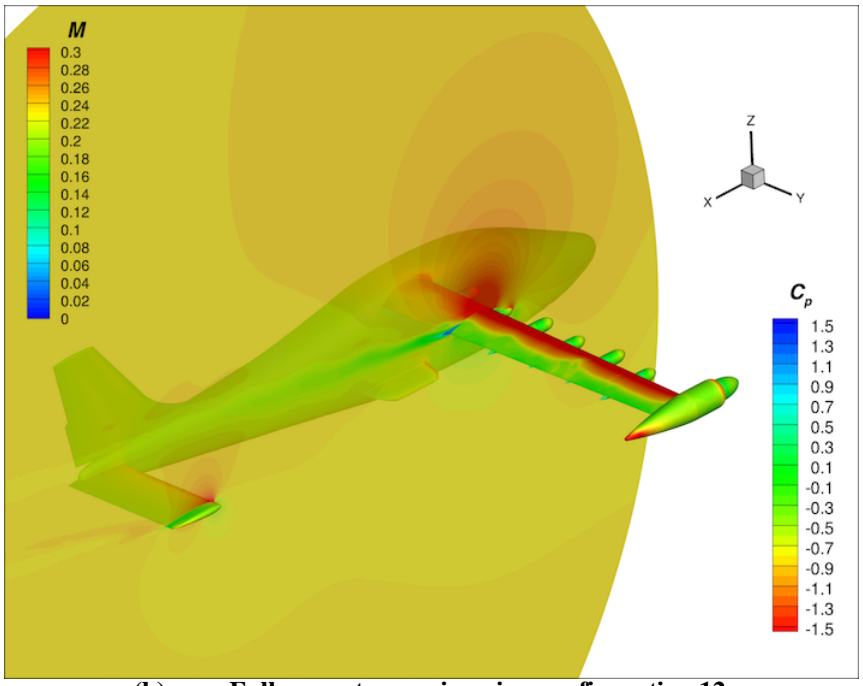

(b) Full geometry, cruise wing configuration 12

Figure 27. Mach contours at a plane y = 60 inches and surface pressure coefficient contours for configurations 8 and 12 at α = 12°, 150 KTAS, *Re* = 2.83 million, h = 8000 ft, and T = 30.5°F.

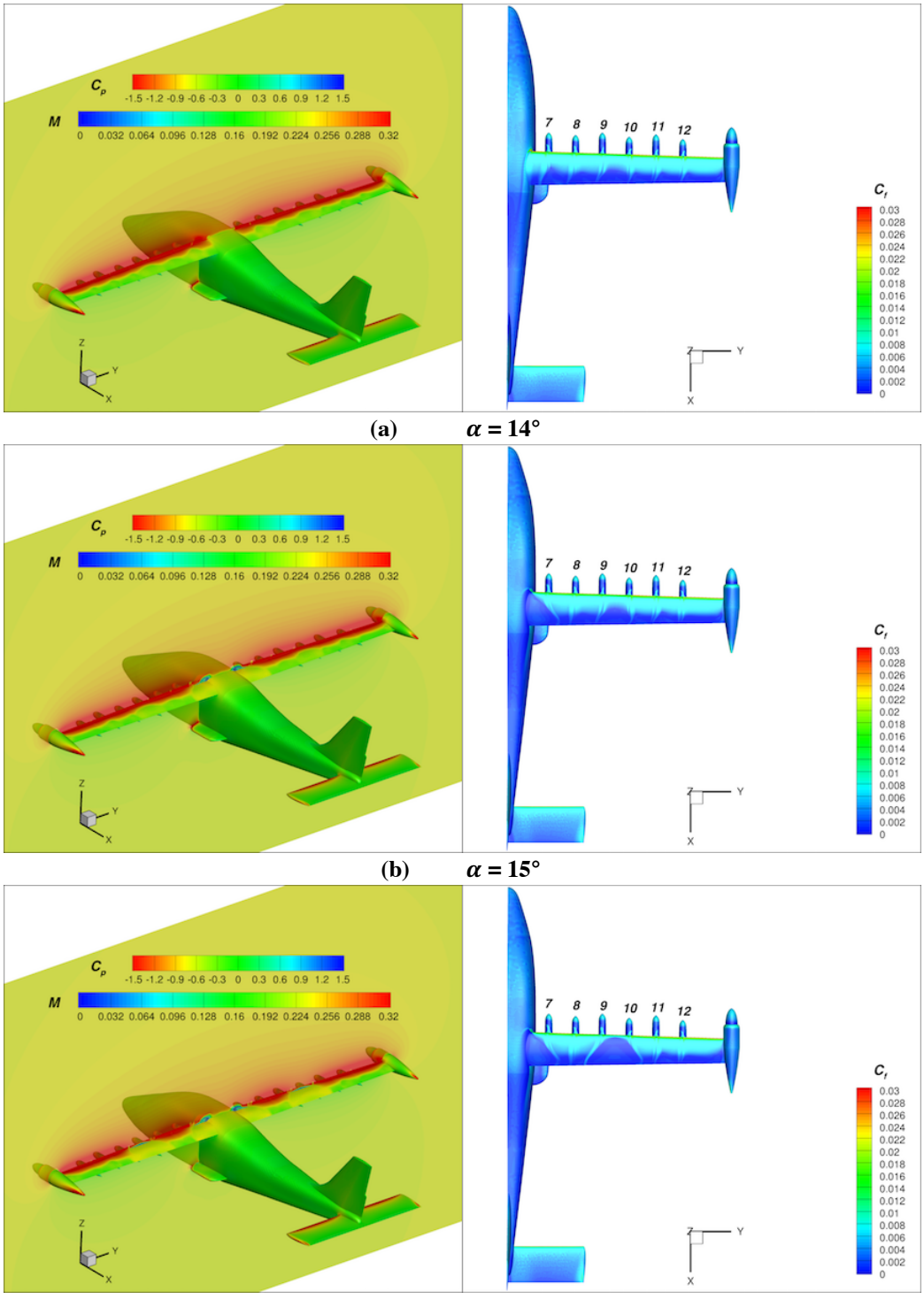

(a) $\alpha = 14°$

(b) $\alpha = 15°$

(c) $\alpha = 16°$

Figure 28. Mach contours at a plane x = 155 inches and surface pressure coefficient contours (left), and surface skin friction coefficient contours (right) for the full geometry, configuration 12 (cruise wing, stabilator incidence -1° and 0° trim tab) for 150 KTAS, *Re* = 2.83 million, h = 8000 ft, and T = 30.5°F.

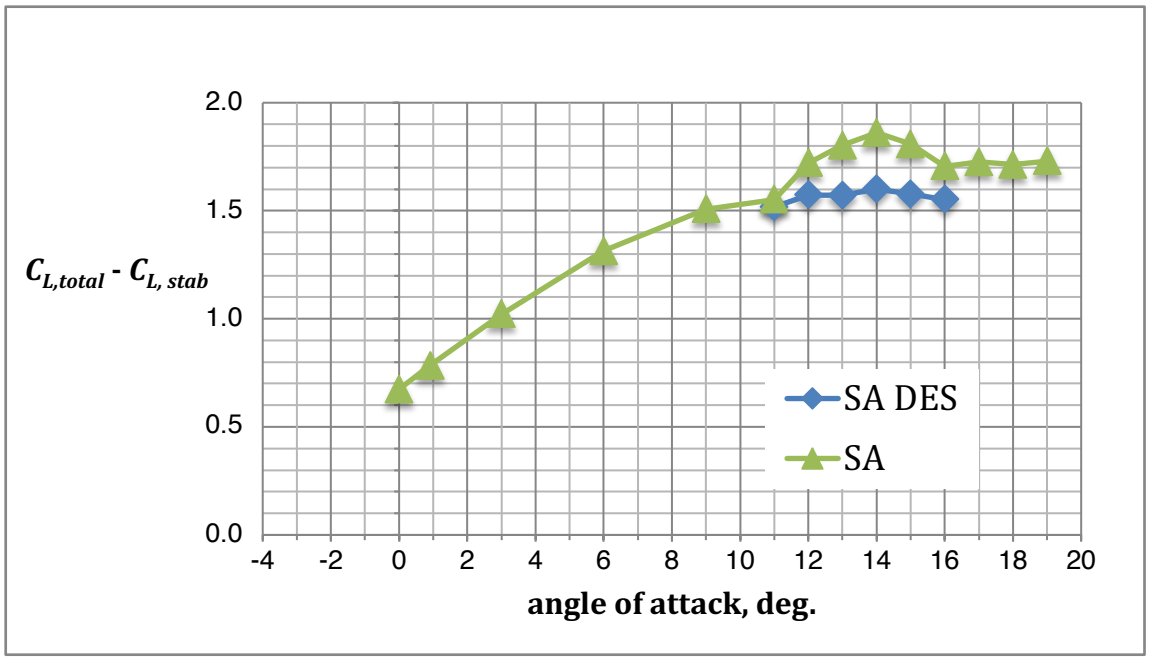

(a) lift coefficient, excluding the stabilator contribution

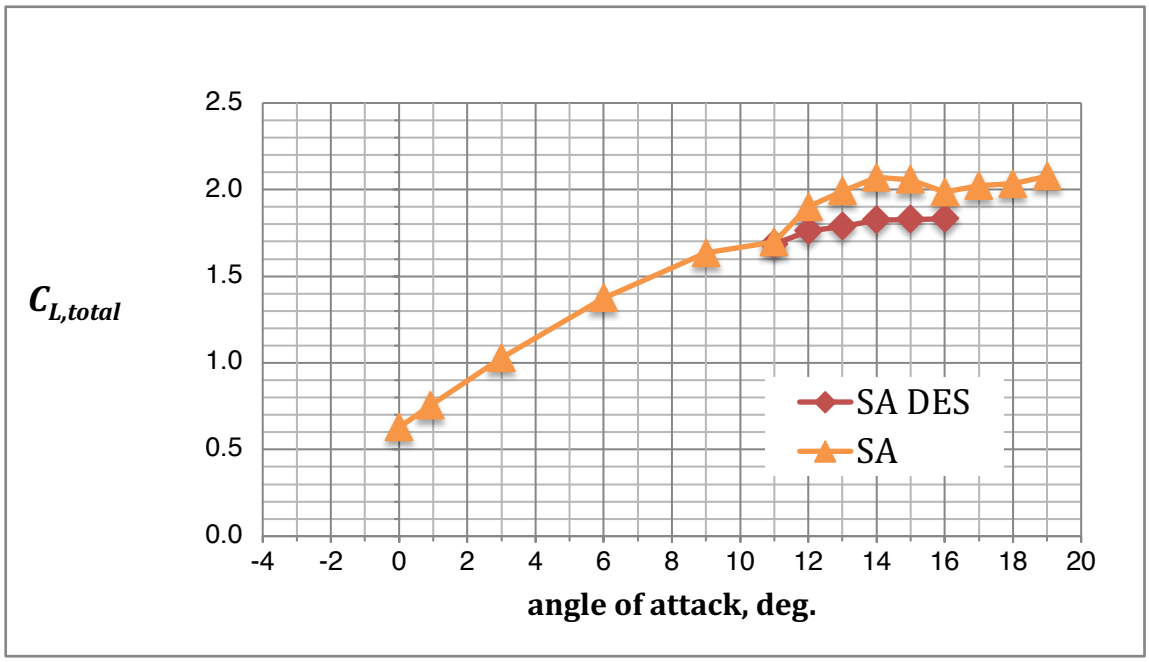

(b) total lift coefficient

Figure 29. The effect of turbulence model on lift coefficient for USM3D solutions of the full geometry, configuration 12 (cruise wing, stabilator incidence -1° and 0° trim tab) for 150 KTAS, *Re* = 2.83 million, h = 8000 ft, and T = 30.5°F.

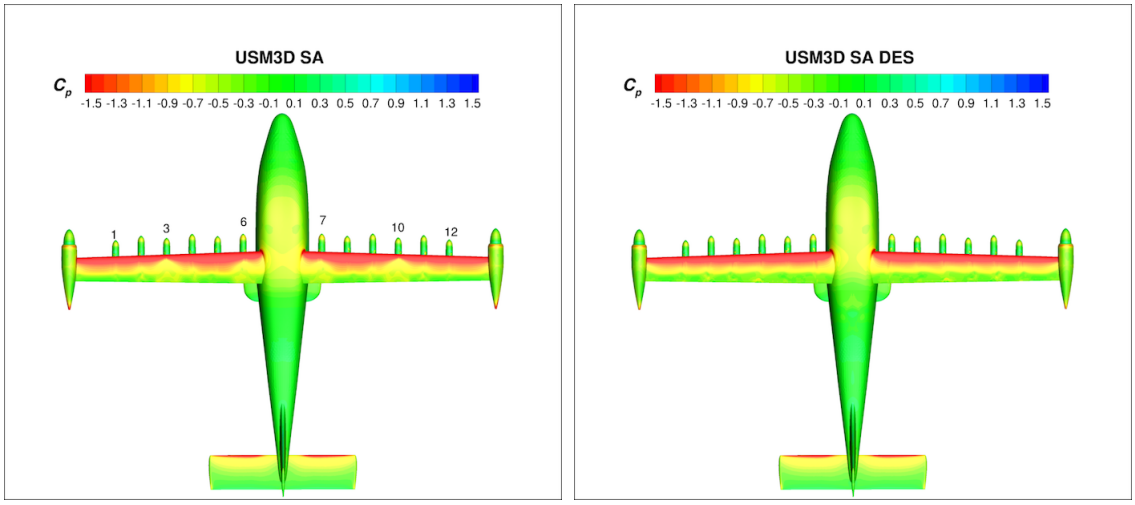

Figure 30. The effect of turbulence model on surface pressure coefficient for USM3D solutions of the full geometry, configuration 12 (cruise wing, stabilator incidence -1° and 0° trim tab) at α = 11°, 150 KTAS, *Re* = 2.83 million, h = 8000 ft, and T = 30.5°F.

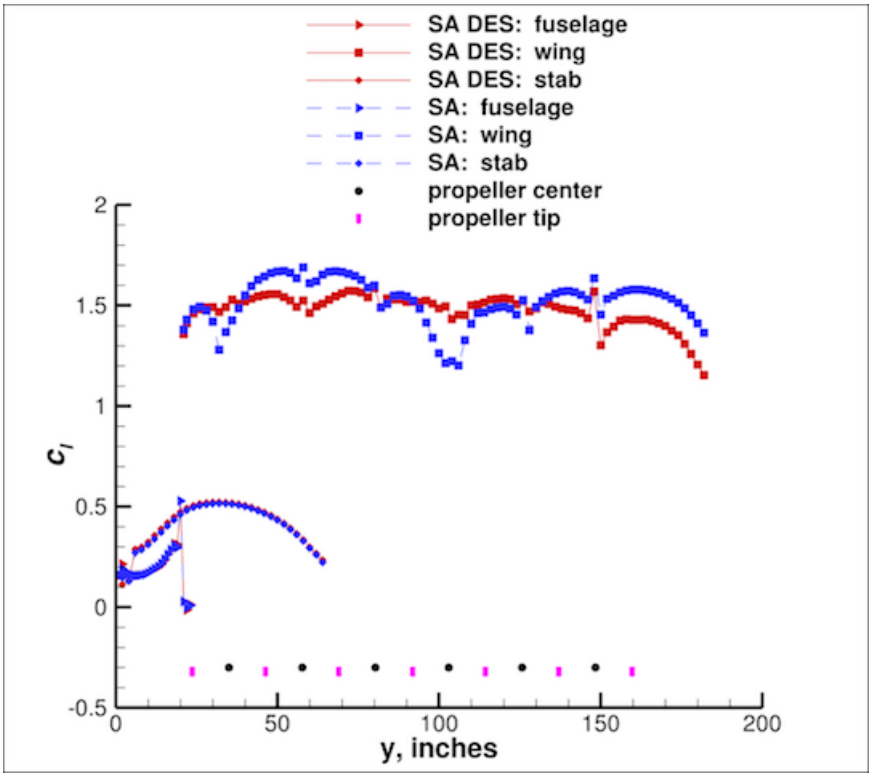

Figure 31. The effect of turbulence model on sectional lift coefficient for USM3D solutions of the full geometry, configuration 12 (cruise wing, stabilator incidence -1° and 0° trim tab) at α = 11°, 150 KTAS, *Re* = 2.83 million, h = 8000 ft, and T = 30.5°F.

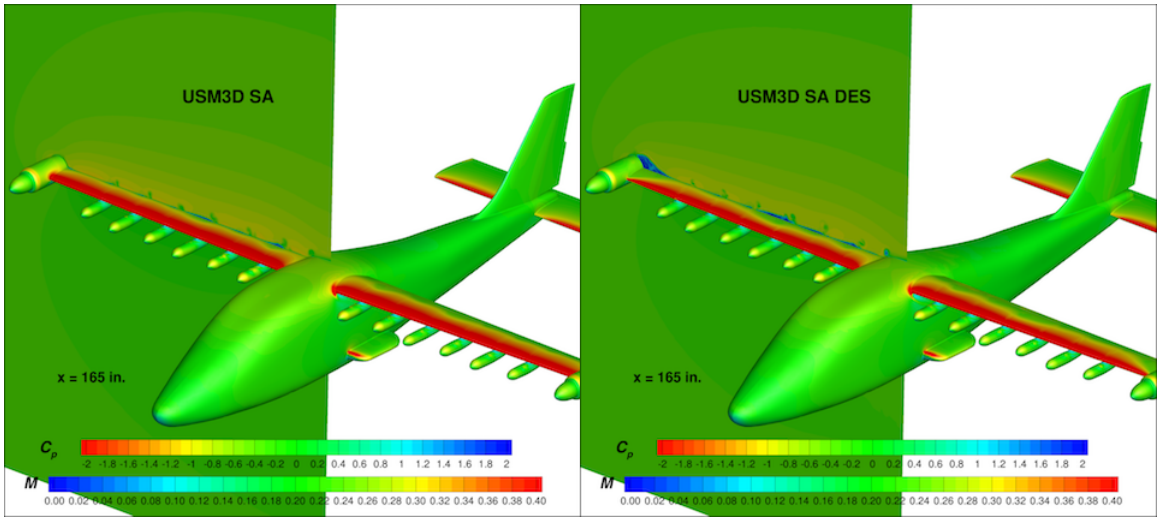

Figure 32. The effect of turbulence model on surface pressure coefficient contours and Mach contours at x = 165 in. for USM3D solutions of the full geometry, configuration 12 (cruise wing, stabilator incidence -1° and 0° trim tab) at α=14°, 150 KTAS, *Re* = 2.83 million, h = 8000 ft, and T = 30.5°F.

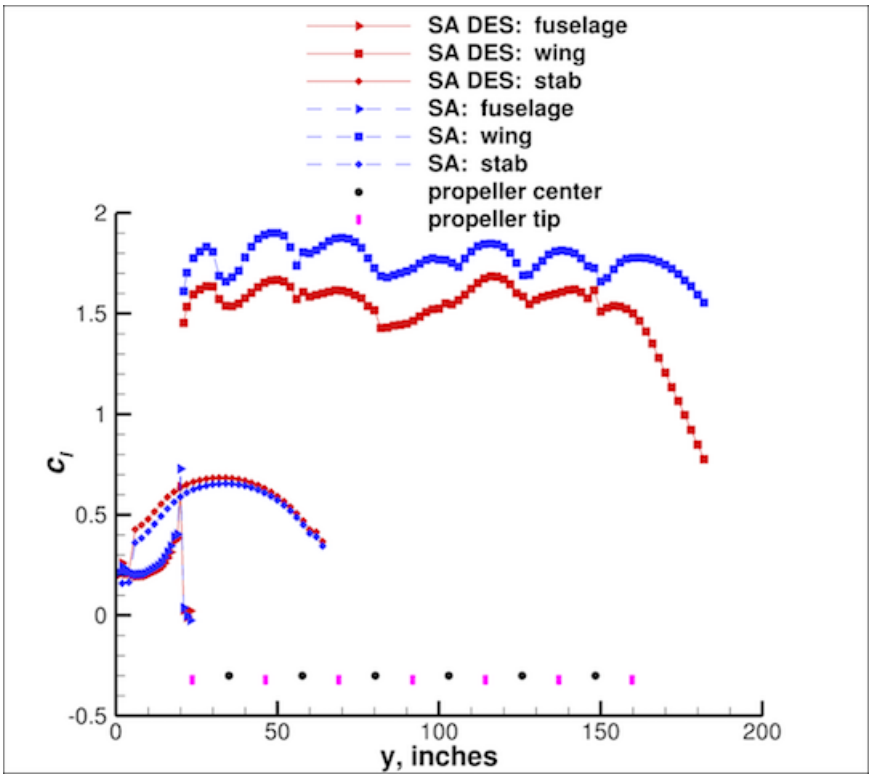

Figure 33. The effect of turbulence model on sectional lift coefficient for USM3D solutions of the full geometry, configuration 12 (cruise wing, stabilator incidence -1° and 0° trim tab) at α = 14°, 150 KTAS, *Re* = 2.83 million, h = 8000 ft, and T = 30.5°F.

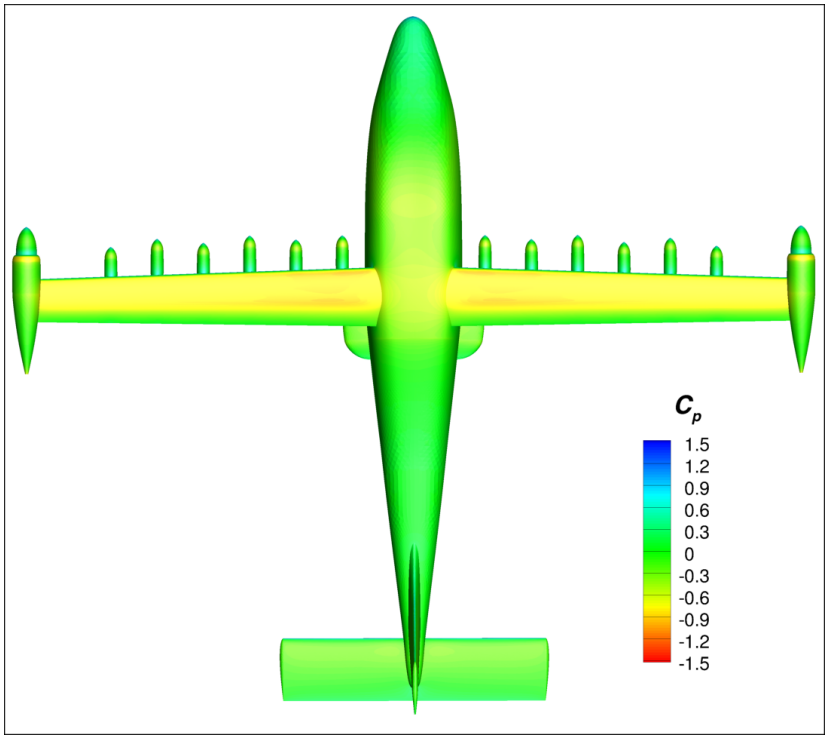

(a) USM3D SA turbulence model

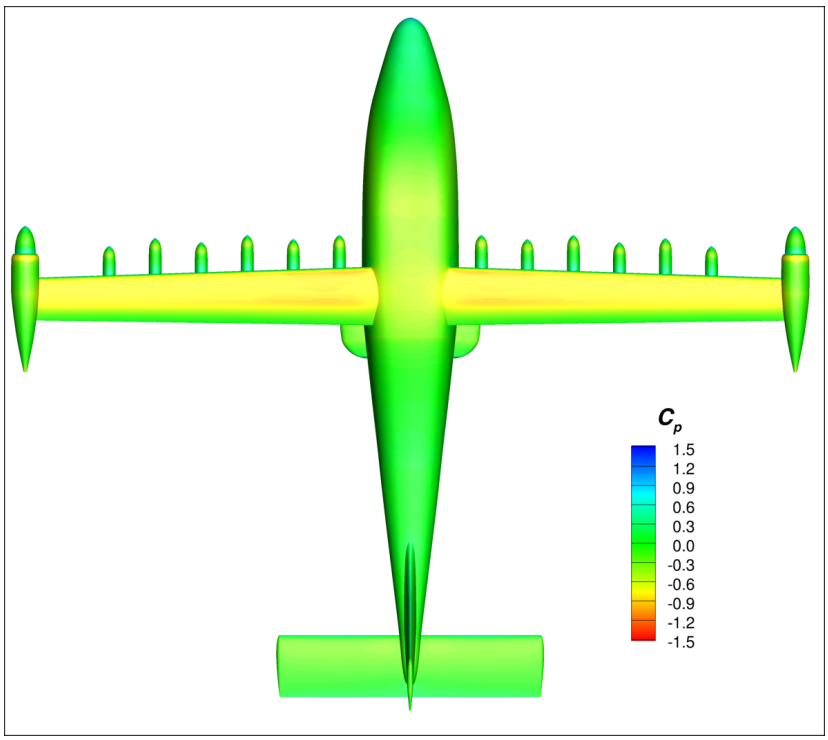

(b) KESTREL SA turbulence model

Figure 34. Code comparison of pressure coefficient contours for the full geometry, configuration 12 (cruise wing, stabilator incidence -1° and 0° trim tab) at α = 0°, 150 KTAS, *Re* = 2.83 million, h = 8000 ft, and T = 30.5°F.

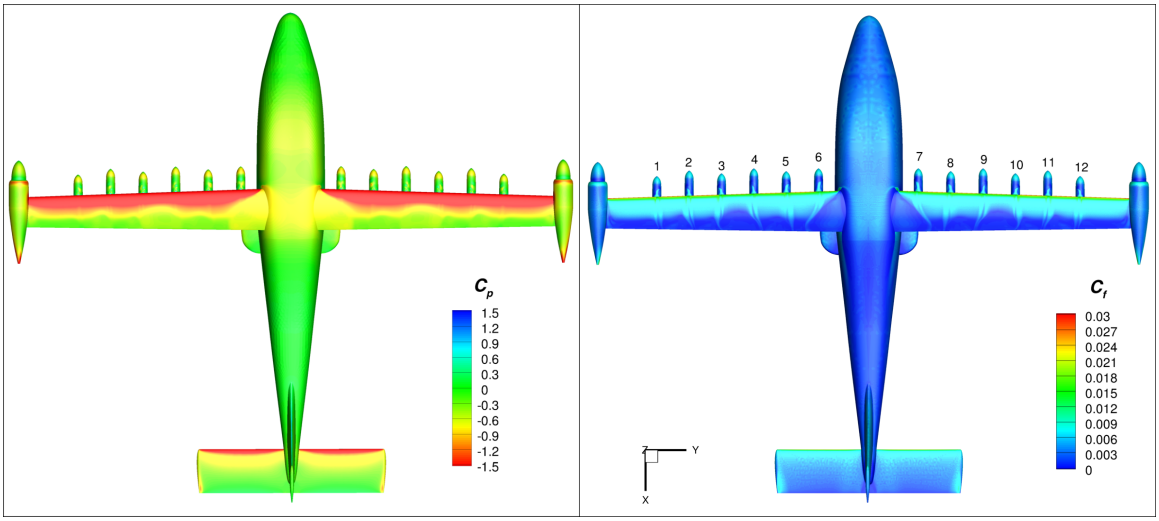

(a) USM3D SA turbulence model

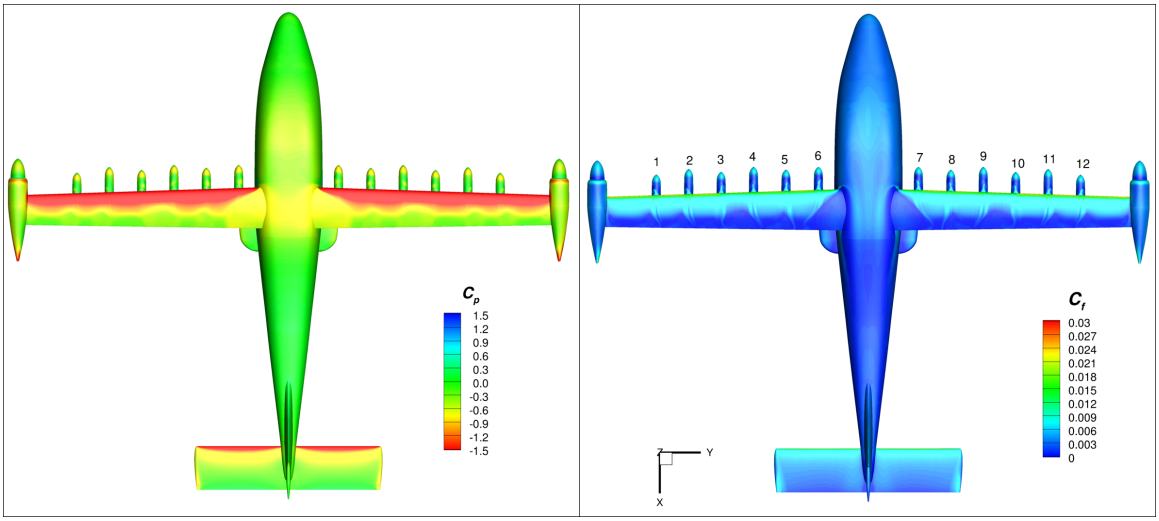

(b) KESTREL SA turbulence model

Figure 35. Code comparison of pressure coefficient (left) and skin friction coefficient (right) contours for the full geometry, configuration 12 (cruise wing, stabilator incidence -1° and 0° trim tab) at α = 15°, 150 KTAS, Re = 2.83 million, h = 8000 ft, and T = 30.5°F.

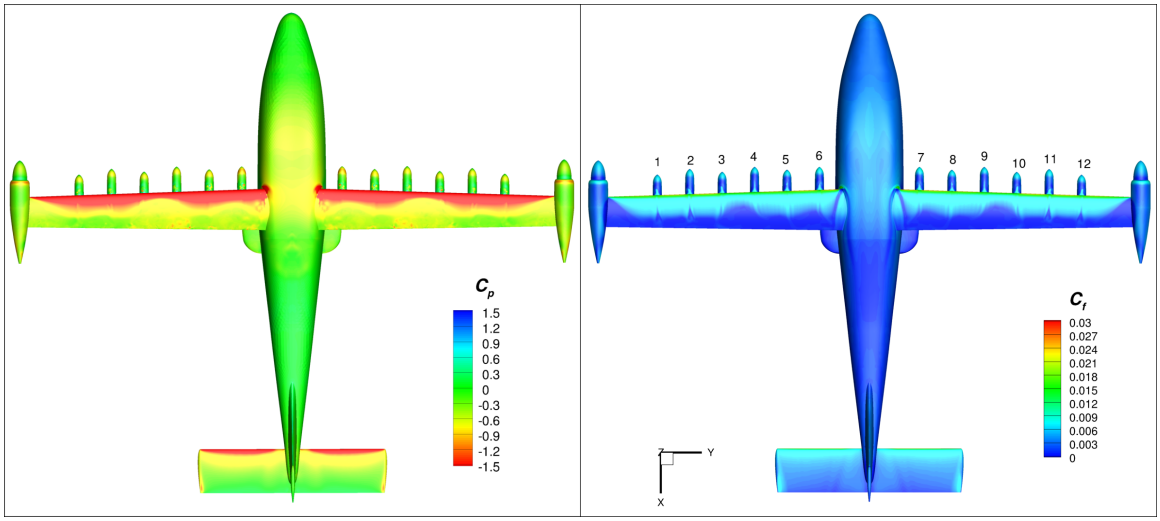

(a) USM3D SA DES

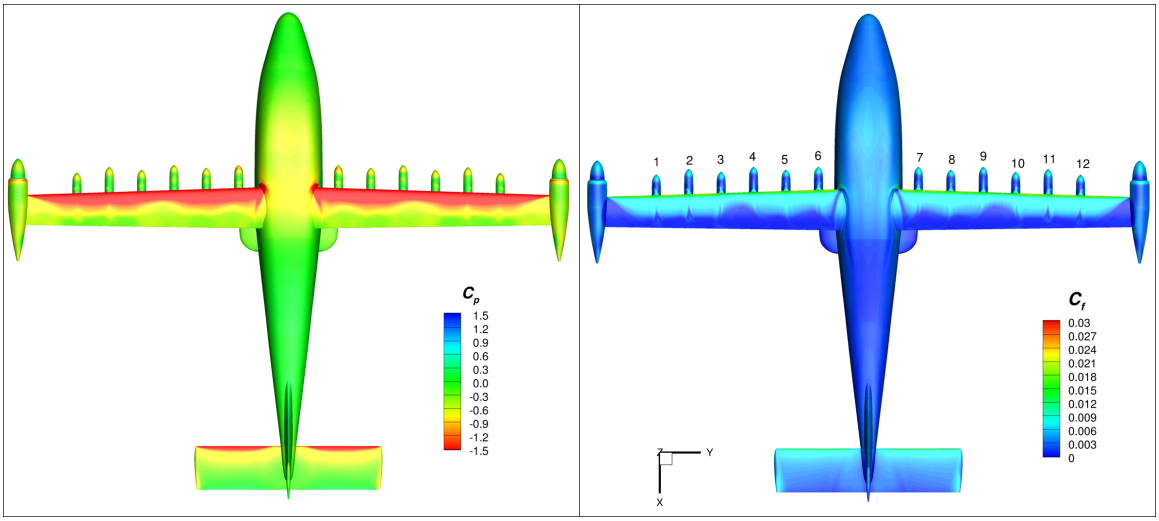

(b) KESTREL SA DDES

Figure 36. Code comparison of pressure coefficient (left) and skin friction coefficient (right) contours for the full geometry, configuration 12 (cruise wing, stabilator incidence -1° and 0° trim tab) at α = 15°, 150 KTAS, *Re* = 2.83 million, h = 8000 ft, and T = 30.5°F.